

2016

Detection Of Periodic Error And Structure Change Using Wavelet Analysis

Chao Lu

University of South Carolina

Follow this and additional works at: <https://scholarcommons.sc.edu/etd>

 Part of the [Mechanical Engineering Commons](#)

Recommended Citation

Lu, C. (2016). *Detection Of Periodic Error And Structure Change Using Wavelet Analysis*. (Doctoral dissertation). Retrieved from <https://scholarcommons.sc.edu/etd/3924>

This Open Access Dissertation is brought to you by Scholar Commons. It has been accepted for inclusion in Theses and Dissertations by an authorized administrator of Scholar Commons. For more information, please contact dillarda@mailbox.sc.edu.

DETECTION OF PERIODIC ERROR AND STRUCTURE CHANGE USING
WAVELET ANALYSIS

by

Chao Lu

Bachelor of Science
Tsinghua University, 2012

Master of Science
University of South Carolina, 2015

Submitted in Partial Fulfillment of the Requirements

For the Degree of Doctor of Philosophy in

Mechanical Engineering

College of Engineering and Computing

University of South Carolina

2016

Accepted by:

Joshua A. Tarbutton, Major Professor

Xiaomin Deng, Committee Member

Lingyu Yu, Committee Member

Stephen A. Fenner, Committee Member

Cheryl L. Addy, Vice Provost and Dean of the Graduate School

© Copyright by Chao Lu, 2016
All Rights Reserved.

DEDICATION

This work is dedicated to my parents, whose love and support make the impossible possible.

ACKNOWLEDGEMENTS

I would like to express my deepest gratitude to my advisor, Dr. Joshua Tarbutton, for his guidance, encouragement and patience. It is an honor for me to be his first PhD student. His passion on research and his teaching on me will encourage and benefit me in my future career and life.

I wish to express my thanks to the committee members, Dr. Xiaomin Deng, Dr. Lingyu Yu, and Dr. Stephen Fenner, for their valuable guidance. I also would like to thank Dr. Jonathan Ellis and Dr. Tony Schmitz for their advisement in the wavelet-based periodic error compensation project, and thank Dr. Travis Knight for his support in the spent fuel rod drying project.

Thanks are given to my colleagues in AMRL and my friends in Mechanical Engineering for their kindly help during my PhD life.

ABSTRACT

Heterodyne displacement measuring interferometry provides important metrology for applications requiring high resolution and accuracy. Heterodyne Michelson interferometers use a two-frequency laser source and separate the two optical frequencies into one fixed length and one variable length path via polarization. Ideally these two beams are linearly polarized and orthogonal so that only one frequency is directed toward each path. An interference signal is obtained by recombining the light from the two paths; this results in a measurement signal at the heterodyne (split) frequency of the laser source. This measurement signal is compared to the optical reference signal. Motion in the measurement arm causes a Doppler shift of the heterodyne frequency which is measured as a continuous phase shift that is proportional to displacement. In practice, due to component imperfections, undesirable frequency mixing occurs which yields periodic errors. Ultimately, this error can limit the accuracy to approximately the nanometer level. Periodic error is typically quantified using a Fourier transform-based analysis of constant velocity motions. However, non-constant velocity profiles lead to non-stationary signals that require alternate analysis techniques for real-time compensation. A new discrete time continuous wavelet transform (DTCWT)-based algorithm has been developed, which can be implemented in real time to quantify and compensate periodic error for constant velocity motion in heterodyne interferometer. The objective of this study is to extend the application of this algorithm to compensate non-stationary periodic error. In non-constant velocity motion, the frequency of periodic error varies with the velocity of the target.

Also, the periodic error amplitude may fluctuate due to the use of a fiber-coupled laser source. The algorithm is also applied into the situation where higher order periodic error occurs. To validate the effectiveness of the novel wavelet-based algorithm in practice, the algorithm is implemented on the hardware and operated in real-time.

The wavelet analysis is generalized and extended to a method of structural health monitoring (SHM). Currently, there are nearly 70,000 t of used nuclear fuel in spent fuel pools or dry cask storage increasing by nearly 2,000 t per year. After being used in a reactor, this fuel is stored for 3 to 5 years in spent fuel pools. Eventually the spent fuel will be placed into dry cask storage for another 20 years to more than 100 years. From the spent fuel pool, used fuel rod assemblies are loaded into casks underwater. This water must be removed to avoid corrosion or potential creation of combustion gases burning subsequent storage. During the drying process, if this operation is rapid, the water retained in the failed rods is likely to form ice. In this case, the ice crystal is difficult to remove. Moreover, if the ice forms at some critical location on the water flow path (e.g., a fretting on a fuel rod), it will prevent removal of the remaining water inside the rod. The objective of this research is to develop an integrated wavelet-based approach for structural health monitoring in dry cask storage based on concepts developed in the periodic error compensation. The key conditions (defect location, ice formation, etc.) of failed fuel rods in dry cask storage are monitored to acquire any possible structure change in real-time. The relationship between different conditions and wavelet transform results is investigated. Simulations and experiments are used to validate this approach. A wavelet-based approach can be used to effectively do SHM and periodic error compensation.

TABLE OF CONTENTS

DEDICATION	iii
ACKNOWLEDGEMENTS.....	iv
ABSTRACT	v
LIST OF TABLES	ix
LIST OF FIGURES	x
LIST OF SYMBOLS	xiv
LIST OF ABBREVIATIONS.....	xv
CHAPTER 1: WAVELET ANALYSIS.....	1
1.1 INTRODUCTION.....	1
1.2 DISCRETE WAVELET TRANSFORM	3
1.3 CONTINUOUS WAVELET TRANSFORM	5
CHAPTER 2: PERIODIC ERROR COMPENSATION IN HETERODYNE INTERFEROMETRY	15
2.1 BACKGROUND	15
2.2 PROBLEM DEFINITION	17
2.3 RESEARCH OBJECTIVE	18
2.4 HETERODYNE INTERFEROMETER.....	18
2.5 PERIODIC ERROR	23
2.6 WAVELET-BASED PERIODIC ERROR COMPENSATION ALGORITHM	31
2.7 APPLICATION ON CONSTANT VELOCITY MOTION	36
2.8 EXTENDED APPLICATION ON NON-CONSTANT VELOCITY MOTION	43

2.9 HARDWARE IMPLEMENTATION	53
CHAPTER 3: STRUCTURAL HEALTH MONITORING IN DRY CASK STORAGE.....	58
3.1 BACKGROUND.....	58
3.2 PROBLEM DEFINITION	60
3.3 RESEARCH OBJECTIVE	63
3.4 GUIDED WAVES IN PIPES.....	64
3.5 WAVELET-BASED FAILED FUEL ROD CONDITION DETECTION APPROACH	73
CHAPTER 4: CONCLUSIONS AND FUTURE WORK.....	89
4.1 CONCLUSIONS	89
4.2 FUTURE WORK.....	90
REFERENCES	92

LIST OF TABLES

Table 2.1 NI PXIe-7975R specifications	55
Table 3.1 Bessel function types used at different frequencies	70

LIST OF FIGURES

Figure 1.1 Structure of a discrete wavelet transform (DWT) computation	5
Figure 1.2 (a) Translation of the mother wavelet (the real Morlet wavelet). (b) Stretching and squeezing the real Morlet wavelet at three dilations, $s = 1, 2, 3$	7
Figure 1.3 The Haar wavelet.....	9
Figure 1.4 One Hermitian wavelet (first derivative of a Gaussian function).....	10
Figure 1.5 The Mexican hat wavelet.....	11
Figure 1.6 The complex Morlet wavelet.....	12
Figure 2.1 Schematic of the Michelson interferometer	16
Figure 2.2 Schematic of a single pass interferometer	20
Figure 2.3 Schematic of heterodyne interferometer setup. Optical components include: retroreflectors (RR), polarizing beam splitter (PBS), polarizers, half wave plate (HWP), and photodetectors	21
Figure 2.4 (a) Simulated linear displacement at 50 mm/min and periodic error with magnitudes of 4 nm and 2.5 nm for first and second order, respectively. (b) Periodic error amplitudes in the frequency domain	25
Figure 2.5 Interferometer showing optical mixing	29
Figure 2.6 First and second order periodic error in time and spatial domain	30
Figure 2.7 DTCWT coefficients calculation at $n = N$ and scale $s[1..M]$	32
Figure 2.8 Calculations to implement the periodic error compensation algorithm	36
Figure 2.9 Simulated linear displacement at 50 mm/min and periodic error with magnitudes of 4 nm and 2.5 nm for first and second order	38
Figure 2.10 The measured DTCWT ridge for the error signal	39

Figure 2.11 The measured amplitudes for the FFT and DTCWT approaches.....	41
Figure 2.12 The result of periodic error compensation (both DTCWT and FFT approaches) in the time domain	41
Figure 2.13 (a) The result of periodic error compensation in the frequency domain is presented. (b) Zoomed view of the compensation result for first order periodic error. (c) Zoomed view of the compensation result for second order periodic error	42
Figure 2.14 Accelerating motion at 50 mm/min ² and periodic error with magnitudes of 4 nm and 2.5 nm for first and second order	44
Figure 2.15 The measured DTCWT ridge for the error signal (simulated non-constant velocity motion)	45
Figure 2.16 The measured amplitudes for the DTCWT approach (simulated non-constant velocity motion)	46
Figure 2.17 The result of periodic error compensation in the time domain (simulated non-constant velocity motion).....	47
Figure 2.18 Experimental displacement for a 50 mm/min ² constant acceleration and periodic error.....	48
Figure 2.19 The measured DTCWT ridge for the error signal (experimental non-constant velocity motion)	48
Figure 2.20 The result of periodic error compensation in the time domain (experimental non-constant velocity motion)	49
Figure 2.21 Zoomed view of periodic error compensation result (experimental non-constant velocity motion).....	49
Figure 2.22 Simulated displacement for a 3000 mm/min ² constant acceleration and periodic error with varying amplitudes.....	51
Figure 2.23 The measured DTCWT ridge for the error signal (varying amplitudes).....	51
Figure 2.24 The measured amplitudes for the DTCWT approach (varying amplitudes) ..	52
Figure 2.25 The result of periodic error compensation in the time domain (varying amplitudes).....	52
Figure 2.26 Simulated displacement for a 1800 mm/min ² constant acceleration and periodic error with high orders	53

Figure 2.27 The measured amplitudes for the DTCWT approach (high orders).....	54
Figure 2.28 The result of periodic error compensation in the time domain (high orders).	54
Figure 2.29 NI FPGA module and PXI platform.....	56
Figure 2.30 The result of periodic error compensation in the time domain (hardware)....	57
Figure 3.1 Illustration of dry storage	59
Figure 3.2 Grid to rod fretting failure in the fuel rod.....	61
Figure 3.3 An example of a sealed chamber to accommodate the mock fuel rod assembly.....	62
Figure 3.4 Defect on a mock failed fuel rod	63
Figure 3.5 Cylindrical coordinates of a hollow cylinder	67
Figure 3.6 (a) Phase velocity and (b) group velocity dispersion curves of axisymmetric longitudinal waves ($L(0,m)$) in a 304 stainless steel pipe (12.7 mm outer diameter and 10.9 inner diameter), where m is the mode family order.....	74
Figure 3.7 (a) Phase velocity and (b) group velocity dispersion curves of axisymmetric torsional waves ($T(0,m)$) in a 304 stainless steel pipe (12.7 mm outer diameter and 10.9 inner diameter), where m is the mode family order.....	75
Figure 3.8 The CWT results of transmitted and received signals. t_1 and t_2 show different propagation time for f_1 and f_2 guided waves ($L(0,1)$ mode).....	77
Figure 3.9 The finite element model of the failed fuel rod with defect, and guided wave propagation simulation.....	78
Figure 3.10 The definition of angle θ between defect and receiver sensor along circumferential direction.....	79
Figure 3.11 Simulation results of the maximum modulus in CWT at (a) 50 kHz and (b) 100 kHz frequencies for different angles between received sensor and defect (1 mm) along circumferential direction	80
Figure 3.12 Simulation results of the maximum modulus in CWT at (a) 50 kHz and (b) 100 kHz frequencies for different sizes of defects at 0° , 90° and 180° angles between received sensor and defect along circumferential direction.....	81
Figure 3.13 Pitch-catch measurement for ice formation and ice level detection.....	83

Figure 3.14 Tuning curve of a round PZT (7 mm diameter, 0.2 mm thickness) bonded on a 304 stainless steel pipe (12.7 mm outer diameter and 10.9 inner diameter).....	85
Figure 3.15 Experiment setup for PZT sensing system	86
Figure 3.16 Experimental results for the measured ice levels by 50 kHz and 100 kHz guided waves.....	87
Figure 3.17 The wavelet-based approach for structural health monitoring in dry cask storage.....	88

LIST OF SYMBOLS

φ	Scaling function.
ψ	Wavelet function.
u	Shift parameter in the continuous wavelet transform.
s	Scale parameter in the continuous wavelet transform.
W	The continuous wavelet transform operation.
E	Light wave amplitude.
f	Light wave frequency.
λ	Light wave wavelength.
ϕ	Phase.
ω	Angular frequency.
A	Periodic error amplitude.
u	Displacement.
ρ	Density.
Φ	Dilatational scalar potential.
H	Equivoluminal vector potential.
k	Wavenumber.

LIST OF ABBREVIATIONS

CWT.....	Continuous Wavelet Transform
DTCWT	Discrete Time Continuous Wavelet Transform
DWT	Discrete Wavelet Transform
FEM	Finite Element Method
HWP.....	Half Wave Plate
LP	Linear Polarizer
PBS	Polarizing Beam Splitter
PZT	Piezoelectric ceramic Lead Zirconate Titanate
RMS	Root Mean Square
RR	Retroreflector
SHM.....	Structural Health Monitoring
WT	Wavelet Transform

CHAPTER 1

WAVELET ANALYSIS

Wavelet analysis began in the mid-1980s where it was first used to examine seismic signals. At the beginning of 1990s, wavelet analysis was recognized as a useful tool in science and engineering, and began rapidly developing during that decade. The wavelet transform has been found to be particularly useful for analyzing aperiodic, noisy, intermittent, and transient signals. It can examine a signal in both time and frequency domain, which is distinctly different from the traditional Fourier transform. A number of wavelet-based methods have been created to identify signals based on this advantage. Wavelet analysis has been applied to many research areas, including condition monitoring of machinery, video image compression, seismic signal denoising, characterization of turbulent intermittency, analysis of financial indices, etc.

1.1 INTRODUCTION

Wavelet analysis has been developed to be an analytical tool for signal processing, mathematical modeling, and numerical analysis. Early work was in the 1980's by Morlet, Grossmann, Meyer, Mallat, and others, and the paper by Ingrid Daubechies in 1988 first directed the attention of the larger applied mathematics communities in signal processing and statistics to wavelet analysis [1-6]. Early work was related to a specific application, and now the theory is abstracted from applications and developed on its own. One

modern wavelet research goal is to create a set of basic functions and transforms describing a function or signal. Work done by Donoho, Johnstone, Coifman, and others explained why wavelet analysis is versatile and powerful and showed wavelet system is optimal for a number of problems [7]. Multiresolution is another important feature. Wavelets are called “The Mathematical Microscope” since discrete wavelet transform can decompose a signal at independent scales and conduct this in a quite flexible way which is superior to other methods for processing, denoising, and compression [8, 9]. Because of this advantage, signal processing in wavelet domain provides many new methods for signal detection, compression, and filtering [7, 10-14].

The wavelet transform includes the discrete wavelet transform (DWT) and the continuous wavelet transform (CWT). The DWT is usually used for compression, filtering, and denoising, while the CWT is preferred to provide interpretable multi-scale information of signals. The transform is computed at various locations of the signal and for various scales of the wavelet, thus filling up the transform plane. This is done in a smooth continuous fashion for the continuous wavelet transform (CWT). A CWT of a time domain signal provides information in both the temporal and frequency domains [15]. For example, calculating the Morlet CWT enables the frequency content of a signal to be observed at different times. The CWT can be more informative than the Fourier transform because the CWT shows the relationship between frequency content and signal based on the wavelet scale and the time period. This enables the frequency and time information of the signal to be determined simultaneously by applying an appropriate wavelet. When applied to non-stationary signals, the CWT can supply frequency information at any time.

The next two sections introduce these two transforms separately.

1.2 DISCRETE WAVELET TRANSFORM

A signal $f(t)$ can be better analyzed if expressed as a linear decomposition

$$f(t) = \sum_l a_l \psi_l(t), \quad (1.1)$$

where l is an integer index for the finite or infinite sum, a_l is the real-valued expansion coefficient, and $\psi(t)$ is a set of the real-valued functions of t (expansion set). An unique expansion set is called a “basis”. If the basis is orthogonal, i.e.

$$\langle \psi_k(t), \psi_l(t) \rangle = \int \psi_k(t) \psi_l(t) dt = 0 \quad k \neq l, \quad (1.2)$$

Then the coefficient a_l can be calculated by

$$a_l = \langle f(t), \psi_k(t) \rangle = \int f(t) \psi_k(t) dt. \quad (1.3)$$

For the wavelet expansion, a two-parameter system is constructed as

$$f(t) = \sum_k \sum_j a_{j,k} \psi_{j,k}(t). \quad (1.4)$$

where $a_{j,k}$ is a set of expansion coefficients. Two-dimensional families of scaling and wavelet functions are generated from the basic scaling function and mother wavelet, $\varphi(t)$ and $\psi(t)$, by scaling and translation,

$$\begin{aligned} \varphi_{j,k}(t) &= 2^{j/2} \varphi(2^j t - k) \\ \psi_{j,k}(t) &= 2^{j/2} \psi(2^j t - k) \end{aligned} \quad (1.5)$$

where j is the scale, and k is the time or space location. Further, $\varphi(t)$ and $\psi(t)$ can be expressed as

$$\begin{aligned}\varphi(t) &= \sum_n h(n) \sqrt{2} \varphi(2t-n) \\ \psi(t) &= \sum_n h_1(n) \sqrt{2} \varphi(2t-n)\end{aligned}\quad (1.6)$$

where $h(n)$ and $h_1(n)$ are low-pass filter and high-pass filter in the decomposition filters, respectively. Therefore, as a series expansion in terms of the scaling functions and wavelets, any function $g(t)$ can be given by

$$g(t) = \sum_k c_{j_0}(k) 2^{j_0/2} \varphi(2^{j_0}t - k) + \sum_k \sum_{j=j_0}^{\infty} d_j(k) 2^{j/2} \psi(2^j t - k), \quad (1.7)$$

where j_0 is the basis scale, and $c(k)$ and $d(k)$ are some sets of coefficients. These coefficients are called the discrete wavelet transform of the signal $g(t)$, and Equation 1.7 is the inverse discrete wavelet transform (IDWT). If the wavelet system is orthogonal, the coefficients can be calculated by

$$\begin{aligned}c_j(k) &= \langle g(t), \varphi_{j,k}(t) \rangle = \int g(t) \varphi_{j,k}(t) dt \\ d_j(k) &= \langle g(t), \psi_{j,k}(t) \rangle = \int g(t) \psi_{j,k}(t) dt\end{aligned}\quad (1.8)$$

The DWT applies a pair of decomposition filters to the original time domain signal repeatedly. The low-pass filter and high-pass filter are designed to avoid any loss of information during transform process. Figure 1.1 shows a typical structure of the DWT process. For a decomposition at a single scale, the wavelet decomposition filters are applied to a signal $x(t)$ in time domain, and the output coefficients are down sampled into low-pass band (approximation band) A_1 and high-pass band (detail band) D_1 . The bands are time domain signals, and they have half of samples compared to the original signal. At the next stage, the low-pass band A_1 is decimated into quarters, A_2 and D_2 ,

and so on. The final output of DWT is the approximation subband of the final scale (A_2 in this example), and the detail subband of all the scales (D_1 , D_2 and D_3 in the same example).

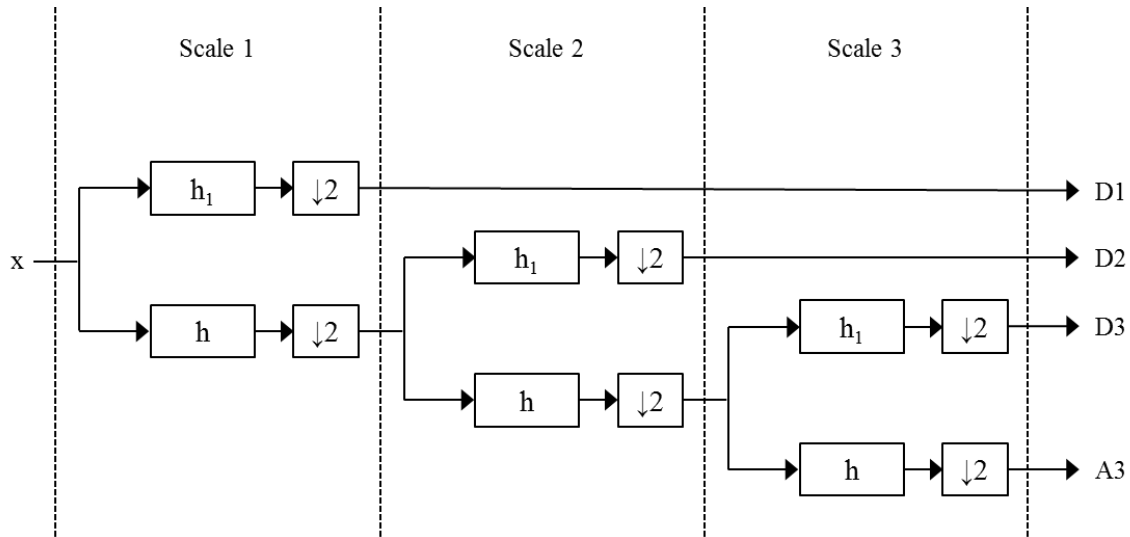


Figure 1.1 Structure of a discrete wavelet transform (DWT) computation.

However, after transforming a signal, the DWT wavelet coefficients are difficult to interpret and need an IDWT for comparison with the original signal. For CWT, in contrast, the wavelet coefficient directly provides substantial information at any particular time instance for a time domain signal. The final goal of this research is to analyze the signals in real-time. Therefore, CWT is used in a real-time algorithm design to examine the spectral information of signals.

1.3 CONTINUOUS WAVELET TRANSFORM

A continuous wavelet transform is used to construct a time-frequency representation of a signal $x(t)$ which provides sufficient time and frequency localization.

To perform a CWT, a wavelet is needed. It is a function $\psi(t)$ which satisfies certain mathematical criteria. This function is operated to transform the time domain signal into another form via translation and dilation.

1.3.1 REQUIREMENTS FOR THE WAVELET

A wavelet function of time, $\psi(t)$, must have finite energy

$$E = \int_{-\infty}^{+\infty} |\psi(t)|^2 dt < \infty. \quad (1.9)$$

A wavelet must have an average of zero,

$$\bar{\psi}(t) = \int_{-\infty}^{+\infty} \psi(t) dt = 0. \quad (1.10)$$

Additionally, a wavelet is usually normalized to a unit value [16],

$$\|\psi(t)\|^2 = \int_{-\infty}^{+\infty} |\psi(t)| dt = 1. \quad (1.11)$$

1.3.2 WAVELET MANIPULATIONS

In order to transfer a chosen “mother” wavelet to be a more flexible form, two basic manipulations can be performed. The wavelet function can be stretched and squeezed (dilation), or moved (translation).

A wavelet family can be generated from the mother wavelet by translating it via the shift parameter, $u \in \mathfrak{R}$, and dilating the wavelet via the scale parameter, $s > 0$. This series of wavelets can be denoted as

$$\psi_{u,s}(t) = \psi\left(\frac{t-u}{s}\right). \quad (1.12)$$

The movement of the wavelet along the time axis is governed by the shift parameter.

Figure 1.2(a) displays the movement of the real part of the Morlet wavelet from $u = 0$ via $u = 1$ to $u = 2$ along the time axis. The dilation and contraction of the wavelet is governed by the scale parameter, which is the distance between the center of the wavelet and the origin of time axis. Figure 1.2(b) shows the real Morlet wavelet stretched and squeezed to half and double of its original width, respectively.

1.3.3 WAVELET TRANSFORM

In the form of Equation 1.12, the wavelet transform of a continuous signal, $x(t)$, with respect to a wavelet function is defined as

$$Wx(u, s) = w(a) \int_{-\infty}^{+\infty} x(t) \psi_{u,s}^*(t) dt = w(a) \int_{-\infty}^{+\infty} x(t) \psi^* \left(\frac{t-u}{s} \right) dt, \quad (1.13)$$

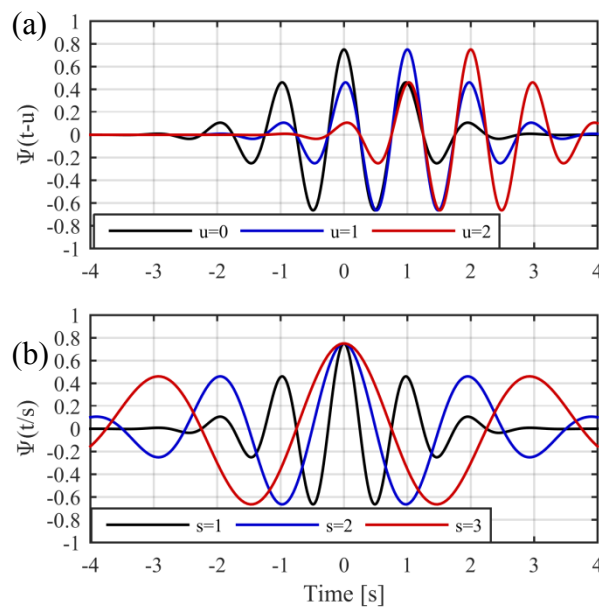


Figure 1.2 (a) Translation of the mother wavelet (the real Morlet wavelet). (b) Stretching and squeezing the real Morlet wavelet at three dilations, $s = 1, 2, 3$.

where $w(a)$ is a weighting function, and the asterisk indicates the complex conjugate of the wavelet function used in the transform, which is needed when complex wavelets are used. Typically $w(a)$ is chosen as $1/\sqrt{a}$ for energy conservation, which ensures the wavelet at each scale has the same energy. Sometimes $1/a$ is also adopted in some special applications.

In the following discussion, $w(a) = 1/\sqrt{a}$ is used as the weighting function. Thus the wavelet transform is written as

$$Wx(u, s) = \frac{1}{\sqrt{a}} \int_{-\infty}^{+\infty} x(t) \psi^* \left(\frac{t-u}{s} \right) dt. \quad (1.14)$$

This is the continuous wavelet transform. The signal $x(t)$ could be a gearbox vibration signal, audio signal, or even a crack profile in the spatial domain. The normalized wavelet function can be written as

$$\psi_{u,s}^*(t) = \frac{1}{\sqrt{a}} \psi^* \left(\frac{t-u}{s} \right). \quad (1.15)$$

Equation 1.14 shows the integration in the product of the signal and the normalized wavelet. In mathematics, this is called the convolution integral. Therefore, the CWT can be described in a compact form as

$$Wx(u, s) = \int_{-\infty}^{+\infty} x(t) \psi_{u,s}^*(t) dt. \quad (1.16)$$

1.3.4 TYPICAL WAVELETS

The Haar wavelet is a sequence of rescaled square functions [17]. It is the simplest example of an orthonormal wavelet. The Haar wavelet is also known as

Daubechies 1 tap wavelet. The mother wavelet of the Haar wavelet (shown in Figure 1.3) can be described as

$$\psi(t) = \begin{cases} 1 & 0 \leq t < \frac{1}{2} \\ -1 & \frac{1}{2} \leq t < 1 \\ 0 & \text{otherwise} \end{cases} \quad (1.17)$$

Based on the characteristics of the Haar wavelet, it can be useful in discontinuity detection.

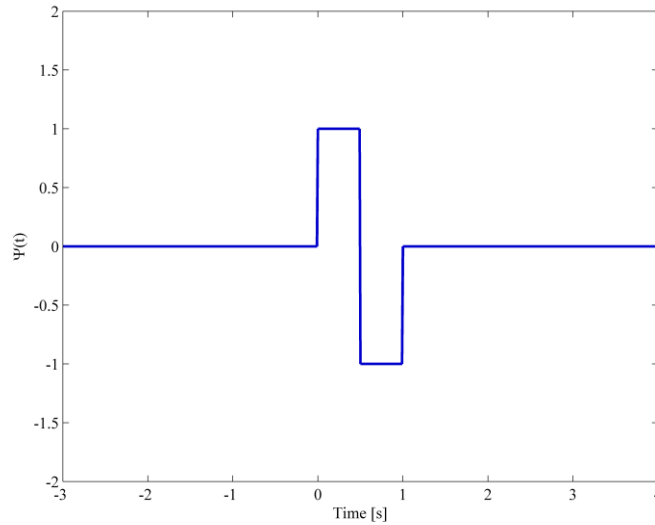


Figure 1.3 The Haar wavelet.

Hermitian wavelets are a family of continuous wavelet, which can also be used in the CWT [18]. The n^{th} Hermitian wavelet is defined as the n^{th} derivative of a Gaussian function,

$$\psi_n(t) = (2n)^{-\frac{n}{2}} c_n H_n\left(\frac{t}{\sqrt{n}}\right) e^{-\frac{1}{2n}t^2}, \quad (1.18)$$

where $H_n(x)$ denotes the n^{th} Hermite polynomial, and the normalization coefficient is given by

$$c_n = \left(n^{2-n} \sqrt{\pi} 2^{-n} (2n-1)!! \right)^{-\frac{1}{2}} \quad n \in \mathbb{N} . \quad (1.19)$$

Figure 1.4 shows an example of Hermitian wavelets, which is the negative normalized first derivative of a Gaussian function,

$$\psi_1(t) = \sqrt{2\pi}^{-\frac{1}{4}} t e^{-\frac{t^2}{2}} . \quad (1.20)$$

Figure 1.5 displays another example of a Hermitian wavelet, which is sometimes called “Mexican hat wavelet” and is the negative normalized second derivative of a Gaussian function [19],

$$\psi_2(t) = \frac{2}{3} \sqrt{3\pi}^{-\frac{1}{4}} (1-t^2) e^{-\frac{t^2}{2}} . \quad (1.21)$$

Depending on the application, all derivatives of the Gaussian function may be employed as a wavelet.

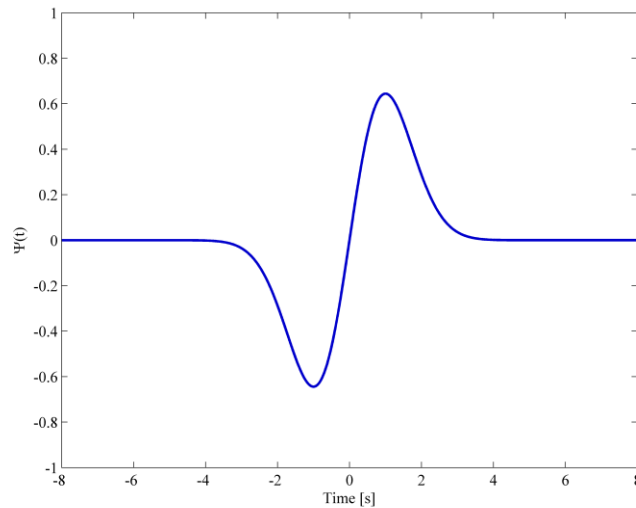


Figure 1.4 One Hermitian wavelet (first derivative of a Gaussian function).

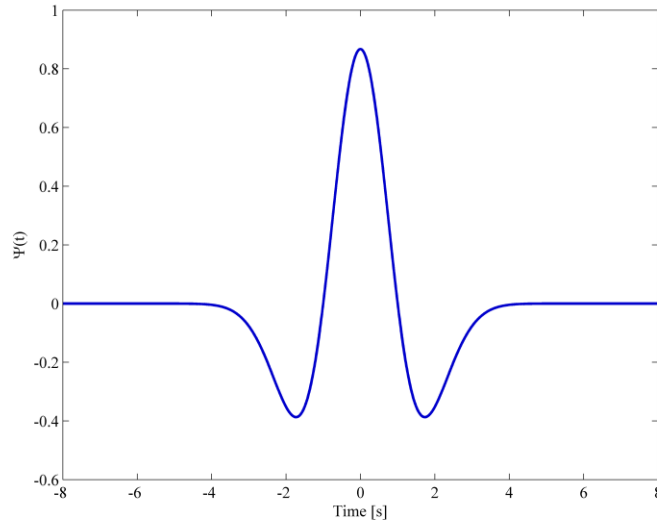


Figure 1.5 The Mexican hat wavelet.

The complex Morlet wavelet is composed of a complex exponential multiplied by a Gaussian window (shown in Figure 1.6),

$$\psi^*(t) = \pi^{-\frac{1}{4}} e^{i2\pi f_0 t} e^{-\frac{1}{2}t^2}. \quad (1.22)$$

where f_0 is the central frequency of the mother wavelet. It is closely related to human hearing and vision, and has been applied into many research fields, such as the electrocardiogram (ECG), medicine, and music transcription. More detailed introduction and analysis to the complex Morlet wavelet is given in next section.

1.3.5 COMPLEX MORLET WAVELET

In 1946, the use of Gaussian-windowed sinusoids for time-frequency decomposition was introduced from ideas in quantum physics. It provides the best trade-off between spatial and frequency resolution. In 1984, it was modified to keep the same

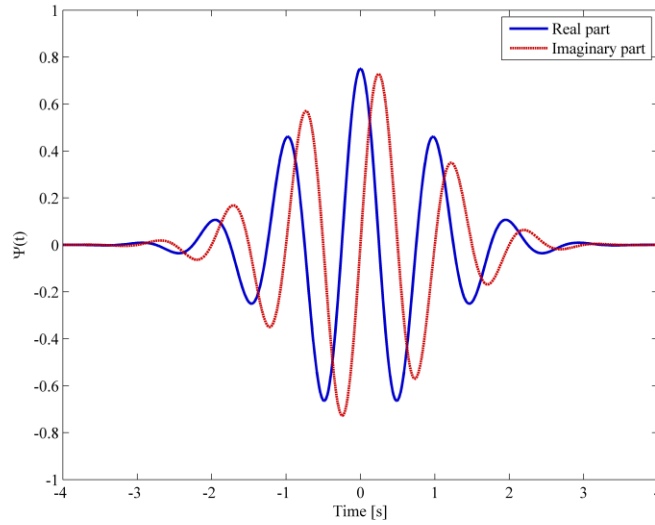


Figure 1.6 The complex Morlet wavelet.

wavelet shape over octave intervals, offering the first formalization of the continuous wavelet transform [20].

The shift parameter, u , and the scale parameter, s , can be included within the definition of the complex Morlet wavelet given by Equation 1.22. The shifted and dilated version of the mother wavelet can be given by

$$\psi^* \left(\frac{t-u}{s} \right) = \pi^{-\frac{1}{4}} e^{i2\pi f_0 \frac{t-u}{s}} e^{-\frac{1}{2} \left(\frac{t-u}{s} \right)^2}. \quad (1.23)$$

As the wavelet is squeezed and stretched to half and double of its original width (shown in Figure 1.2b), its frequency increases and decreases to double and half of its original value.

1.3.6 LINEARITY PROPERTY

One property of the continuous wavelet transform is its linearity. Given a multi-component signal $x = \sum_{i=1}^N \alpha_i x_i$, where $x_i (i=1 \dots N)$ are signal components, and $\alpha_i (i=1 \dots N)$ are scalar weightings, the linearity states that the CWT coefficients for the signal x are equivalent to the sum of the CWT coefficients for each component of x . In fact, the CWT is a convolution of a signal with a set of wavelets. Therefore, the foundation of this property is actually the linearity of integration. The property can be derived from

$$\begin{aligned} Wx(u, s) &= \int_{-\infty}^{+\infty} x(t) \psi_{u,s}^*(t) dt \\ &= \int_{-\infty}^{+\infty} \sum_{i=1}^N \alpha_i x_i(t) \psi_{u,s}^*(t) dt \\ &= \sum_{i=1}^N \alpha_i \int_{-\infty}^{+\infty} x_i(t) \psi_{u,s}^*(t) dt \\ &= \sum_{i=1}^N \alpha_i [Wx_i(u, s)] \end{aligned} \quad (1.24)$$

Based on Equation 1.24, the CWT linearity property can be expressed as

$$\left(W \sum_{i=1}^N \alpha_i x_i \right) (u, s) = \sum_{i=1}^N \alpha_i [Wx_i(u, s)]. \quad (1.25)$$

It can be used to analyze the multi-component signal. The linearity is used in the periodic error compensation algorithm to obtain periodic error amplitudes (or weightings).

1.3.7 DISCRETE TIME CONTINUOUS WAVELET TRANSFORM

The data collected from the real world is always a digital signal. Measured displacement data by a heterodyne interferometer, for instance, is collected at a very high

sampling rate (typically 50 – 100 kHz), but it is still discrete signal. For a discrete signal, the continuous wavelet transform shown in Equation 1.14 cannot be directly applied. Instead, it must be transformed to a discretized form. For a digital signal $x[1..M]$ which has M data points, the discrete time continuous wavelet transform (DTCWT) can be described as

$$Wx(n, s) = \sum_{n'=1}^M \left(x(n') \sqrt{s} \psi^* \left(\frac{(n'-n)\Delta t}{s} \right) \Delta t \right), \quad (1.26)$$

where $x(n)$ is the n^{th} discrete data point, ψ^* is the mother wavelet, M is the number of total data points in the signal, and Δt is the sampling time.

CHAPTER 2

PERIODIC ERROR COMPENSATION IN HETERODYNE INTERFEROMETRY

Since first introduced in the early 1960s, the displacement measuring interferometer has provided high accuracy, long range and high resolution for dimensional metrology. The interferometer is used in a number of non-contact displacement measurement applications including: 1) position feedback of lithographic stages for semiconductor fabrication; 2) transducer calibration; and 3) position feedback/calibration for other metrology systems. In these situations, Heterodyne (two-frequency) Michelson-type interferometers with single, double, or multiple passes of optical paths is a common configuration choice. These systems infer changes in the selected optical path length difference by monitoring the optically induced variation in the photodetector, where current is generated proportional to the optical interference signal. The current is processed and converted to voltage and the phase is determined by phase-measuring electronics. The measured phase change is nominally linearly proportional to the displacement of the measurement target, based on ideal performance of the optic elements.

2.1 BACKGROUND

The use of monochromatic light as a standard technique for displacement measurement was first introduced in 1892. Interferometry was used for the measurement of the standard meter by Albert Michelson and Rene Benoit. A schematic of the

Michelson interferometer is shown in Figure 2.1. Beam 1 is from an extended light source, and split by a beam splitter with semi-reflective coating on the surface. Two separated beams travel to and reflect back from two mirrors, M1 and M2 (M2 can move to generate an optical path difference), and then recombine at the same beam splitter. The interference pattern of the recombined beam is imaged on the screen.

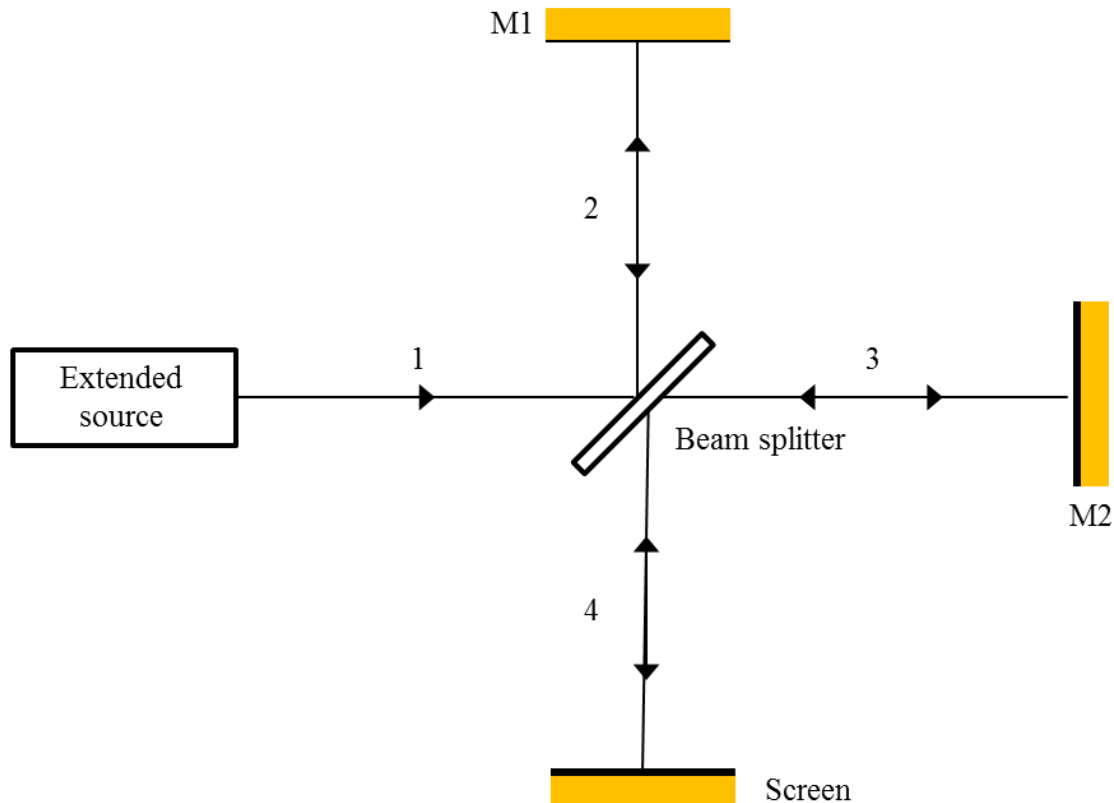


Figure 2.1 Schematic of the Michelson interferometer.

After the development of the He-Ne laser in the 1960s, interferometry has been widely used for precision length and displacement measurement in many demanding applications requiring high resolution and accuracy. In past five decades, the basic configuration of the interferometer, developed by Michelson, remains the same. The modern interferometer has been developed with the improvement in laser source, optics,

and signal processing. The extended light source is replaced by the laser, generating monochromatic light, and the screen is replaced by a photodetector, with an added digital electronics behind to interpret the measurement signal (irradiance variation or phase change) and to convert fringe to displacement.

Currently, polarization encoded heterodyne interferometers have become a standard instrument for displacement measurement. Its difference from a homodyne (single frequency) interferometer is that the laser source in a heterodyne interferometer emits two slightly different frequencies. This difference introduces a number of advantages and results in improved accuracy.

2.2 PROBLEM DEFINITION

Periodic error is an intrinsic error among various error sources in the heterodyne interferometer. It is caused by optical frequency mixing, which results from non-perfect optical component alignment. Its frequency varies with the target velocity, and its amplitude may fluctuate due to the use of fiber-coupled laser source.

To compensate this error, real-time digital error measurement may be applied, as it requires no change to the optical system, which allows convenient implementation for existing systems. Previous research has demonstrated a frequency domain approach to periodic error identification [21-23], where the periodic error is measured by calculating the Fourier transform of the time domain data collected during constant velocity target motion. But, the limitation of this method is also apparent. For non-constant velocity motion, the Doppler frequency varies with velocity. In this case, the frequency domain approach is not well-suited because the Fourier transform assumes stationary signals.

Another time domain regression algorithm can compensate the periodic error in both constant and non-constant velocity motions [24, 25]. Since it uses a mathematical model for first and second order periodic error, however, it cannot be used to compensate higher order periodic error. Moreover, fiber delivery from the laser to interferometer is used to limit optical alignment and isolate heat sources, but it also leads to periodic error amplitude fluctuation, which is difficult to compensate using existing methods.

Therefore, an alternative tool, for example, wavelet analysis used in this work, is needed to overcome this issue.

2.3 RESEARCH OBJECTIVE

A wavelet-based analysis is a novel approach in the study of periodic error measurement and compensation and enables the analysis of non-constant velocity motions. This research results in a new wavelet analysis algorithm to measure and to compensate periodic error for both constant and non-constant velocity target motions. This algorithm is able to compensate the periodic error with varying amplitude and higher order. The algorithm is implemented on the hardware.

2.4 HETERODYNE INTERFEROMETER

For displacement measurement, two types of the Michelson interferometer are commonly used. One is the homodyne interferometer, which uses a single frequency laser head and converts the intensity variation induced by interferences into displacement. On the other hand, a heterodyne interferometer uses a two-frequency laser source and

measures displacement by identifying the phase shift between the reference and measurement signals.

A Michelson-type interferometer is implemented with a certain configuration (signal, double, or multiple passes of the optical path). The single pass configuration prior to the introduction of two interferometer types will be described. In a single pass configuration (shown in Figure 2.2), a beam with both vertical and horizontal polarization components splits at a polarizing beam splitter (PBS). The horizontally polarized beam is transmitted while the vertically polarized beam is reflected. The transmitted beam (measurement beam) propagates forward to the moving retroreflector and then backward to the polarizing beam; the reflected beam (reference beam) is reflected at the fixed retroreflector. The two measurement and reference beams are recombined at the PBS and brought into interference after passing through a linear polarizer (LP). The phase change of the measurement beam, $\Delta\phi_{single}$, is proportional to double displacement of the moving retroreflector,

$$\Delta\phi_{single} \propto 2d, \quad (2.1)$$

where d is the displacement of the target.

The optical resolution of the signal pass system is half of the laser wavelength. Thus, in the single pass interferometer, the target displacement can be determined by

$$d = \frac{\lambda}{2} N_{fringe}, \quad (2.2)$$

where N_{fringe} is the number of fringes, λ is the wavelength.

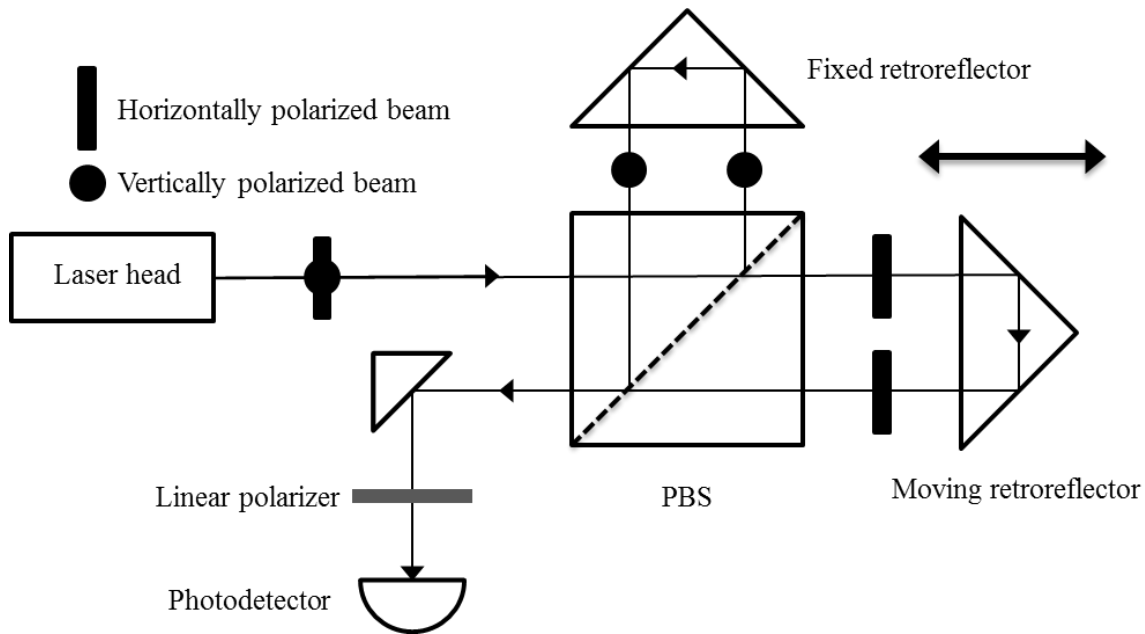


Figure 2.2 Schematic of a single pass interferometer.

The basic heterodyne interferometer consists of a laser source (two-frequency beam), a polarizing beam splitter, retroreflectors, and a photodetector. A schematic of a single pass heterodyne interferometer is shown in Figure 2.3. The laser source typically contains two slightly distinct optical frequencies with a known split frequency. They are generated by either placing a magnetic field around the laser tube to obtain two frequencies, or combining a single frequency laser with an acousto-optic modulator, which produces another beam with a modulated frequency [26]. The two optical frequencies are orthogonally polarized and do not interfere, so they can be separated. One frequency is used in the reference arm, while another one is used in the measurement arm.

An initial beam splitter splits part of the laser output, and a polarizer causes interference between the two beams. This interference is detected at the reference detector, generating an optical reference. The main beam travels to PBS, where the

frequency f_1 reference beam is reflected and then travels to the fixed retroreflector and back, while the frequency f_2 measurement beam transmits through the beam splitter and then travels to the moving retroreflector and back. The two beams are combined again within the PBS, where interference is created by passing these two collinear, orthogonal beams through this polarizer aligned at 45° . The irradiance can be then observed at the measurement photodetector.

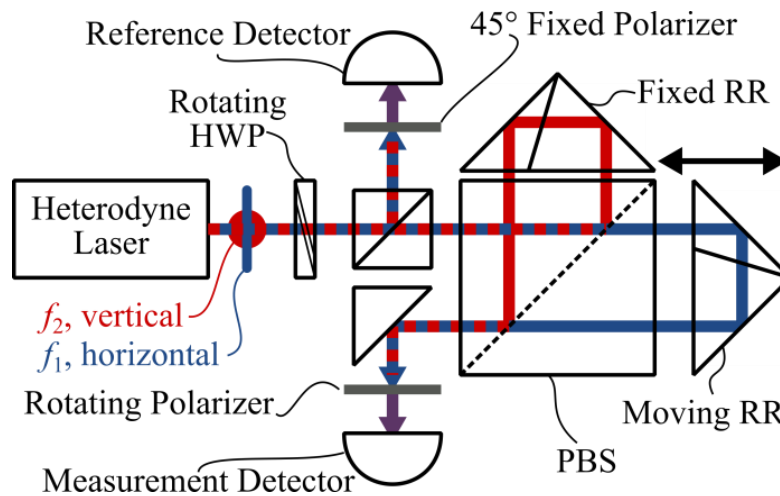


Figure 2.3 Schematic of heterodyne interferometer setup. Optical components include: retroreflectors (RR), polarizing beam splitter (PBS), polarizers, half wave plate (HWP), and photodetectors.

Heterodyne interferometer advantages:

- System has directional sensitivity.
- One optical reference can be used for multiple interferometers.
- System is insensitive to laser power fluctuations and stray light.
- System can measure fast-moving targets.
- System is adaptable to multipass configurations.

Heterodyne interferometer disadvantages:

- Two-frequency source with a split frequency is needed, increasing hardware costs.
- High speed signal processing is required.
- Polarization manipulation leads a more complex alignment procedure and costly components.

The two light waves are both linearly polarized, and have different amplitudes and frequencies. They are described by

$$\begin{aligned} E_1 &= E_{01}e^{-i(\omega_1 t + \phi_1)} \\ E_2 &= E_{02}e^{-i(\omega_2 t + \phi_2)} \end{aligned} \quad (2.3)$$

where $\omega_i = 2\pi f_i$ ($i = 1, 2$) are the different angular frequencies of the light waves, E is the light wave amplitude. According to the Principle of Superposition, when they interfere, the resultant wave, E , is given by the sum of the two light waves, E_1 and E_2 ,

$$E = E_1 + E_2 = E_{01}e^{-i(\omega_1 t + \phi_1)} + E_{02}e^{-i(\omega_2 t + \phi_2)}. \quad (2.4)$$

The resultant irradiance, I , is proportional to the square of the amplitude,

$$\begin{aligned} I \propto |E|^2 &= \left| E_{01}e^{-i(\omega_1 t + \phi_1)} + E_{02}e^{-i(\omega_2 t + \phi_2)} \right|^2 \\ &= \left(E_{01}e^{-i(\omega_1 t + \phi_1)} + E_{02}e^{-i(\omega_2 t + \phi_2)} \right) \left(E_{01}^*e^{-i(\omega_1 t + \phi_1)} + E_{02}^*e^{-i(\omega_2 t + \phi_2)} \right), \\ &= |E_{01}|^2 + |E_{02}|^2 + 2\operatorname{Re}\left(E_{01}E_{02}^*e^{-i(\Delta\omega t + \Delta\phi)} \right) \\ &= I_1 + I_2 + 2\sqrt{I_1 I_2} \cos(\Delta\omega t + \Delta\phi) \end{aligned} \quad (2.5)$$

where $\Delta\omega = \omega_1 - \omega_2$. There is a frequency difference $\Delta\omega$, referred as to split or beat frequency, which results from two slightly different optical frequencies. In the heterodyne interferometer, the irradiance is measured by the fluctuation at the split

frequency. The displacement of the moving target causes phase change, $\Delta\phi$.

Measurement of this phase change is proportional to the displacement. The output of the heterodyne interferometer occurs at some frequency around the split frequency.

Therefore, the sign of the frequency shift can describe the direction of the motion.

2.5 PERIODIC ERROR

There are many well-known error sources that can degrade the accuracy of the system [27-31]. These include cosine error, Abbe error, refractive index uncertainty, thermal drift and deadpath. These errors can be compensated by setup changes or additional metrology approaches. Other errors, such as electronics error and source vacuum wavelength uncertainty, are usually small. Frequency mixing in heterodyne interferometer resulting from non-ideal performance of the optical system causes periodic errors which are superimposed on the measured displacement signal. For heterodyne interferometers, both first and second order periodic errors occur, which correspond to one and two periods per displacement fringe. Periodic error is an intrinsic error in the heterodyne interferometer that can limit the accuracy to the nanometer level (or higher) depending on the optical setup. This is true when the interferometer is operated in vacuum to minimize the error associated with refractive index uncertainty due to uncompensated fluctuations in temperature, pressure, and humidity. While any of these error sources may dominate in a given situation, the focus of this study is periodic error.

2.5.1 INTRODUCTION

Periodic error is a noncumulative error in the measured displacement from spurious interference signal arising from source mixing and beam leakage. Imperfect separation of two frequencies into the measurement and reference beam produce periodic error, or errors of some cycles per wavelength of optical path change. From another perspective, the measured moving target displacement within superimposed periodic error can be treated as cyclically oscillating about the nominal displacement, typically with amplitude of several nanometers [32].

Ideally, the phase-to-displacement relationship is assumed to be linear, but due to the spurious interference signal, in practice, there exists a cyclic deviation and this assumption becomes incorrect since the relationship is nonlinear.

Periodic error occurs at a predictable interval. First order periodic error has one harmonic per full cycle of phase change and second periodic error has two harmonics per full cycle of phase change, etc.

Periodic error characteristics can be described as:

- Periodic error does not scale with measured displacement. Source mixing and frequency leakage cause periodic error superimposed in the true displacement to be predictable.
- Periodic error is a function of interferometer geometry and the source wavelength, detectable as first, second, and higher spatial harmonics as the target moves.
- Each order of periodic error is caused by different mixing errors and alignment.

Sources of frequency mixing and leakage include non-orthogonality between the linear beam polarization, elliptical polarization of one beam, imperfect optical components, parasitic reflections from the surface, and mechanical misalignment in the interferometer [33]. For a motion of a moving retroreflector in a single pass interferometer, for example, Figure 2.4 displays a simulated displacement of this motion from 25 μm to 30 μm with a velocity of 50 mm/min in 0.006 s, and superimposed periodic error with a first order magnitude of 4 nm and second order magnitude of 2.5 nm. The nominal constant velocity motion is extracted to reveal only the remaining periodic error component.

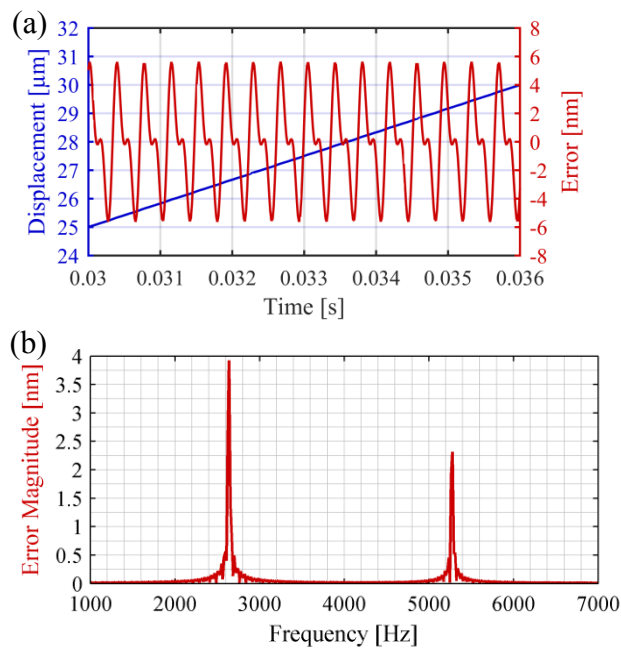


Figure 2.4 (a) Simulated linear displacement at 50 mm/min and periodic error with magnitudes of 4 nm and 2.5 nm for first and second order, respectively. (b) Periodic error amplitudes in the frequency domain.

2.5.2 LITERATURE REVIEW

Periodic error is a fundamental accuracy limitation for the heterodyne Michelson-type interferometer. It can limit the interferometer accuracy to the nanometer or subnanometer level. The measurement and reference beams are linearly polarized and mutually orthogonal, separated and recombined perfectly at polarizing beam splitter. Errors and defects in the optical system components cause source mixing and frequency leakage between the two beams. This frequency mixing causes periodic error superimposed on the measured displacement signal, which is extensively explored in the literature.

Fedotova [34], Quenelle [35], and Sutton [36] first investigated periodic error in heterodyne Michelson-type interferometers. Subsequent studies of periodic error in displacement measuring interferometry and its reduction have been reported in many publications [21, 22, 24-31, 33, 37-106]. They are divided into the following categories: 1) error sources [26-29, 37-39]; 2) refractive index in air [40-46]; 3) periodic error description and modeling [47-65]; 4) periodic error measurement under various conditions [22, 66-73]; 5) periodic error correction and compensation [21, 24, 25, 33, 56, 74-101]; 6) uncertainty evaluation of interferometric displacement measurement [30, 31]; 7) measurement applications [102-106].

Optical mixing is a major source causing periodic error in heterodyne Michelson-type interferometers that rely on polarization coding. Optical mixing refers to part of one arm frequency leakage into the other of the interferometer. This includes imperfect optical components, mechanical misalignment between interferometer elements, non-orthogonality of linear beam polarizations, ellipticity in the nominally linear polarization

of the individual beam, deviation of the optics from ideal behaviors, and parasitic reflections from individual surface.

Further, optical mixing can be subdivided into two kinds based upon the mechanism of mixing, polarization mixing and frequency mixing [27]. For polarization mixing, it is due to the imperfect separation of the beams on their polarization (due to leakage in the beam splitter). On the other hand, frequency mixing is due to contamination by correct polarization but incorrect frequency for light. It can be caused by imperfect angular alignment of the polarization states of the beam relative to the beam splitter direction, or ellipticity in polarization states for the individual beam. Each passage through the polarizing beam splitter attenuates the leakage term for polarization mixing, while in frequency mixing, repeated passage through the beam splitter does not affect the mixing. In both kinds of mixing, the consequence is always contamination from one beam in the interferometer into another.

In spite of the source of the optical mixing, its effect can be described in Figure 2.5. The interaction of the two beams with the PBS in a practical interferometer result in an imperfect separation of the two frequencies. Beam 1 with frequency f_1 and amplitude E_{01} is contaminated by a small component with frequency f_2 and amplitude ε_{21} , while beam 2 with f_2 and E_{02} is contaminated by a component with f_1 and ε_{12} . The resultant output beam has four components instead of two in the ideal interferometer. The resultant irradiance can be expressed by

$$\begin{aligned}
I \propto |E|^2 &= \left| E_{01} e^{-i(\omega_1 t + \phi_1)} + E_{02} e^{-i(\omega_2 t + \phi_2)} + \varepsilon_{21} e^{-i(\omega_2 t + \phi_1)} + \varepsilon_{12} e^{-i(\omega_1 t + \phi_2)} \right|^2 \\
&= \underbrace{\left(|E_{01}|^2 + |E_{02}|^2 + |\varepsilon_{21}|^2 + |\varepsilon_{12}|^2 \right)}_{DC \text{ Terms}} + 2 \operatorname{Re} \left\{ \underbrace{E_{01} E_{02}^* e^{-i(\Delta\omega t + \Delta\phi)}}_{\text{Nominal Signal}} \right. \\
&\quad + \underbrace{\left(E_{01} \varepsilon_{21}^* + E_{02}^* \varepsilon_{12} \right) e^{-i(\Delta\omega t)}}_{\text{First Harmonics}} + \underbrace{\varepsilon_{21}^* \varepsilon_{12} e^{-i(\Delta\omega t - \Delta\phi)}}_{\text{Second Harmonics}} \left. \right\} \quad (2.6) \\
&\quad + \underbrace{\left(E_{01} \varepsilon_{12}^* + E_{02}^* \varepsilon_{21} \right) e^{i(\Delta\phi)}}_{\text{Quasi-DC Terms}}
\end{aligned}$$

Four components combine and produce eight terms. The DC terms are the irradiance of four beams, which are self-interference. The quasi-DC terms are low-frequency irradiance variations, which originate from interference between the main component in one beam and the contamination component in the other beam with the same frequency. It is identical to the case in homodyne interferometer, and shows a small variation close to DC. In most cases they can be considered as DC terms unless $\Delta\phi$ is close to $\Delta\omega$. The remaining three terms, $E_{01} E_{02}^* e^{-i(\Delta\omega t + \Delta\phi)}$, $(E_{01} \varepsilon_{21}^* + E_{02}^* \varepsilon_{12}) e^{-i(\Delta\omega t)}$, and $\varepsilon_{21}^* \varepsilon_{12} e^{-i(\Delta\omega t - \Delta\phi)}$, are around the split frequency. The nominal signal results from the interference between two beams, and it is the desired signal. The first harmonic term arises from the interference of the desired beam and the mixing term in a given arm. The interference result is at the split frequency since they are at different frequencies f_1 and f_2 . This term can be distinguished from the nominal signal by its independence of phase. The second harmonic term arises from the interference between two mixing terms, $\varepsilon_{21} e^{-i\omega_2 t}$ and $\varepsilon_{12} e^{-i\omega_1 t}$. This result shows a negative phase dependence. Its amplitude is much smaller than that of the nominal signal. The first and second order periodic errors, which are derived from the first and second harmonic terms, can be approximately given by

$\sin(\Delta\phi)$ as a simplified model of a pure sine wave [22]. When the heterodyne interferometer system is under high-speed displacement and amplifier nonlinearity is considered, high order periodic errors will emerge as Doppler shifted terms; these errors can also be modeled as pure sine waves [48]. For convenience, each order of periodic error is expressed in terms of $A\sin\theta(t)$ in the following discussions, where t is the time, and θ is the phase.

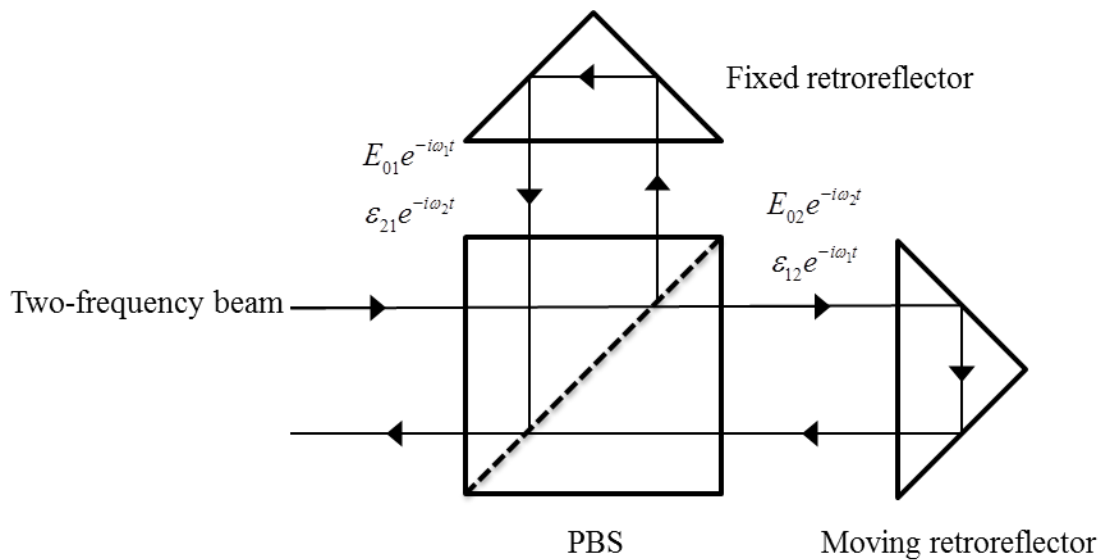


Figure 2.5 Interferometer showing optical mixing.

As discussed above, the nominal, first harmonic, and second harmonic terms are $E_{01}E_{02}^*e^{-i(\Delta\omega t + \Delta\phi)}$, $(E_{01}\epsilon_{21}^* + E_{02}^*\epsilon_{12})e^{-i(\Delta\omega t)}$, and $\epsilon_{21}^*\epsilon_{12}e^{-i(\Delta\omega t - \Delta\phi)}$. If the measured moving retroreflector is at a constant velocity, v , then $\Delta\phi$ can be described as $\frac{2\pi Nv}{\lambda}t$, where

N is the number of passes in the interferometer. In this case, $\frac{2\pi Nv}{\lambda}$ is a constant.

Therefore, these three terms are at constant frequencies of $\Delta\omega + \frac{2\pi Nv}{\lambda}$, $\Delta\omega$, and $\Delta\omega - \frac{2\pi Nv}{\lambda}$. The traditional frequency domain approach [21-23] can be applied here since they are all stationary signals. The periodic error amplitudes are determined by computing the Fourier transform of the time domain displacement data.

Each order of the periodic error can be described as a simplified mathematical model, a pure sine wave $A \sin \theta(t)$, where t is the time, A is the amplitude, and θ is the phase. For example, for a periodic error, which consists of only first and second order periodic errors, can be expressed as $A_1 \sin \theta_1(t) + A_2 \sin \theta_2(t)$. Figure 2.6 shows first and second order periodic errors in both the time and spatial (polar coordinate) domains. The frequency, f_1 , of the first order periodic error is half of the second order error frequency, f_2 . Thus, the phase, θ_1 , of first order periodic error is half of the second order phase, θ_2 .

Higher order periodic error holds the similar relationship to the first order periodic error. In general, for the k^{th} order periodic error, $A_k \sin \theta_k(t)$, the frequency, $f_k = kf_1$, and the phase $\theta_k = k\theta_1$.

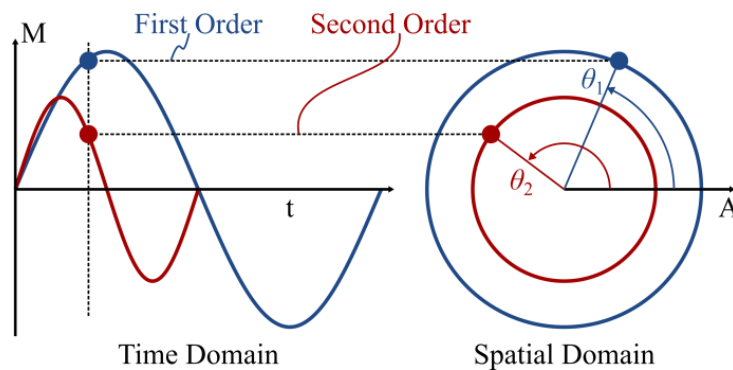


Figure 2.6 First and second order periodic error in time and spatial domain.

2.6 WAVELET-BASED PERIODIC ERROR COMPENSATION ALGORITHM

This section describes a detailed real-time periodic error compensation algorithm design based on DTCWT, where the complex Morlet wavelet is used as the mother wavelet. It includes periodic error identification and reconstruction.

2.6.1 DETREND OF THE SIGNAL

The algorithm starts with storing the latest N data points in a memory array, $X[1..N]$, which is used as the signal to conduct the DTCWT. First, detrending $X[1..N]$ is required to eliminate the main displacement component (subtracting the line connecting the beginning and ending points of the signal). This step is required because the magnitude of the periodic error is typically on the nanometer level while the overall displacement is usually on the micrometer level or larger. A new array $X'[1..N]$ is obtained after detrending the measured data $X[1..N]$.

2.6.2 APPLICATION OF THE WAVELET TRANSFORM

The DTCWT (Equation 1.26) is applied to the signal $X'[1..N]$ using the following five steps:

- 1) substitute the data points in $X'[1..N]$ for x in Equation 1.26;
- 2) select the mother wavelet to be the complex Morlet wavelet to produce child wavelets at various scales;
- 3) set the shift parameter n to N (for the last point of the array);

- 4) build a scale array $s[1 \dots M]$ to produce the child wavelets where M is the total integer number of scales used in the DTCWT calculation;
- 5) using Equation 1.26 calculate the wavelet coefficient of the N^{th} data point in the array.

Because the complex Morlet wavelet has complex values the resulting coefficients from the DTCWT calculation in Equation 1.26 will also be complex. Therefore, after applying the complex Morlet wavelet to the signal, the resulting wavelet transform is a complex array along the scale direction (see Figure 2.7).

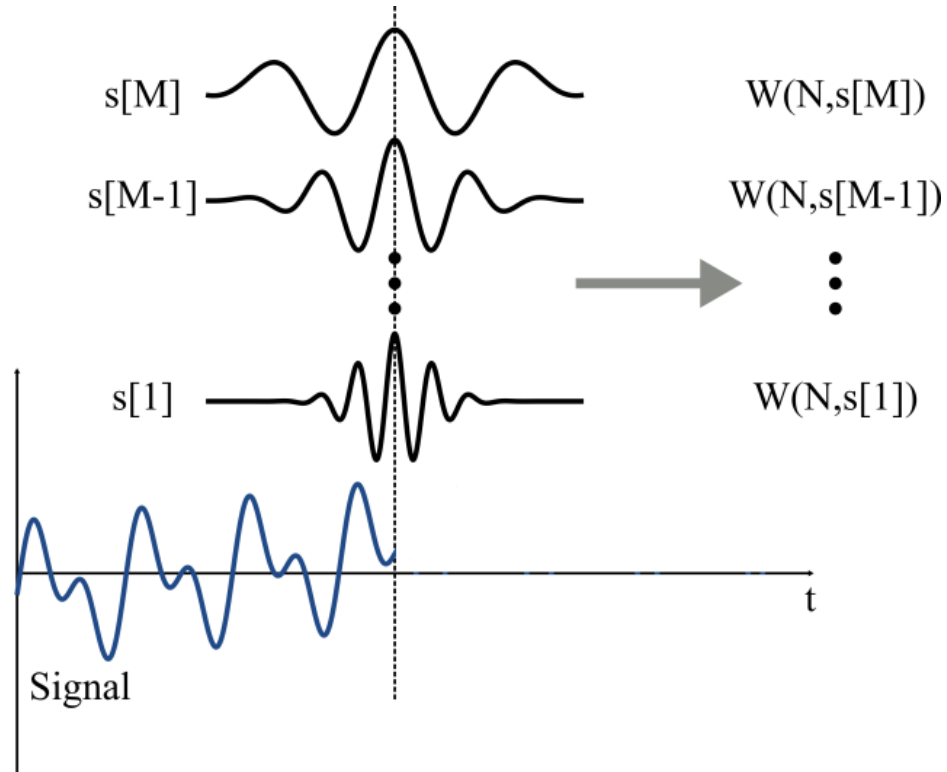


Figure 2.7 DTCWT coefficients calculation at $n = N$ and scale $s[1 \dots M]$.

2.6.3 IDENTIFICATION OF THE RIDGE AND PHASE

The modulus and the phase for each complex coefficient can be calculated as:

$$abs(n, s) = |Wx(n, s)| \text{ and} \quad (2.7)$$

$$\phi(n, s) = \arctan\left(\frac{\text{Im}(Wx(n, s))}{\text{Re}(Wx(n, s))}\right), \quad (2.8)$$

where Im and Re represent the imaginary and real parts of the DTCWT coefficient, respectively. For the modulus $abs(N, s)$ at $X'[N]$ along the scale array, the maximum value of the DTCWT coefficient or “ridge” can be extracted. The ridge is defined as the location where the modulus reaches its local maximum at scale s_{ridge} [107]. When the modulus is maximal at the ridge, the frequency of the wavelet scaled by s_{ridge} shows the greatest match with the convolved periodic error signal [108].

This s_{ridge} equals s_1 , which corresponds to the frequency of first order periodic error. Therefore, the phase $\phi(N, s_{ridge})$ is the first order periodic error phase at $X'[N]$. A phase array $\phi[1 \dots N]$ is used to store this phase. A new point is added by completing two steps: 1) remove $\phi[1]$ and shift $\phi[2 \dots N]$ forward to $\phi[1 \dots N-1]$ and 2) set $\phi[N] = \phi(N, s_{ridge})$. Subsequently, the array $\phi[1 \dots N]$ has the first order periodic error phase information for the latest N data points. Based on the periodic error model defined in Section 2.5, with the phase array $\phi[1 \dots N]$ and an assumed unit amplitude, the k^{th} order periodic error is $A_k \sin(\theta_k) = \sin(k\phi)$. It is located at the scale $s_k = s_1 / k$ since its frequency is $f_k = kf_1$ and the scale is inversely related to the frequency. The k^{th} order periodic error for the latest N points is

$$r_k[1 \dots N] = \{\sin(k\phi(1)), \sin(k\phi(2)), \dots, \sin(k\phi(N))\}, \quad (2.9)$$

which is called the “reference periodic error”.

2.6.4 IDENTIFICATION OF THE AMPLITUDE

The next step is to determine the amplitude of different periodic error orders. The entire periodic error $e[1..N]$ is a linear combination of m order periodic errors, which can be expressed as

$$e[1..N] = \sum_{j=1}^m A_j r_j[1..N], \quad (2.10)$$

where A_j ($j = 1..m$) is the periodic error amplitude on the j^{th} order, which is to be quantified.

Assuming that the detrended array, $X'[1..N]$, is exactly the periodic error¹, the assumed sinusoidal combination of periodic errors $e[1..N]$ can be said to be equivalent to $X'[1..N]$ according to Equation 2.10 to obtain

$$X'[1..N] = \sum_{j=1}^m A_j r_j[1..N]. \quad (2.11)$$

The discrete form of the CWT in Equation 1.26 can then be used on both sides of Equation 2.11. Equation 2.11 is effectively substituting the actual periodic error for x on one side of the equation and substituting the periodic error model on the other side of the equation. Once the values are substituted the complex Morlet wavelet can be used to calculate the coefficients by setting the location to be $n = N$, and using scales $s[1..M]$.

¹ If there is a difference between the detrended signal and the actual periodic error due to imperfect detrending, this causes an error in the algorithm results.

The linearity property of the CWT introduced in Equation 1.25 can then be used to construct the following result:

$$WX'[1\dots N](N, s[1\dots M]) = \sum_{j=1}^m A_j [Wr_j[1\dots N](N, s[1\dots M])], \quad (2.12)$$

where $WX'[1\dots N](N, s[1\dots M])$ has already been calculated. For m order reference periodic errors, another m DTCWT calculations about $Wr_j[1\dots N](N, s)$ ($j=1\dots m$) are required. Amplitudes A_j ($j=1\dots m$) include m unknowns, which require at least m equations to be solved. Recall that the frequency of j^{th} order periodic error is related to the scale $s_j = s_1 / j$, so the DTCWT results $WX'[1\dots N](N, s_i)$ and $Wr_j[1\dots N](N, s_i)$ at scale s_i are extracted for use ($i, j=1\dots m$). Let $c_i = WX'[1\dots N](N, s_i)$, $d_{ij} = Wr_j[1\dots N](N, s_i)$, $i, j=1\dots m$. The following set of equations can then be obtained from Equation 2.12:

$$\begin{cases} c_1 = A_1 d_{11} + A_2 d_{12} + \dots + A_m d_{1m} \\ c_2 = A_1 d_{21} + A_2 d_{22} + \dots + A_m d_{2m} \\ \vdots \\ c_m = A_1 d_{m1} + A_2 d_{m2} + \dots + A_m d_{mm} \end{cases} \Rightarrow \begin{bmatrix} A_1 \\ A_2 \\ \vdots \\ A_m \end{bmatrix} = \begin{bmatrix} d_{11} & d_{12} & \dots & d_{1m} \\ d_{21} & d_{22} & \dots & d_{2m} \\ \vdots & \vdots & \ddots & \vdots \\ d_{m1} & d_{m2} & \dots & d_{mm} \end{bmatrix}^{-1} \begin{bmatrix} c_1 \\ c_2 \\ \vdots \\ c_m \end{bmatrix}. \quad (2.13)$$

The amplitudes A_j ($j=1\dots m$) can therefore be determined.

2.6.5 RECONSTRUCTION OF PERIODIC ERROR

The magnitude M of the periodic error at the latest sampling time is calculated using

$$M = \sum_{i=1}^m A_i \sin(i\varphi(N)), \quad (2.14)$$

where $A_i \sin(i\varphi(N))$ is i^{th} order reconstructed periodic error at $n = N$. Finally, the magnitude M is subtracted from the original displacement data to determine the compensated displacement data point.

Figure 2.8 displays the sequence of calculations required for compensating one displacement data point in the DTCWT algorithm.

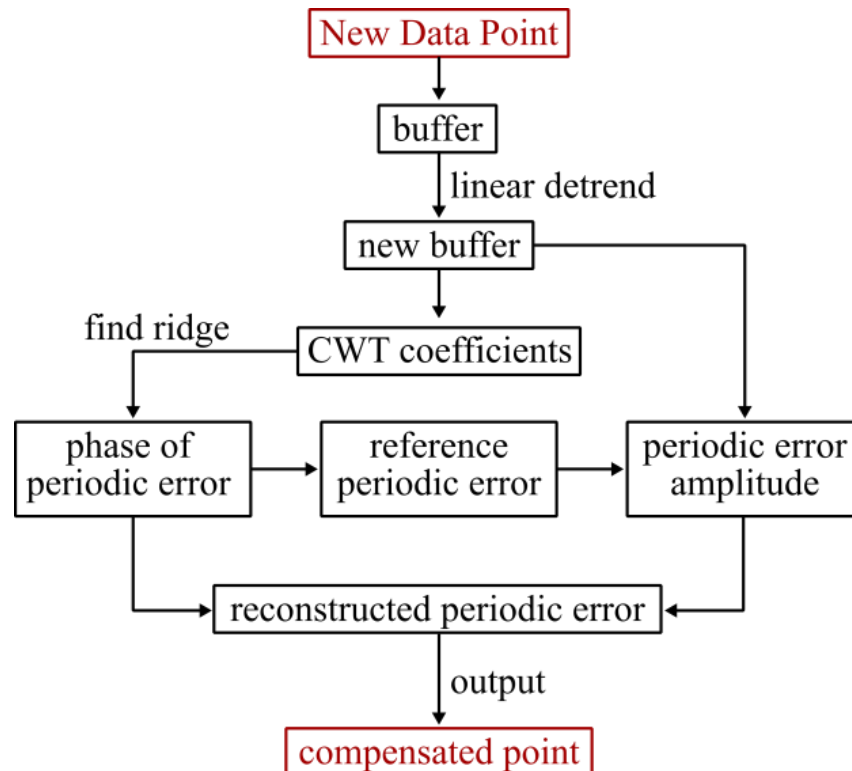


Figure 2.8 Calculations to implement the periodic error compensation algorithm.

2.7 APPLICATION ON CONSTANT VELOCITY MOTION

In this section, simulated displacement data with superimposed periodic error are used to assess the validity of the wavelet-based compensation algorithm. The simulated data is first introduced. Then identifications of periodic error ridge, phase and amplitude

are provided in sequence. Finally, overall periodic error compensation performance of the wavelet-based algorithm is shown. In order to demonstrate the capability of the wavelet-based approach to compensate periodic error, it is compared to the traditional Fourier-based approach.

2.7.1 SIMULATED DISPLACEMENT DATA

The simulated displacement is designed to coincide with the collected data in a real heterodyne interferometer. But more ideally, only the first and second order periodic errors are considered in the simulated data. The interferometer parameters used in the simulation are:

- 1) He-Ne laser wavelength of $\lambda = 633 \text{ nm}$;
- 2) a fold factor of $FF = 2$, which describes the number of light passes through the interferometer (the first order error completes a full cycle in $633/2 = 316.5 \text{ nm}$, while the second order error requires $633/4 = 158.3 \text{ nm}$);
- 3) a sampling frequency was 62.5 kHz .

A typical simulated signal used in the simulations is a linear displacement signal where first and second order periodic errors (amplitudes 4 nm and 2.5 nm , respectively) are superimposed during a constant velocity (50 mm/min) displacement as shown in Figure 2.9.

The following sections discuss the results of ridge detection, amplitude detection, and a comparison between the DTCWT and frequency domain approaches.

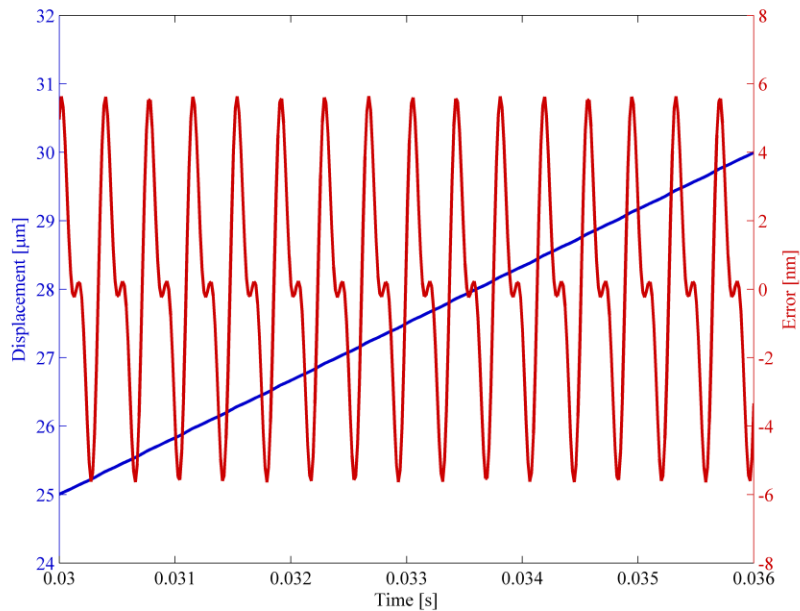


Figure 2.9 Simulated linear displacement at 50 mm/min and periodic error with magnitudes of 4 nm and 2.5 nm for first and second order.

2.7.2 RIDGE DETECTION

Identifying periodic error frequency components first requires ridge detection using Equation 2.7. The performance of the ridge detection portion of the algorithm is evaluated using the simulated displacement signal shown in Figure 2.9. The measured DTCWT ridge for this signal is displayed in Fig. 2.10 along with the result of the same algorithm implemented offline. The ridge detected from the real-time algorithm is at the integer scale 190 ± 1 . The algorithm is simulated in real-time. It means that each time a new data point is received and operated by the algorithm; only after a compensated point is outputted, next new data point will be accepted.

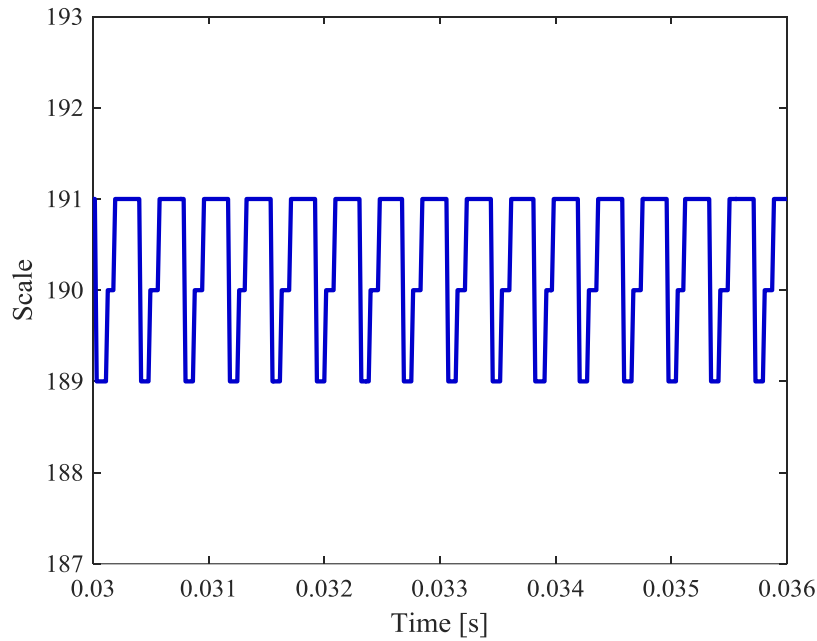


Figure 2.10 The measured DTCWT ridge for the error signal.

2.7.3 AMPLITUDE DETECTION

For the simulations in this section, a simulated constant velocity motion (50 mm/min) with first order periodic error amplitude of 4 nm and second order periodic error amplitude of 2.5 nm is used just as in Section 2.7.2. To identify the periodic error amplitudes under this constant velocity condition, two methods are compared at every sampling instant. The first method is a fast Fourier transform (FFT) method similar to [21-23]. The FFT of the error is computed after detrending the nominal displacement stored in the displacement array $X[1 \dots N]$ and applying a Hanning window. The second method is the DTCWT-based algorithm. This algorithm is applied to calculate first and second order periodic error amplitudes (Equation 2.13, where $m = 2$ because only first and second order periodic errors exist) after obtaining the modulus and phase information (Equations 2.7 and 2.8) and determining the reference periodic errors (Equation 2.9). The

measured amplitudes are displayed in Figure 2.11. The frequency domain approach result is smoother since windowing reduces the spectral leakage. The FFT assumes that the data is infinite and stationary. However, the signal used in the algorithm is finite (200 points, which is the same amount used in the DTCWT algorithm) and shifts forward by one data point each sampling interval. It actually measures the average amplitude over the signal. For first order periodic error, the true value of its amplitude is 4 nm. The average value from the FFT approach is 3.92 nm; the amplitude measured by the DTCWT approach is 4.25 nm. For second order periodic error, the true value is 2.5 nm. The amplitudes measured by the FFT and DTCWT approaches are 2.34 nm and 2.31 nm, respectively. The two approaches show good agreement for amplitude measurement.

2.7.4 PERIODIC ERROR COMPENSATION

In these tests, the performance of the entire DTCWT algorithm (from receiving a new data point to providing a compensated data point) is examined. Again, the simulated 50 mm/min constant velocity motion with superimposed periodic errors is used. The time domain periodic error compensation result is displayed in Figure 2.12. The root-mean-square error is reduced from 3.32 nm to 0.49 nm for both two methods. Figure 2.13 displays the compensation result in the frequency domain. After compensation, the amplitudes of the first and second order periodic errors are reduced from 4 nm to 0.24 nm (0.27 nm for the FFT method) and from 2.5 nm to 0.30 nm (0.27 nm for the FFT method), respectively. These similar results indicate that the DTCWT algorithm has the capability to accurately compensate the periodic error.

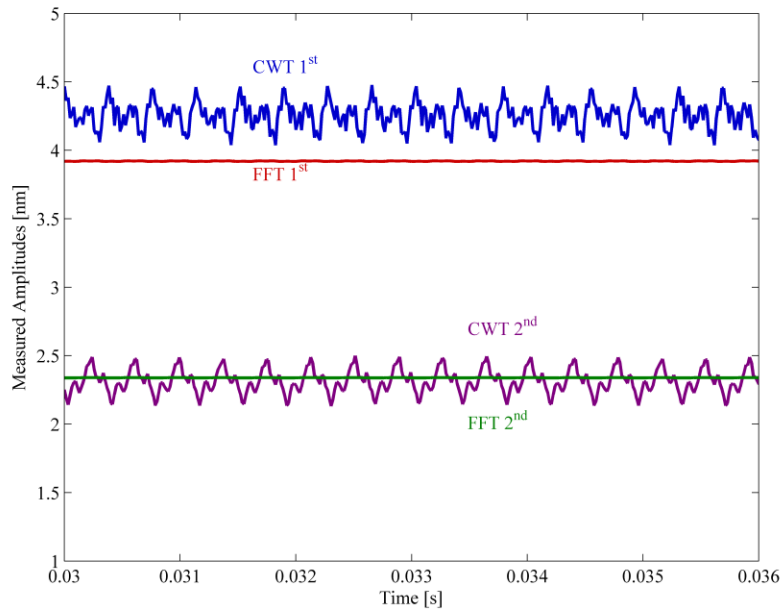


Figure 2.11 The measured amplitudes for the FFT and DTCWT approaches.

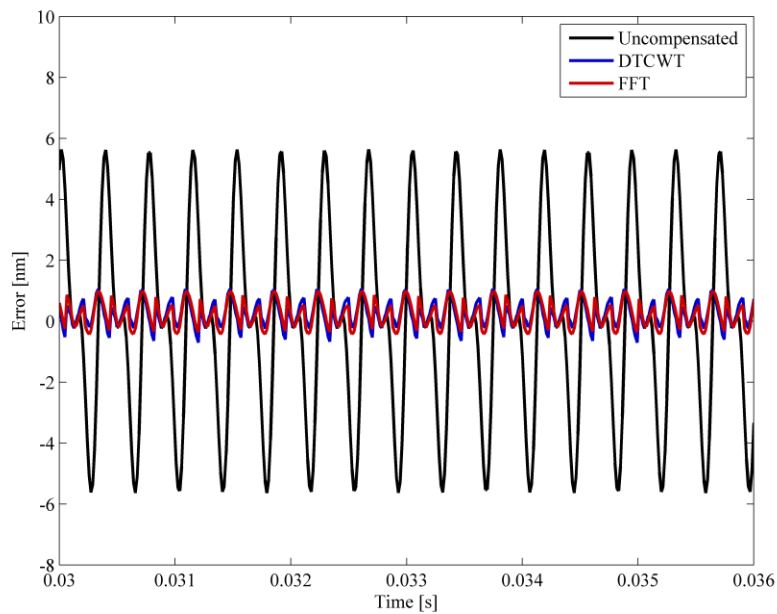


Figure 2.12 The result of periodic error compensation (both DTCWT and FFT approaches) in the time domain.

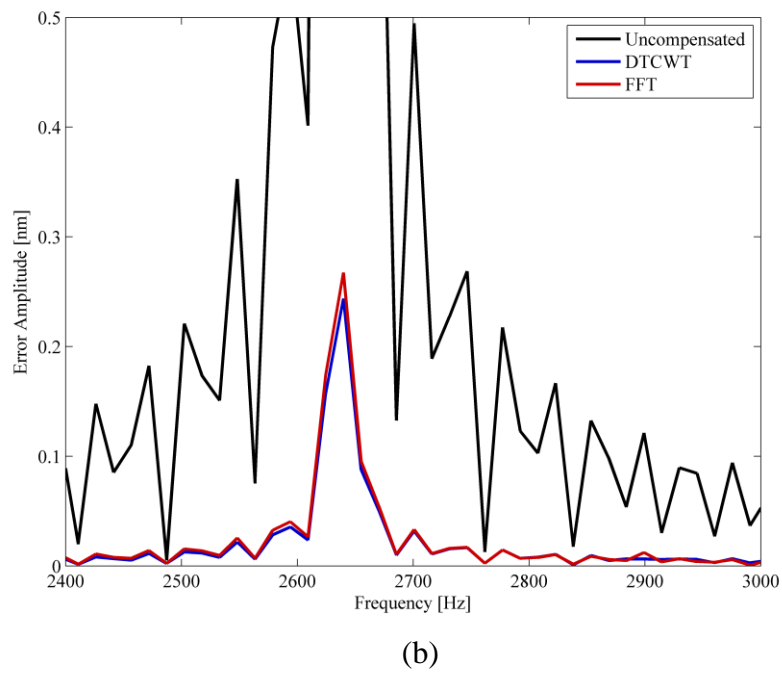
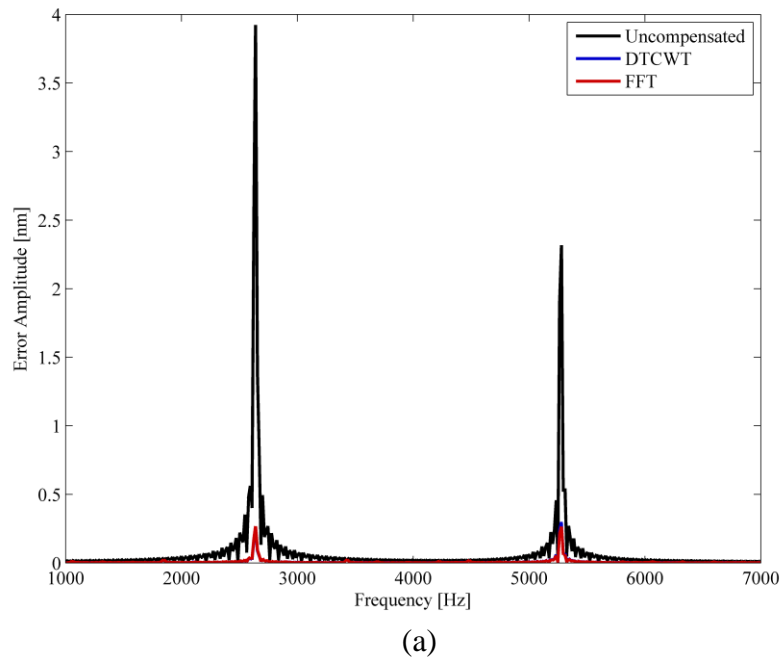


Figure 2.13 (a) The result of periodic error compensation in the frequency domain is presented. (b) Zoomed view of the compensation result for first order periodic error.

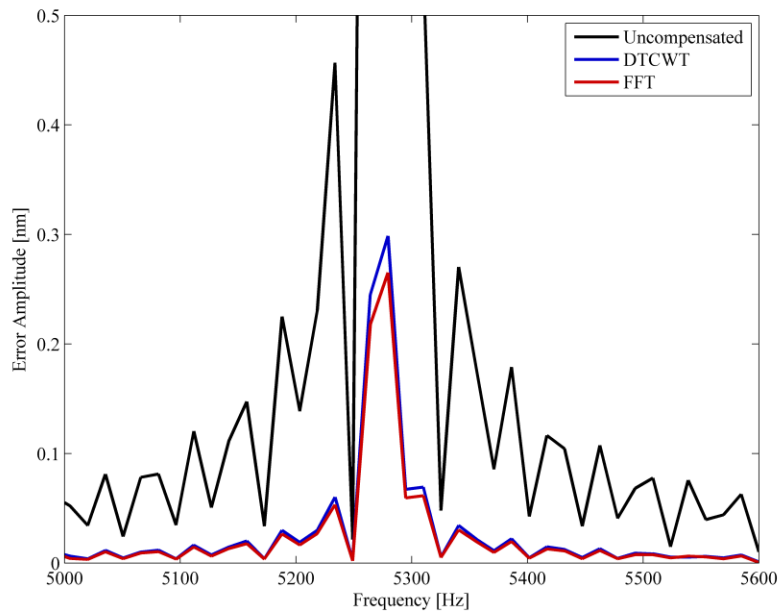


Figure 2.13 (continued) (c) Zoomed view of the compensation result for second order periodic error.

2.8 EXTENDED APPLICATION ON NON-CONSTANT VELOCITY MOTION

One major advantage of the novel wavelet-based approach is that it can compensate periodic error during non-constant velocity motion. Not only did the wavelet-based approach demonstrate better results for constant velocity motions but the traditional frequency domain approach cannot be applied to non-constant motion profiles. This is because the FFT based approach to measuring periodic error amplitude assumes stationary signals during the period covered by the measurement array. However, for non-constant velocity motion, the periodic error time period and frequency is not constant although the spatial period is constant [25]. This section extends the application of this wavelet-based approach to non-stationary signals. Both simulated and experimental non-constant velocity motions with constant periodic error amplitudes are discussed to

validate the effectiveness of the novel algorithm. Also, compensation results of varying amplitude periodic errors and higher order periodic errors imposed in the displacement are displayed. Besides, the result of algorithm implementation on the hardware is shown.

2.8.1 COMPENSATION OF PERIODIC ERROR IN THE SIMULATED NON-CONSTANT VELOCITY MOTION

The simulated displacement here used exactly same interferometer parameters as in Section 2.7.1. In this case, however, the velocity of the target motion is not constant. The non-stationary signal used in the simulation is an accelerating motion signal where first and second order periodic errors (amplitudes 4 nm and 2 nm, respectively) are superimposed during a constant acceleration (3000 mm/min^2) displacement as shown in Figure 2.14.

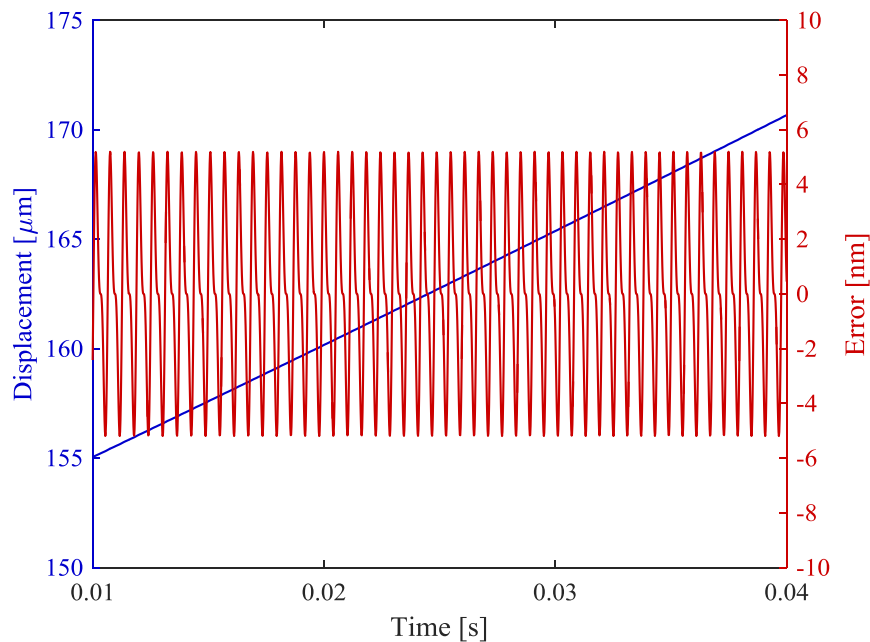


Figure 2.14 Accelerating motion at 50 mm/min^2 and periodic error with magnitudes of 4 nm and 2.5 nm for first and second order.

The results of ridge detection, phase detection, amplitude detection, and overall periodic error compensation are shown in Figures 2.15-17.

The ridge is first detected using Equation 2.7. The performance of the ridge detection portion of the algorithm is evaluated using the simulated displacement signal shown in Figure 2.14. The measured DTCWT ridge for this signal is displayed in Fig. 2.15. The decreasing ridge shown in the figure means the periodic error frequency and the motion velocity are increasing since the frequency is inversely related to the scale in the CWT.

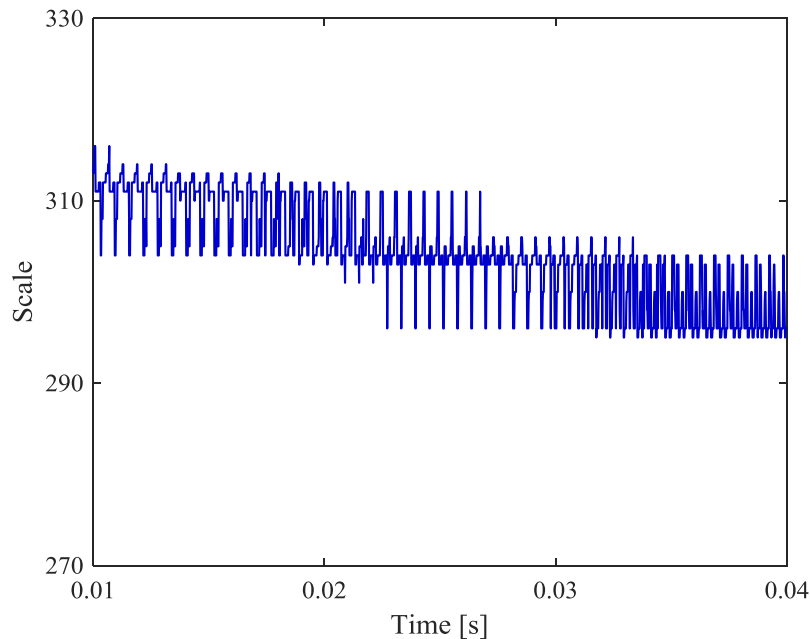


Figure 2.15 The measured DTCWT ridge for the error signal (simulated non-constant velocity motion).

The periodic error amplitudes are then identified using the DTCWT approach. The true values for first and second order periodic errors are 4 nm and 2 nm .The

measured amplitudes are shown in Figure 2.16, with the standard deviations of 0.32 nm and 0.17 nm for first and second orders, respectively.

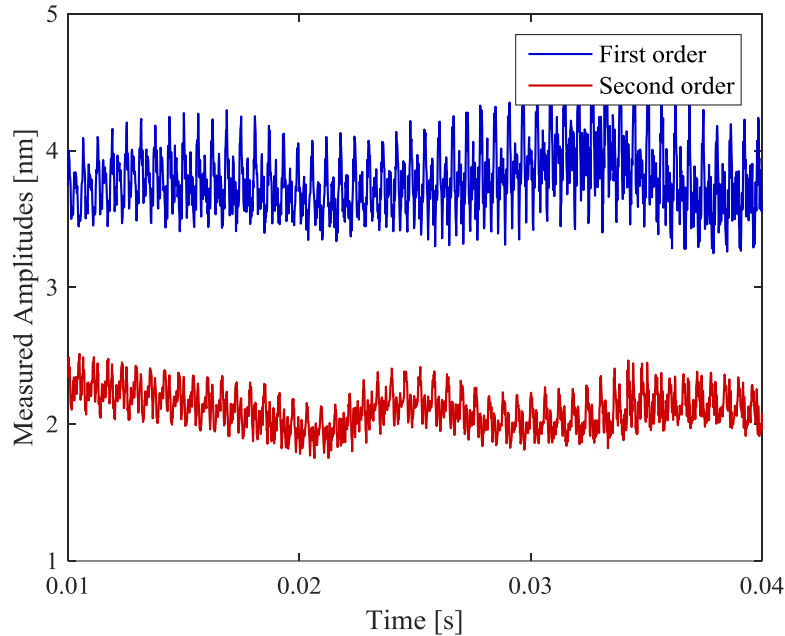


Figure 2.16 The measured amplitudes for the DTCWT approach (simulated non-constant velocity motion).

The overall result of time domain periodic error compensation in real-time using the DTCWT algorithm is displayed in Figure 2.17. The root-mean-square error is reduced from 3.16 nm to 0.56 nm by 82.3%.

2.8.2 COMPENSATION OF PERIODIC ERROR IN THE EXPERIMENTAL NON-CONSTANT VELOCITY MOTION

Experimental data of a small stage was collected for a displacement of 300 μm with parabolic velocity profile (due to constant acceleration of 3000 mm/min^2). Figure 2.18 shows the displacement and periodic error, which was isolated by subtracting a least

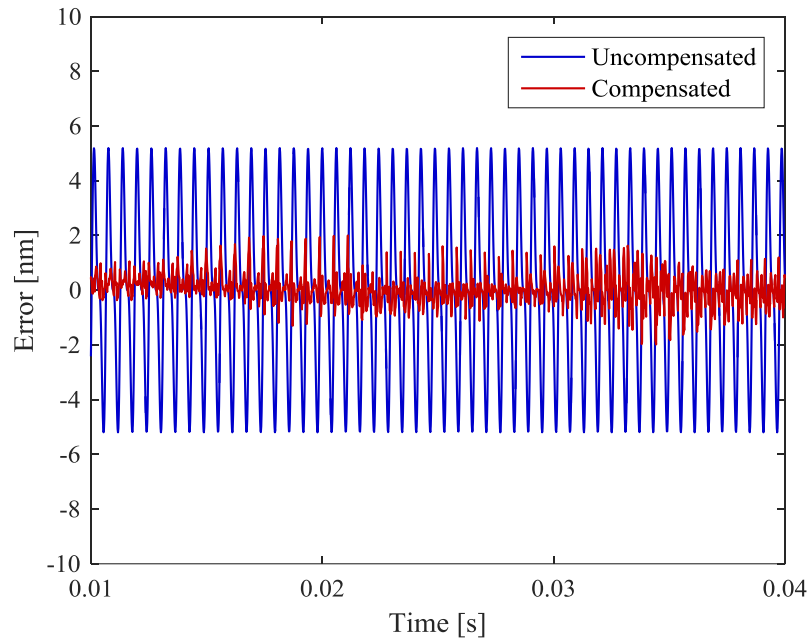


Figure 2.17 The result of periodic error compensation in the time domain (simulated non-constant velocity motion).

squares fit polynomial from the displacement signal. The low frequency drift is caused by an imperfect polynomial fit or non-constant acceleration. The source of this low frequency content may also generically result from vibration or refractive index variation, for example.

Figure 2.19 shows the identified ridge, which is decreasing since the target is accelerating.

Figures 2.20-21 displays the compensated periodic error for the motion. The DTCWT algorithm only removes the reconstructed periodic errors from the displacement. Other errors are not compensated and remain as residuals. These errors are implicitly included in the compensation calculation, as they cannot be eliminated with a low-order polynomial fit. This leads to spikes at some locations in the compensated

result. Overall, the compensated result is results in significant periodic error compensation and reduces the RMS error by approximately 75.2%.

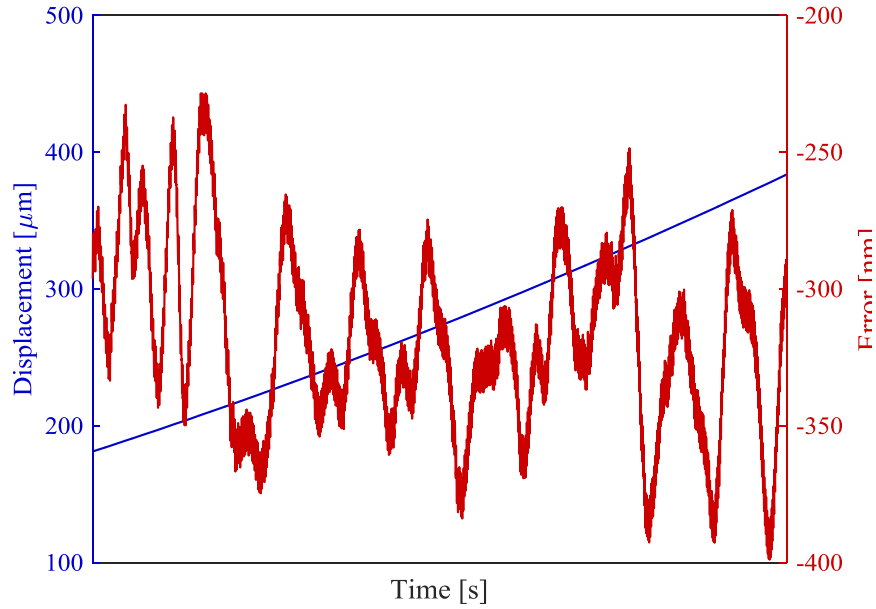


Figure 2.18 Experimental displacement for a 50 mm/min^2 constant acceleration and periodic error.

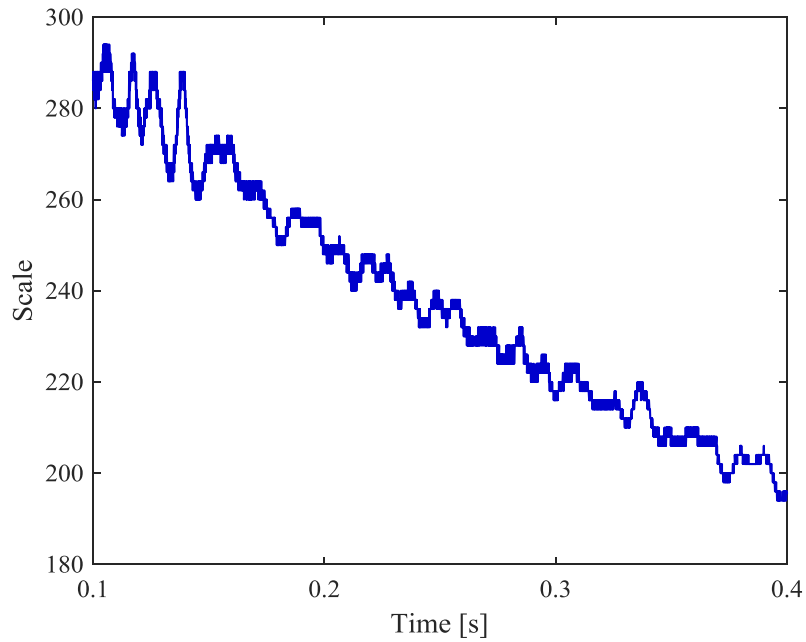


Figure 2.19 The measured DTCWT ridge for the error signal (experimental non-constant velocity motion).

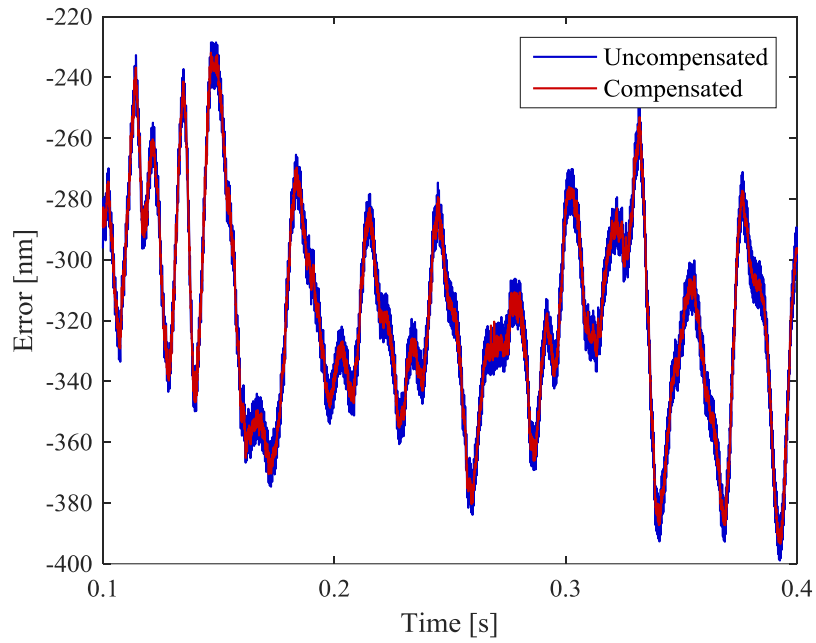


Figure 2.20 The result of periodic error compensation in the time domain (experimental non-constant velocity motion).

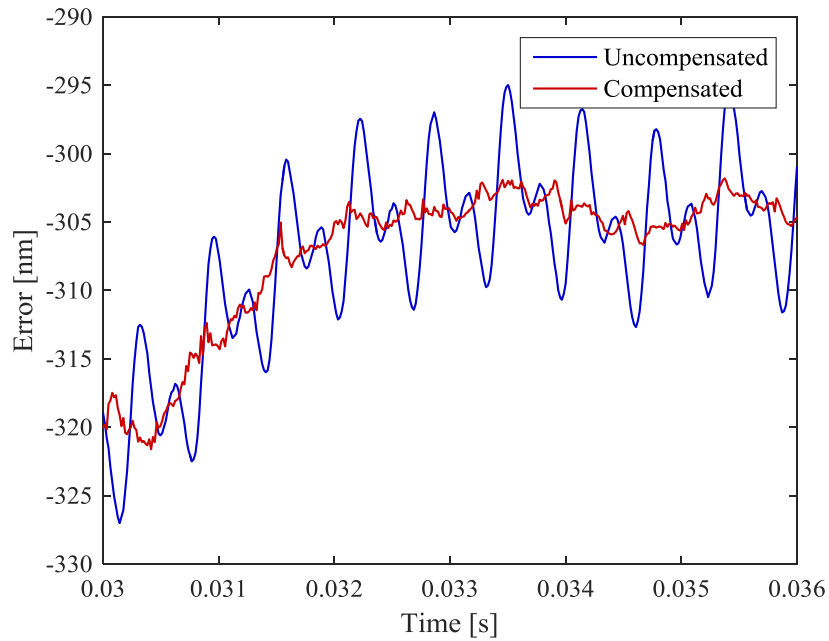


Figure 2.21 Zoomed view of periodic error compensation result (experimental non-constant velocity motion).

2.8.3 COMPENSATION OF PERIODIC ERROR WITH VARYING AMPLITUDES

Fiber-coupled laser sources present the problem that periodic error amplitude can fluctuate due to changes in frequency mixing. The DTCWT approach is also applied to a simulated non-constant velocity motion where the amplitudes of first and second order periodic errors are varying. Again, the displacement is designed based on the same interferometer parameters in Section 2.7.1 to coincide with the real data. The simulated displacement and superimposed first and second order periodic errors are shown in Figure 2.22. The amplitude of first order periodic error is varying from 4.2 nm to 4.8 nm, and the one of second order from 1.8 nm down to 1.2 nm.

The simulated motion is increasing, which can be observed from the descending trend of detected ridge shown in Figure 2.23. The varying amplitudes are measured and displayed in Figure 2.24, with the standard deviations of 0.30 nm and 0.17 nm for first and second orders.

Finally, the overall compensation result in the time domain is shown in Figure 2.25. The root-mean-square error is reduced from 3.36 nm to 0.49 nm by 85.4%.

2.8.4 COMPENSATION OF PERIODIC ERROR WITH HIGHER ORDERS

Typically, first and second order periodic errors occur in the measured target displacement by heterodyne interferometer. In some cases, even higher order periodic errors are imposed in the displacement. The novel wavelet-based algorithm can be also used to compensate the periodic error with order higher than two. This section shows an example of compensating periodic errors up to third order.

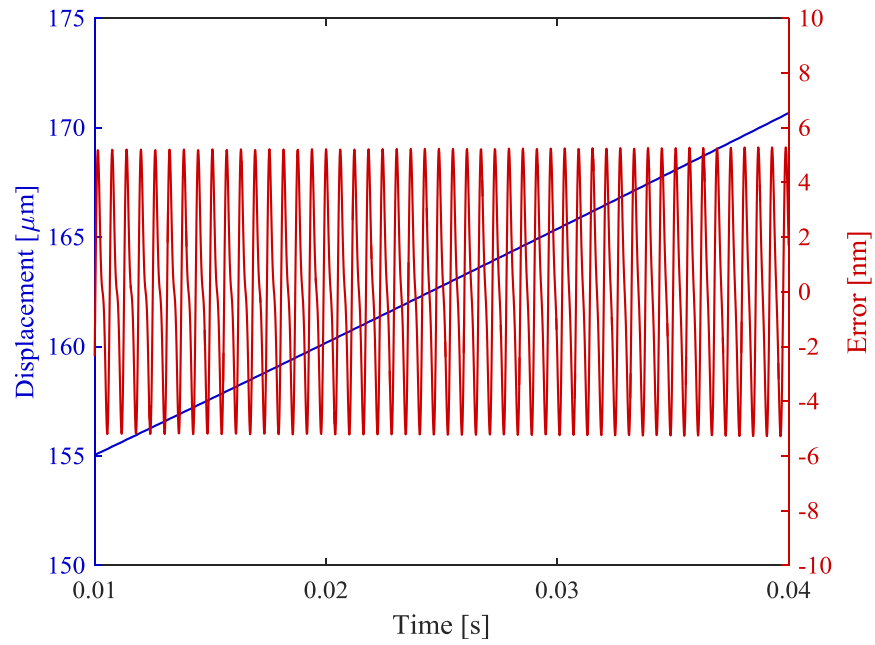


Figure 2.22 Simulated displacement for a 3000 mm/min² constant acceleration and periodic error with varying amplitudes.

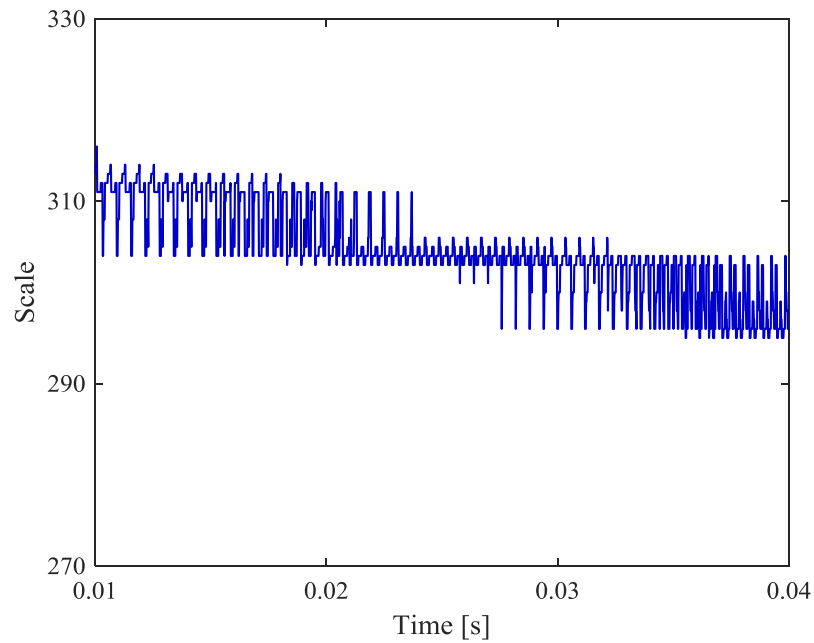


Figure 2.23 The measured DTCWT ridge for the error signal (varying amplitudes).

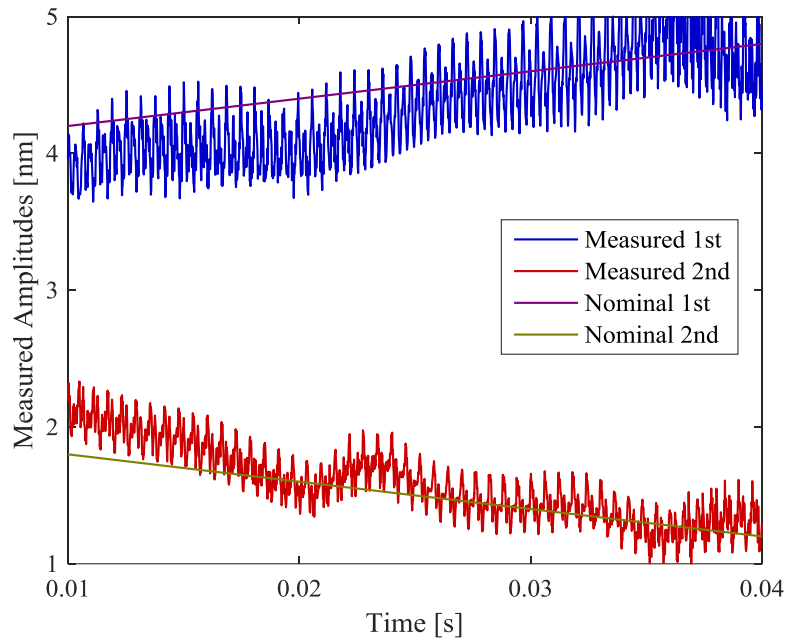


Figure 2.24 The measured amplitudes for the DTCWT approach (varying amplitudes).

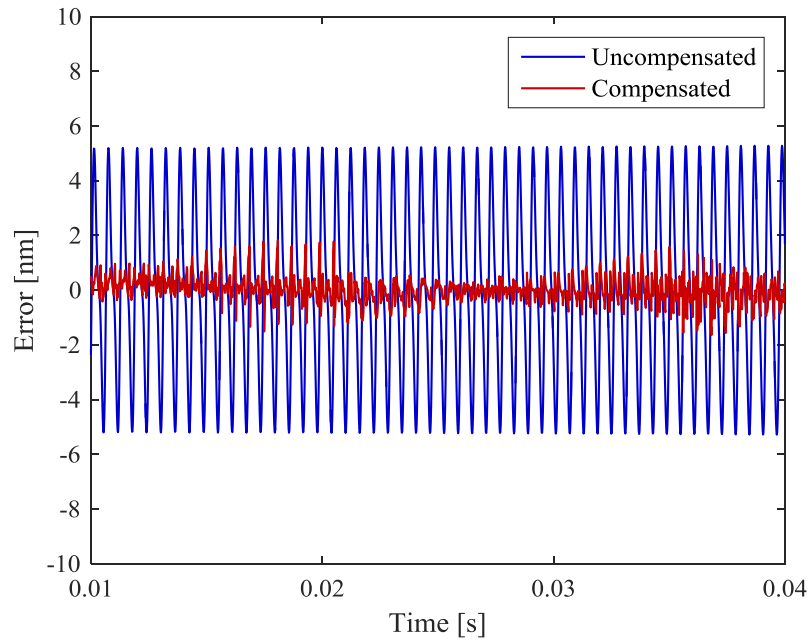


Figure 2.25 The result of periodic error compensation in the time domain (varying amplitudes).

First, second and third order periodic errors (amplitudes of 4 nm, 2.5 nm and 1 nm) in a simulated displacement (1800 mm/min^2 acceleration) are shown in Figure 2.26. Their amplitudes are measured, where the standard deviations are 0.45 nm, 0.11 nm, and 0.16 nm (Figure 2.27). The high order periodic error compensation result is displayed in Figure 2.28. The root-mean-square error is reduced from 2.74 nm to 0.29 nm by 89.4%.

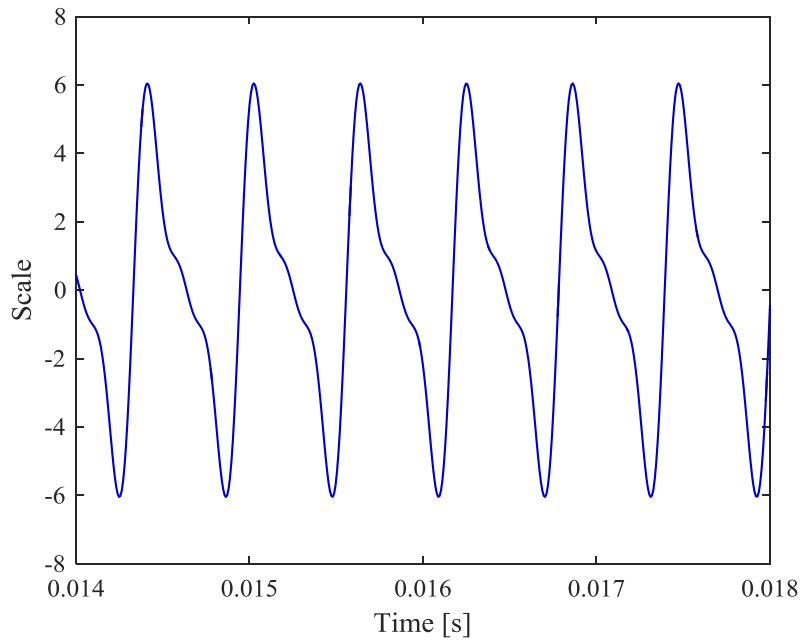


Figure 2.26 Simulated displacement for a 1800 mm/min^2 constant acceleration and periodic error with high orders.

2.9 HARDWARE IMPLEMENTATION

After validating the algorithm for compensating periodic error in different situations on the software, it is also implemented on the hardware to demonstrate that it can be finally applied in practice. The hardware used here is a field-programmable gate array (FPGA), which is an integrated circuit designed to be configured by a customer or a designer after manufacturing. It is common in digital signal processing algorithm

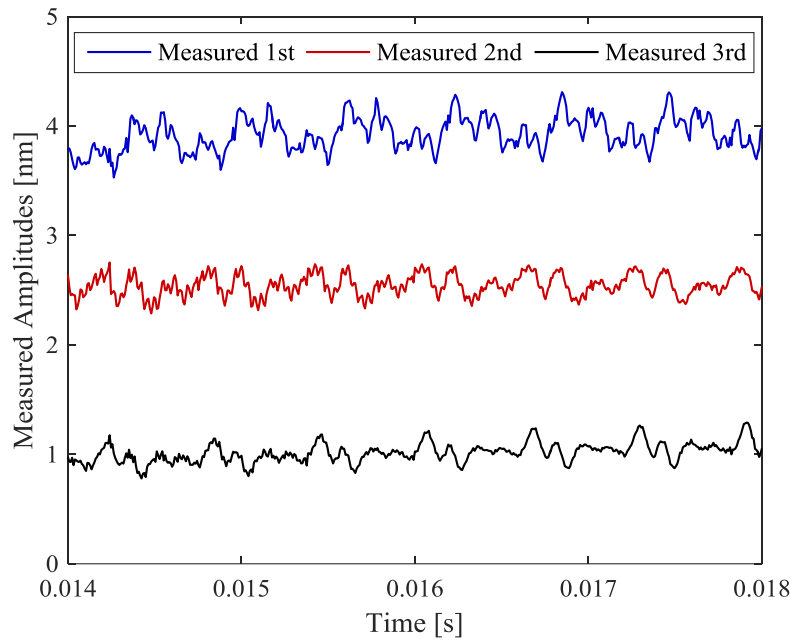


Figure 2.27 The measured amplitudes for the DTCWT approach (high orders).

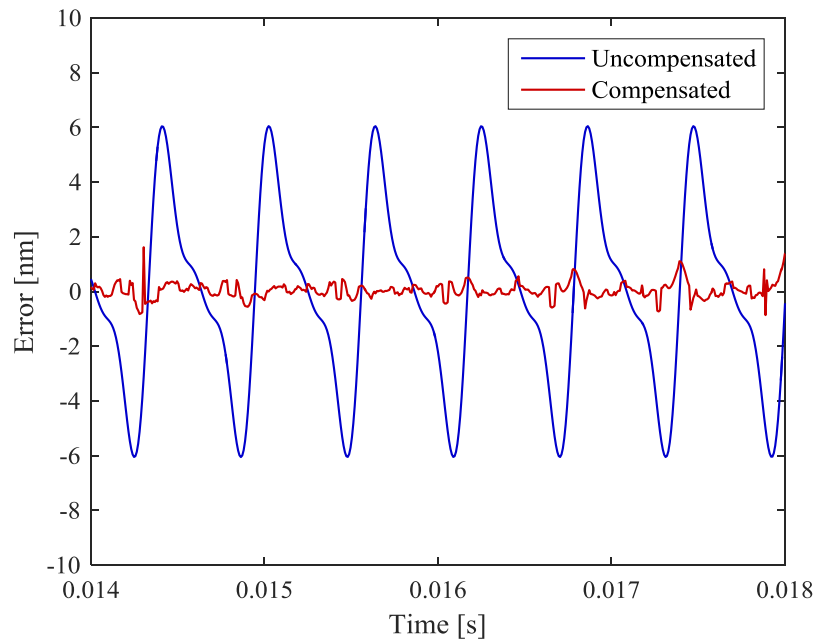


Figure 2.28 The result of periodic error compensation in the time domain (high orders).

development, since it takes advantage of hardware parallelism (it can accomplish many calculations per clock cycle), and has no fabrication cost (it can program repeatedly).

The algorithm is programmed in National Instruments (NI) FPGA module, and implemented on DSP-focused Xilinx Kintex-7 FPGA (NI PXIe-7975R FlexRIO FPGA Module, specifications on Table 2.1), which is installed on NI PXIe-1085 PXI Express Chassis (Figure 2.30). PXI is a rugged PC-based platform for measurement and automation systems. Data and program can be downloaded from PC to PXI system. Real-time operating system is installed on the PXI system. PXI system can run real-time programs on FPGA module.

Table 2.1 NI PXIe-7975R specifications.

FPGA	Kintex-7 XC7K410T
LUTs	254,200
DSP48 Slices	1,540
Embedded Block RAM	28,620
Default time base	40 MHz
Data transfers	DMA, interrupts, programed I/O
Onboard memory size	2 GB single bank



FPGA Module

Figure 2.29 NI FPGA module and PXI platform.

From receiving a new data point to outputting a compensated data point, the algorithm is operated in 545 clock cycles on the FPGA board. The clock is 200 MHz. Therefore, for each new point, it costs $2.725 \mu\text{s}$ to output the compensated point, which means the algorithm has a $2.725 \mu\text{s}$ time delay for compensating periodic error in real-time. The sampling frequency used here remains 62.5 kHz. This implies the time interval between two neighboring data points is $16 \mu\text{s}$. In this case, the algorithm can be completed for current point before next point arriving.

Figure 2.31 shows the periodic error compensation result for a constant velocity motion. The RMS error is reduced by approximately 91.8%.

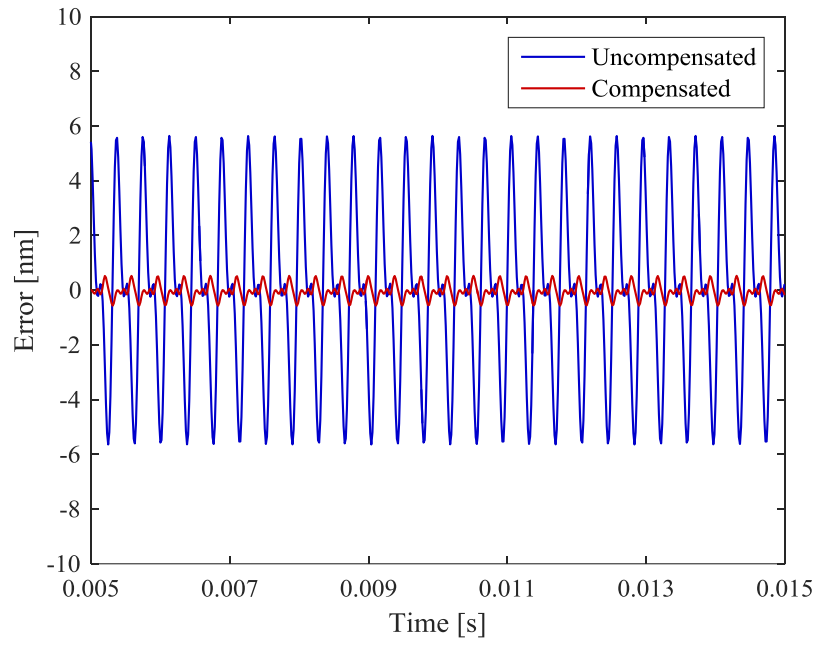


Figure 2.30 The result of periodic error compensation in the time domain (hardware).

CHAPTER 3

STRUCTURAL HEALTH MONITORING IN DRY CASK STORAGE

In this chapter, another application of wavelet analysis will be introduced and investigated. Used nuclear fuel will be stored in dry cask storage for 20 to more than 100 years after moving from spent fuel pools. To avoid any corrosion or degradation, fuel must be dried before storing for such a long period. During drying process, the conditions of failed fuel rods in dry cask storage should be monitored to acquire any possible structure change in real-time. An integrated approach based on wavelet analysis will be developed to monitor the conditions and detect the changes.

3.1 BACKGROUND

Currently, there are nearly 70,000 t of used nuclear fuel in spent fuel pools or dry cask storage increasing by nearly 2,000 t per year. After being used in a reactor, this fuel is stored for 3 to 5 years in spent fuel pools. Eventually the spent fuel will be placed into dry cask storage for another 20 years to more than 100 years. This fuel is now stored in 34 states. The cooling time of this fuel ranges from a minimum of 5 years. Each assembly emits thermal energy from radioisotope decay of 0.5 kW to 1 kW. From the spent fuel pool, used fuel rod assemblies are loaded into casks (Figure 3.1) underwater. This water must be removed to avoid corrosion or potential creation of combustion gases [109].

Combustion gases such as H₂ and O₂ can be generated by radiolysis. The accepted

drying process includes evacuation of the canister to less than 3 Torr and maintaining for 30 minutes after disconnecting from the pumping system [109-111]. An alternative approach is to recirculate helium in the canister to achieve the same water vapor pressure as in vacuuming the canister.

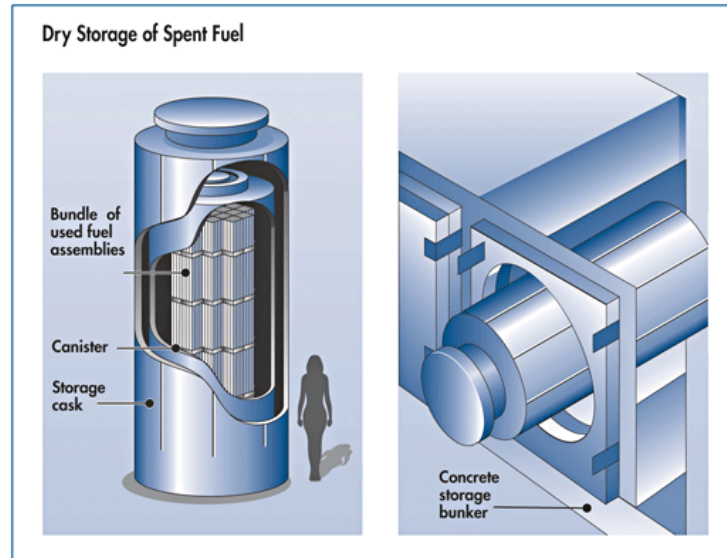


Figure 3.1 Illustration of dry storage.

The temperature of rods in the drying process is subject to vary due to the removal of the heat, since pressure, flow rates and some other system parameters are changing in this process. The maximum of the rod temperature should not exceed $400\text{ }^{\circ}\text{C}$ [110, 112], which is the limit of peak but not average. The number of thermal cycles of heating and cooling for the fuel rods in the drying process is also limited to 10, where the clad temperature varies by more than $65\text{ }^{\circ}\text{C}$ [110].

Structural health monitoring is a process of implementing a damage detection and characterization strategy for an engineering structure. Here, damage is referred as the change from the original system which may cause adverse effects to the system. SHM

may also be used to predict the remaining life of the structure at critical locations. Another potential application is to embed SHM sensors into a new structure to save weight and cost. SHM integrates a wide range of techniques, including sensors, smart materials, data acquisition and signal processing, etc. Five main objectives of SHM are defect detection and location, defect identification, defect assessment, defect monitoring, and failure prediction [113].

There are different methodologies to monitor the structure. One that will be used in this research is ultrasonic testing. In this case, ultrasonic guided waves will be excited and propagate along the designed path. Compared with traditional point-to-point bulk waves, the guided waves can travel in long distances with little amplitude loss. Particularly, the guided waves in a cylinder will be studied and used.

3.2 PROBLEM DEFINITION

Fuel rod failures (for example see Figure 3.2) typically occur in the first 100 days. There are two main failure modes. One is grid-rod fretting, which result in a small square hole at the grid dimple point. The leak path may not be tortuous but partially blocked by the dimple. Another failure mode is axial split because of pellet clad interaction (PCI), which could be dominant in the higher heat flux zones. Since failures occur in fuel rod early life, there will be little creep down of the cladding, which makes the ingress of coolant into the failed fuel rods possible. In this case, the failed rods will hold water at the lower portion, particularly if axial blankets are used. On the other hand, the surface temperature of the fuel pellets could be nearly 600 °C and the center temperature could be above 1200 °C, because the power is generated at the pellet stack. Hence, most of the

water that is contained in the failed rod exists in the form of superheated steam. The steam will oxidize the inside cladding surface and may result in hydride. The steam will also oxidize the UO_2 and form U_3O_8 . This will lead to an increase in volume and then cause the pellet to fragment into small pieces. If this is the case, a considerable amount of water will be retained by the fragmented fuel particles due to these hygroscopic particles with high surface area.

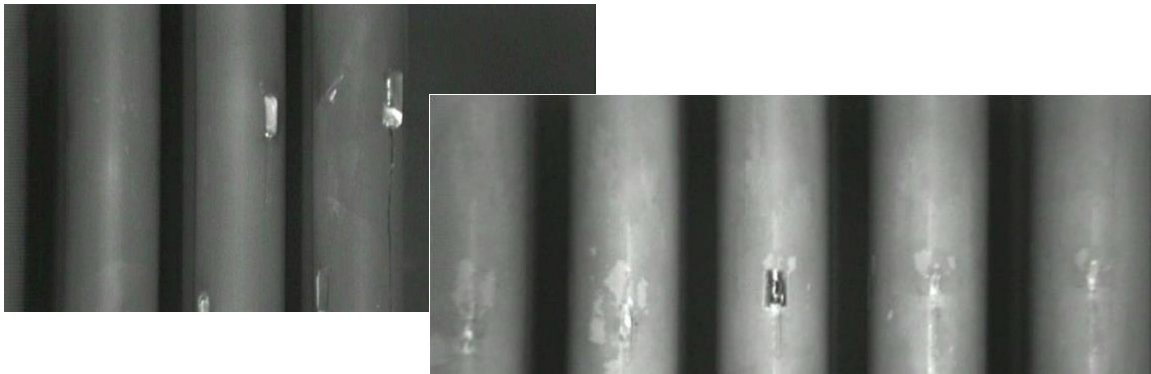


Figure 3.2 Grid to rod fretting failure in the fuel rod.

After the reactor shut down, the steam will condense and fill in the voids in the rods. In the spent fuel pool, little reaction will occur, and therefore, most of the primary coolant will remain unchanged. During the subsequent placement into the storage canister, most of this water will be retained and may not be removed during subsequent evacuation, since the path for water flow through the point of failure in the cladding could be tortuous. A substantial quantity of water may still be retained through the absorption on the U_3O_8 particles even if the liquid water is removed. The absorbed water could be slowly removed over time since the fuel is under high vacuum condition and modest temperature where the equilibrium partial pressure of steam is high.

During the drying process of evacuation, if this operation is rapid (e.g., only a few hold points during the pressure drop from atmosphere to vacuum inside the canister), the water retained in the failed rods is likely to form ice. In this case, the ice crystal is difficult to remove. Moreover, if the ice forms at some critical location on the water flow path (e.g., the failure on the fuel rod), it will prevent all the retained water inside the rod from being removed.

Since the canister is sealed during evacuation, it is difficult to directly observe the condition inside (Figure 3.3). A systematic approach is needed to determine if the fuel rod is failed. If it occurs, some related information, such as the location of the failure (Figure 3.4), and if there is any ice formation, needs to be detected to guide the later operations in the evacuation. This detection is required to be conducted in real-time, since certain system parameters will be recorded when there is any remarkable condition change (e.g., ice formation) inside the fuel rod.



Figure 3.3 An example of a sealed chamber to accommodate the mock fuel rod assembly.



Figure 3.4 Defect on a mock failed fuel rod.

3.3 RESEARCH OBJECTIVE

The focus of this study is on the structural health monitoring in fuel rods using the ultrasonic guided wave technique. Piezoelectric ceramic Lead Zirconate Titanate (PZT) transducers are used to produce cylindrical guided waves through fuel rods to identify and quantify the critical structural health information. In order to obtain substantial information, the transmitted waves include multiple frequencies. Therefore, the received signal from the fuel rods also contains components of different frequencies. To obtain useful information from this multi-frequency signal, the continuous wavelet transform is performed. The relationship will be built between the system conditions and the CWT coefficients. Eventually, if any condition changes inside the canister, it can be observed from the change in the CWT coefficients. The typical conditions that are to be monitored include:

- The location and size of the failure on the fuel rod
- The ice formation inside or on the failed rod.
- The ice level inside the failed rod.

3.4 GUIDED WAVES IN PIPES

Ultrasonic guided waves are commonly used in plate and hollow cylinder inspections. It is possible to inspect long lengths from a single probe position using the guided waves. It has excellent defect detection sensitivities and long inspection distances. In a hollow cylinder, the guided waves may travel in the circumferential or axial direction. The wave behavior can be described by solving the governing wave equations based on the appropriate boundary conditions. This research will focus on the guided waves propagating in axial directions in cylindrical structures.

3.4.1 LITERATURE REVIEW

3.4.1.1 GUIDED WAVE PROPAGATION IN A CYLINDER

The first theoretical study of guided waves was conducted by Rayleigh more than one century ago [114]. However, the ultrasonic guided wave technique began to apply and develop in the mid-1980s. With the efforts of many pioneers, the guided wave technique has shown potential in the field of structural health monitoring due to its long-range testing ability and efficiency compared to the traditional bulk wave methods [115]. Guided waves can propagate in different structures and result in different behaviors, such as a Lamb wave in a plate, a Rayleigh wave in a free surface, or longitudinal and torsional waves in a cylinder. The theory of different guided waves was investigated by

many pioneers [115-121]. A comprehensive review was given on the historical development and applications of guided waves [122, 123].

Guided waves in a hollow cylinder (pipeline) can propagate in two directions. One is the circumferential direction, including the circumferential Lamb type wave and the circumferential shear horizontal (SH) waves [124-127]. Many applications of this type of waves can be found in [128-131]. Another one is the axial direction, including the longitudinal and torsional waves with both axisymmetric and non-symmetric (flexural) modes. Compared to the waves in the circumferential direction, the guided waves in the axial direction can travel in long distances. The investigations of axisymmetric waves can be found in [132-138], including theoretical solutions and experimental excitation methods. In some cases, however, the axisymmetric waves are not well-suited for SHM. Related studies were reported in [139-141].

3.4.1.2 FINITE ELEMENT METHOD

Analytical method can be used to solve wave propagation problem for simple geometries [142, 143]. When the structure is complex (for instance, structure with some defects), it is usually difficult to obtain the exact solution. In these cases, numerical methods may be used. Typical numerical methods include elastodynamic finite integration technique (EFIT) [144-146], spectral element method (SEM) [147, 148], boundary element method (BEM) [149-151], finite difference method (FDM) [152-155], and finite element method (FEM) [156-158].

The FEM is a numerical technique for obtaining approximate solutions for partial differential equations [156-158]. It transforms the governing equations into weak form

(integral representations of the governing equations). The analysis domain is discretized to a set of finite elements. FEM approximates the PDE solutions in the analysis domain. FEM has served as a primary numerical tool to simulate the elastic wave propagation. This work uses FEM to solve and simulate the wave propagation. Commonly used FEM software includes ABAQUS, COMSOL, ANSYS, etc [159-161]. With these powerful tools, complicated wave propagation problems can be solved and simulated, from wave interaction with defects, to wave propagation in complex structures, to nonlinear guided wave propagation [159-161]. Here ANSYS is used in this work.

3.4.1.3 WAVELET ANALYSIS IN DEFECT DETECTION

Defect detection in pipes with signal processing techniques is widely used. Recently the wavelet analysis has become a popular tool to be performed on the received signals. Cho [162] studied the subsurface lateral defect detection with wavelet transform on propagating Lamb waves. Abbate [163] processed signals with nonstationary spectral contents using wavelet transform. Kaya [164] investigate the approach to detect flaws in stainless steel samples using wavelet decomposition. Murase and Kawashima [165] showed that for a thin aluminum plate, the group velocity curves can be plotted when Gabor functions are chosen as the mother wavelet among different wavelet functions. Ahmad and Kundu [166] plotted group velocities for defective and defect-free cylindrical pipes from experimental data using Gabor wavelet functions. Ahmad [167] reported the study of identifying the defects in transmission pipes with Daubechies wavelet functions.

3.4.2 GUIDED WAVE THEORY IN PIPES

The guided wave theory discussed here is about the ones in the axial direction, since it can travel at long distances and will be used in this research. Gazis [133] first obtained the 3-dimensional solution of axial-direction guided waves with displacement fields in the axial, radial and angular directions. By solving the wave propagation equation in a hollow cylinder with traction free boundary conditions (Figure 3.5), the solution can be acquired. The longitudinal waves have dominant particle motions in either the radial or the axial directions and the torsional waves have dominant particle motions in the angular direction.

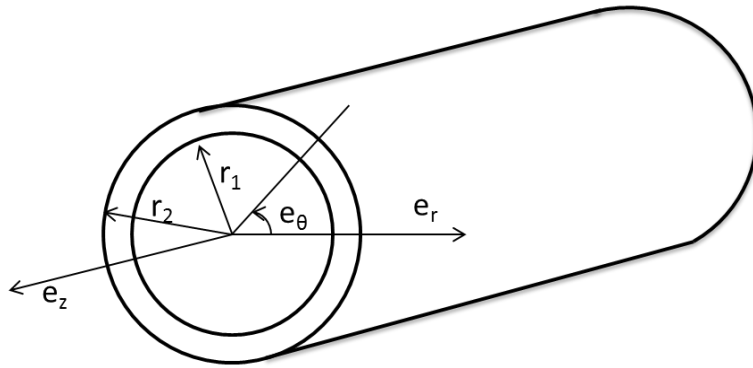


Figure 3.5 Cylindrical coordinates of a hollow cylinder.

The Navier's governing wave equation for guided wave propagation can be written as

$$\mu \nabla^2 \vec{u} + (\lambda + \mu) \nabla \nabla \cdot \vec{u} = \rho \frac{\partial^2 \vec{u}}{\partial t^2}, \quad (3.1)$$

where \vec{u} is the displacement field, t is the time, λ and μ are Lamé constants, and ρ is the density. Six traction-free boundary conditions at the inner ($r = r_1$) and outer ($r = r_2$) surfaces are

$$\sigma_{rr} = \sigma_{\theta\theta} = \sigma_{zz} = 0, \quad \text{at } r = r_1 \text{ and } r = r_2. \quad (3.2)$$

Assume the cylinder is isotropic, Helmholtz decomposition can be used:

$$\vec{u} = \nabla\Phi + \nabla \times \vec{H}, \quad (3.3)$$

where Φ is the dilatational scalar potential field, and \vec{H} is the equivoluminal vector potential. Then the displacement \vec{u} can be expressed based on Equations. 3.2 and 3.3:

$$u_r = \frac{\partial\Phi}{\partial r} + \frac{1}{r} \left(\frac{\partial H_z}{\partial \theta} - \frac{\partial H_\theta}{\partial z} \right), \quad (3.4.1)$$

$$u_\theta = \frac{1}{r} \frac{\partial\Phi}{\partial \theta} - \left(\frac{\partial H_z}{\partial r} - \frac{\partial H_r}{\partial z} \right), \quad (3.4.2)$$

$$u_z = \frac{\partial\Phi}{\partial z} + \frac{1}{r} \left(H_\theta + r \frac{\partial H_\theta}{\partial r} - \frac{\partial H_r}{\partial \theta} \right). \quad (3.4.3)$$

Assuming the hollow cylinder is infinity long, the gauge invariance can be defined as:

$$\nabla \cdot \vec{H} = 0. \quad (3.5)$$

Equation 3.5 can be used to separate longitudinal and shear waves into:

$$\nabla^2 \Phi = \frac{1}{c_1} \frac{\partial^2 \Phi}{\partial t^2}, \quad (3.6)$$

$$\nabla^2 \vec{H} = \frac{1}{c_2} \frac{\partial^2 \vec{H}}{\partial t^2}, \quad (3.7)$$

where $c_1 = \sqrt{\frac{\lambda + 2\mu}{\rho}}$ is the longitudinal bulk wave velocity, and $c_2 = \sqrt{\frac{\mu}{\rho}}$ is the shear

bulk wave velocity.

To separate variables, the solutions can be assumed as:

$$\Phi = f(r) \cos n\theta \cos(\omega t + kz), \quad (3.8.1)$$

$$H_r = g_r(r) \sin n\theta \sin(\omega t + kz), \quad (3.8.2)$$

$$H_\theta = g_\theta(r) \cos n\theta \sin(\omega t + kz), \quad (3.8.3)$$

$$H_z = g_z(r) \sin n\theta \cos(\omega t + kz), \quad (3.8.4)$$

where $f(r)$, $g_r(r)$, $g_\theta(r)$ and $g_z(r)$ are unknown potentials as functions of radius,

$n = 0, 1, 2, \dots$ is the circumferential order of a wave mode, and k is the wavenumber.

Substitute Equation 3.8 into Equations 3.6 and 3.7 to obtain:

$$f'' + \frac{1}{r} f' - \frac{n^2}{r^2} f + \alpha^2 f = 0, \quad (3.9.1)$$

$$g_3'' + \frac{1}{r} g_3' - \frac{n^2}{r^2} g_3 + \beta^2 g_3 = 0, \quad (3.9.2)$$

$$g_1'' + \frac{1}{r} g_1' - \frac{(n+1)^2}{r^2} g_1 + \beta^2 g_1 = 0, \quad (3.9.3)$$

$$g_2'' + \frac{1}{r} g_2' - \frac{(n-1)^2}{r^2} g_2 + \beta^2 g_2 = 0, \quad (3.9.4)$$

where $g_1 = \frac{g_r - g_\theta}{2}$, $g_2 = \frac{g_r + g_\theta}{2}$, $\alpha = \sqrt{\frac{\omega^2}{c_1^2} - k^2}$, and $\beta = \sqrt{\frac{\omega^2}{c_2^2} - k^2}$. The unknowns

$f(r)$, $g_r(r)$, $g_\theta(r)$ and $g_z(r)$ in Equation 3.8 can be expressed as the solutions of the

Bessel equations in Equation 3.9:

$$f = AZ_n(\alpha_1 r) + BW_n(\alpha_1 r), \quad (3.10.1)$$

$$g_3 = A_3 Z_n(\beta_1 r) + B_3 W_n(\beta_1 r), \quad (3.10.2)$$

$$2g_1 = g_r - g_\theta = 2A_1 Z_{n+1}(\beta_1 r) + 2B_1 W_{n+1}(\beta_1 r), \quad (3.10.3)$$

$$2g_2 = g_r + g_\theta = 2A_2 Z_{n-1}(\beta_1 r) + 2B_2 W_{n-1}(\beta_1 r), \quad (3.10.4)$$

where $\alpha_1 r = |\alpha r|$, $\beta_1 r = |\beta r|$, and Z indicates a Bessel function J or I while W indicates a modified Bessel function Y or K, which depends on that α and β are real or imaginary (Table 3.1).

Table 3.1 Bessel function types used at different frequencies.

Frequency interval	α and β	Bessel function types
$c_1 k < \omega$	$\alpha^2 > 0, \beta^2 > 0$	$J(\alpha r), Y(\alpha r), J(\beta r), Y(\beta r)$
$c_2 k < \omega < c_1 k$	$\alpha^2 < 0, \beta^2 > 0$	$I(\alpha_1 r), K(\alpha_1 r), J(\beta r), Y(\beta r)$
$\omega < c_2 k$	$\alpha^2 < 0, \beta^2 < 0$	$I(\alpha_1 r), K(\alpha_1 r), I(\beta_1 r), K(\beta_1 r)$

According to the gauge invariance property, any of the terms g_1, g_2 or g_3 could be set to zero. Let $g_2 = 0$ and use 6 boundary conditions in Equation 3.2. Then the displacement field can be solved by substituting Equations 3.8 and 3.10 into Equation 3.4:

$$u_r = \left[f' + \frac{n}{r} g_3 + k g_1 \right] \cos n\theta \cos(\omega t + kz) = U_r(r) \cos n\theta \cos(\omega t + kz), \quad (3.11.1)$$

$$u_\theta = \left[-\frac{n}{r} f + k g_1 - g_3 \right] \sin n\theta \cos(\omega t + kz) = U_\theta(r) \sin n\theta \cos(\omega t + kz), \quad (3.11.2)$$

$$u_z = \left[-k f - g_1' - (n+1) \frac{g_1}{r} \right] \cos n\theta \sin(\omega t + kz) = U_z(r) \cos n\theta \sin(\omega t + kz), \quad (3.11.3)$$

where $U_r(r), U_\theta(r)$ and $U_z(r)$ are the wave field distributions in the radial direction [115].

From Equations 3.11, the stress can be derived and then applied to the six traction free boundary conditions with a matrix form shown in Equation 3.12:

$$\begin{bmatrix} c_{11} & c_{12} & c_{13} & c_{14} & c_{15} & c_{16} \\ c_{21} & c_{22} & c_{23} & c_{24} & c_{25} & c_{26} \\ c_{31} & c_{32} & c_{33} & c_{34} & c_{35} & c_{36} \\ c_{41} & c_{42} & c_{43} & c_{44} & c_{45} & c_{46} \\ c_{51} & c_{52} & c_{53} & c_{54} & c_{55} & c_{56} \\ c_{61} & c_{62} & c_{63} & c_{64} & c_{65} & c_{66} \end{bmatrix}_{6 \times 6} \begin{Bmatrix} A \\ B \\ A_1 \\ B_1 \\ A_3 \\ B_3 \end{Bmatrix}_{6 \times 1} = [C]_{6 \times 6} \begin{Bmatrix} A \\ B \\ A_1 \\ B_1 \\ A_3 \\ B_3 \end{Bmatrix}_{6 \times 1} = 0, \quad (3.12)$$

where A, B, A₁, B₁, A₃, B₃ are unknown amplitudes,

$$c_{11} = [2n(n-1) - (\beta^2 - k^2)a^2]Z_n(\alpha_1 a) + 2\lambda_1 \alpha_1 a Z_{n+1}(\alpha_1 a)$$

$$c_{12} = 2k\beta_1 a^2 Z_n(\beta_1 a) - 2ka(n+1)Z_{n+1}(\beta_1 a)$$

$$c_{13} = 2n(n-1)Z_n(\beta_1 a) - 2\lambda_2 n \beta_1 a Z_{n+1}(\beta_1 a)$$

$$c_{14} = [2n(n-1) - (\beta^2 - k^2)a^2]W_n(\alpha_1 a) + 2\alpha_1 a W_{n+1}(\alpha_1 a)$$

$$c_{15} = 2\lambda_2 k \beta_1 a^2 W_n(\beta_1 a) - 2(n+1)ka W_{n+1}(\beta_1 a)$$

$$c_{16} = 2n(n-1)W_n(\beta_1 a) - 2n\beta_1 a W_{n+1}(\beta_1 a)$$

$$c_{21} = -2n(n-1)Z_n(\alpha_1 a) + 2\lambda_1 n \alpha_1 a Z_{n+1}(\alpha_1 a)$$

$$c_{22} = k\beta_1 a^2 Z_n(\beta_1 a) - 2ka(n+1)Z_{n+1}(\beta_1 a)$$

$$c_{23} = -[2n(n-1) - \beta^2 a^2]Z_n(\beta_1 a) - 2\lambda_2 \beta_1 a Z_{n+1}(\beta_1 a)$$

$$c_{24} = -2n(n-1)W_n(\alpha_1 a) + 2n\alpha_1 a W_{n+1}(\alpha_1 a)$$

$$c_{25} = \lambda_2 k \beta_1 a^2 W_n(\beta_1 a) - 2ka(n+1)W_{n+1}(\beta_1 a)$$

$$c_{26} = -[2n(n-1) - \beta^2 a^2]W_n(\beta_1 a) - 2\beta_1 a W_{n+1}(\beta_1 a)$$

$$c_{31} = -2nka Z_n(\alpha_1 a) + 2\lambda_1 k \alpha_1 a^2 Z_{n+1}(\alpha_1 a)$$

$$c_{32} = -n\beta_1 a Z_n(\beta_1 a) + (\beta^2 - k^2)a^2 Z_{n+1}(\beta_1 a)$$

$$c_{33} = -nkaZ_n(\beta_1 a)$$

$$c_{34} = -2nkaW_n(\alpha_1 a) + 2k\alpha_1 a^2 W_{n+1}(\alpha_1 a)$$

$$c_{35} = -\lambda_2 n\beta_1 a W_n(\beta_1 a) + (\beta^2 - k^2) a^2 W_{n+1}(\beta_1 a)$$

$$c_{36} = -nkaW_n(\beta_1 a)$$

The fourth to sixth rows can be obtained by replacing a by b in the expressions of the first three rows. λ_i varies as follows:

$$\begin{aligned} c_1 k < \omega: \quad \lambda_1 = 1, \lambda_2 = 1 \\ c_2 k < \omega < c_1 k: \quad \lambda_1 = -1, \lambda_2 = 1. \\ \omega < c_2 k: \quad \lambda_1 = -1, \lambda_2 = -1 \end{aligned}$$

The dispersion equation (also called the characteristic or frequency equation) can be expressed as a solution in Equation 3.13:

$$|C|_{6 \times 6} = 0. \quad (3.13)$$

Numerical methods (for example, a bisection method in [115]) can be used to solve the dispersion equation.

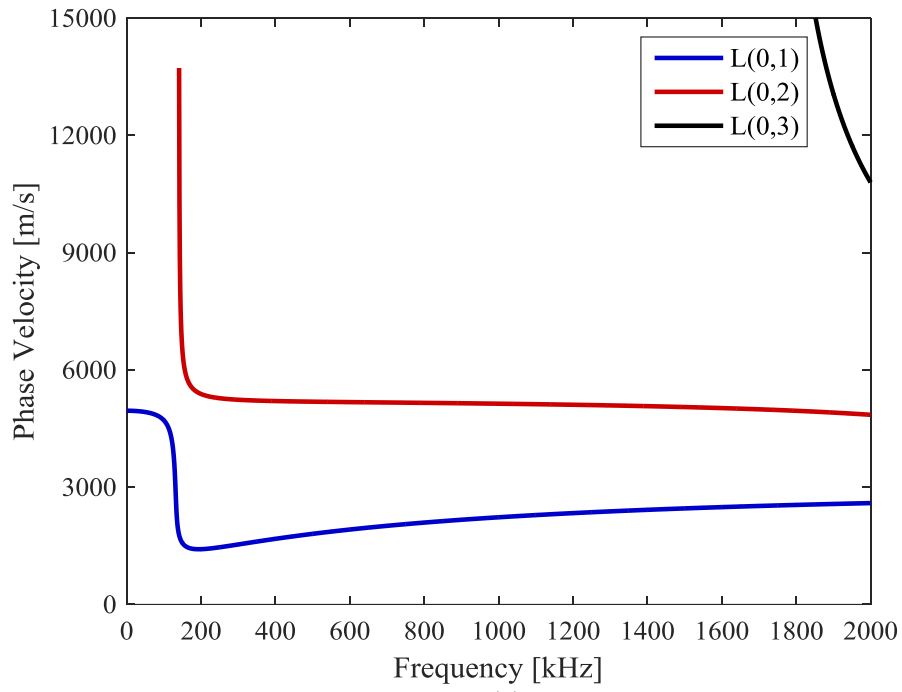
Theoretically, guided waves in pipes include infinite number of modes considering the explicit circumferential order n and the implicit family order m. According to the circumferential order, they are categorized as axisymmetric waves for n equal to zero and non-axisymmetric waves for n greater than zero. Taking into account the displacement component, axisymmetric waves include longitudinal waves L(0,m) with two displacement components u_r and u_z ($u_\theta = 0$), and torsional waves T(0,m) with the angular displacement u_θ ($u_r = u_z = 0$). When n is greater than zero, the modes are called flexural modes F(n,m) with all three displacement components u_r , u_θ , and u_z .

Dispersion curves for a 304 stainless steel pipe (12.7 mm outer diameter and 10.9 mm inner diameter) are shown as an example. The phase velocity and group velocity dispersion curves for axisymmetric longitudinal waves are displayed in Figure 3.6. In the frequency range from 0 to 2 MHz there are three modes L(0,1), L(0,2) and L(0,3). Phase velocity of a wave is the rate at which the phase of the wave propagates in space. It is important in terms of mode excitation. Group velocity is the propagation speed of the energy transport or of the wave group package. The curves are dispersive showing phase velocity as a function of frequency. Dispersion curves for axisymmetric torsional waves are shown in Figure 3.7. T(0,1) torsional mode is non-dispersive indicating a wave package with consistent length as it travels along the structure.

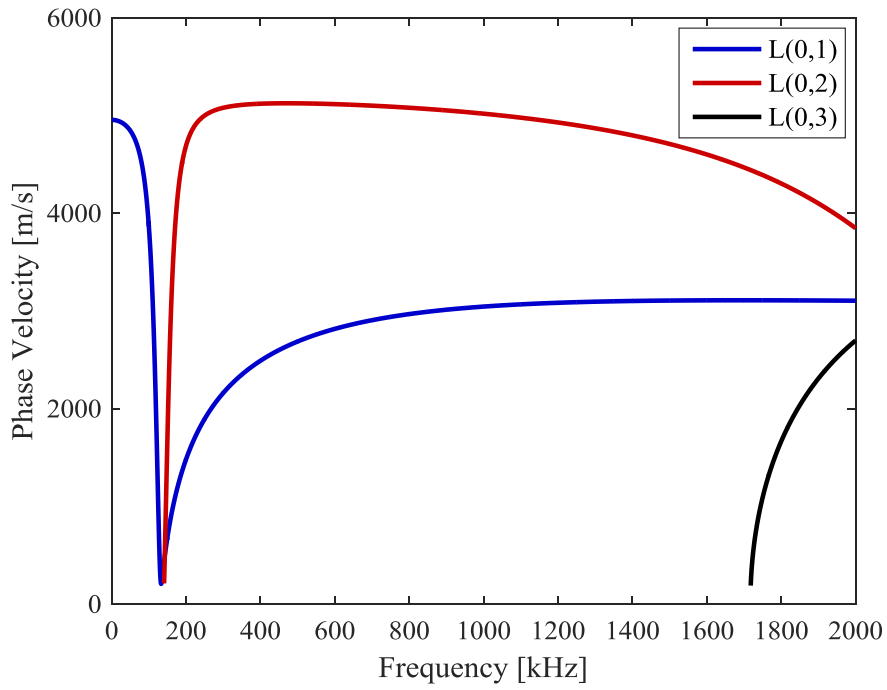
3.5 WAVELET-BASED FAILED FUEL ROD CONDITION DETECTION

APPROACH

To fill the gap toward implementing the guided wave-based SHM on failed fuel rod, a wavelet-based approach is developed to monitor the structure change (rod defect and ice formation) at the failed rod. Guided waves are transmitted from one side of the failed fuel rod. Once the guided waves are received on the other side, they are processed with the CWT, where different frequency components at any particular time instance can be visualized and identified. Different from traditional signal-frequency guided wave propagation method [115], multi-frequency guided waves are used in this research. The advantage of this method is that it is able to extract complex information simultaneously. With the wavelet transform, guided waves can be displayed in both time and frequency domains.



(a)



(b)

Figure 3.6 (a) Phase velocity and (b) group velocity dispersion curves of axisymmetric longitudinal waves ($L(0,m)$) in a 304 stainless steel pipe (12.7 mm outer diameter and 10.9 inner diameter), where m is the mode family order.

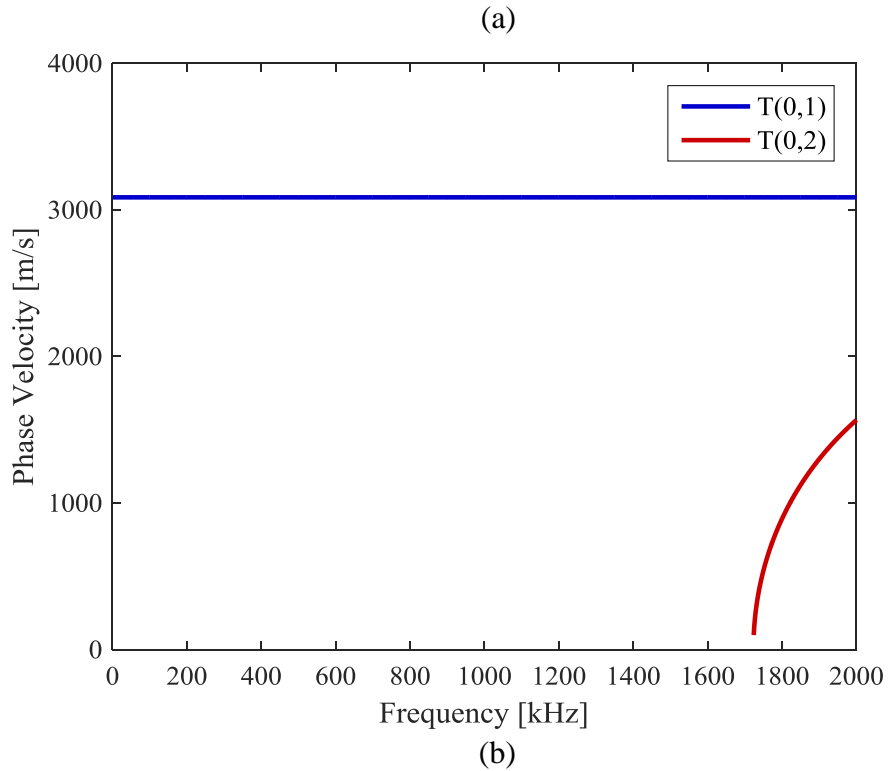
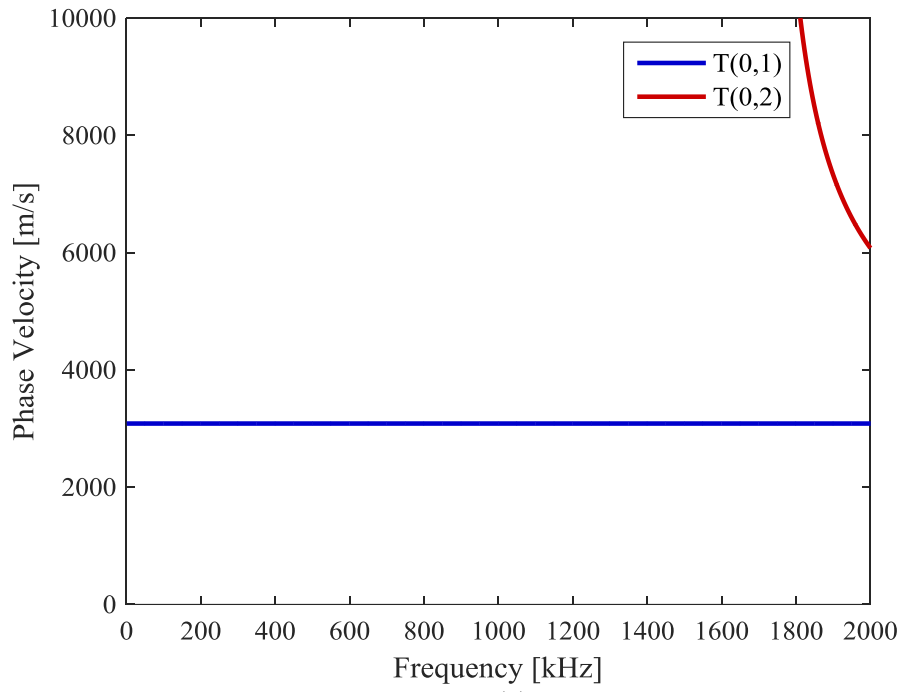


Figure 3.7 (a) Phase velocity and (b) group velocity dispersion curves of axisymmetric torsional waves ($T(0,m)$) in a 304 stainless steel pipe (12.7 mm outer diameter and 10.9 mm inner diameter), where m is the mode family order.

According to Figure 3.6-7, for axisymmetric waves below 140 kHz, only L(0,1) and T(0,1) exist. In this work, L(0,1) waves with 50 kHz and 100 kHz frequencies are used. Simulations and experiments are conducted to investigate the relationship between different conditions (defect location and size, and ice formation and ice level) and CWT coefficients. Then the wavelet-based approach is developed based on this.

3.5.1 MULTI-FREQUENCY GUIDED WAVE EXCITATION

The excited single-frequency guided waves can provide some information of structural features. However, if multiple features are desired to acquire synchronously from the single received wave, the multi-frequency guided waves are needed to provide further information. A simple time or frequency domain analysis cannot satisfy this situation. Using a Morlet wavelet, wavelet analysis can transform a time domain signal (which includes two or more frequencies) into both time and frequency domains to display frequency components at each time instance. Wavelet analysis provides sufficient information about the received wave at different frequencies. By calculating the difference between two locations of the maximum modulus (Equation 2.7) in transmitted and received signals, the propagation time for guided waves at different frequencies can be obtained [168]. Figure 3.8 shows the CWT result for a double-frequency guided wave propagating on a sample rod, which is transmitted from one side and received from the other side. Via the CWT, the two frequencies included in the guide wave are successfully differentiated.

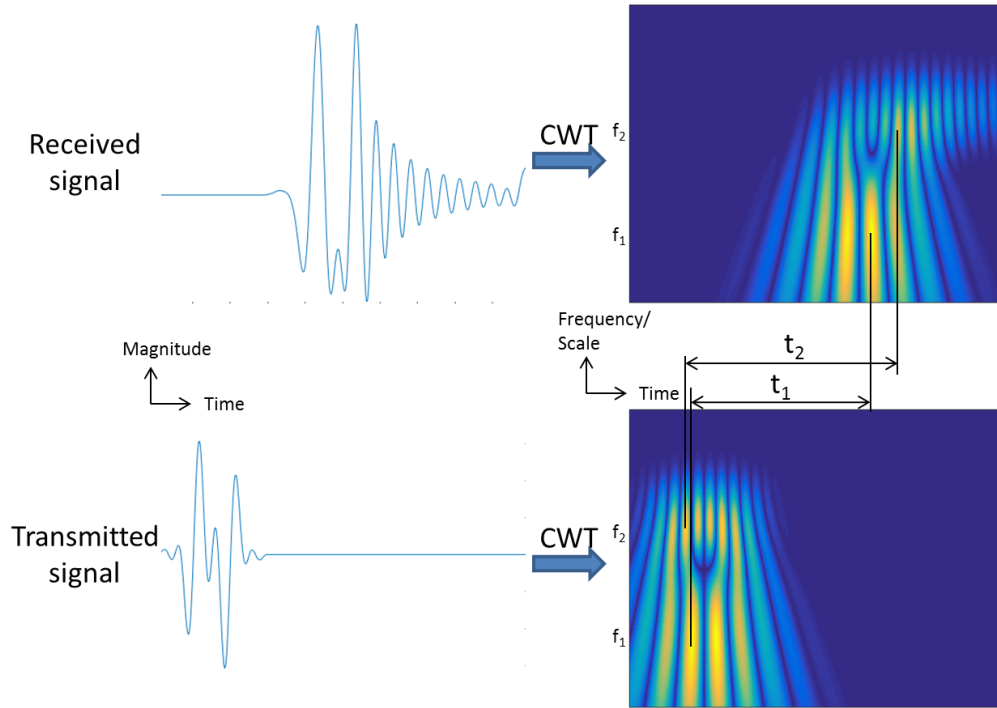


Figure 3.8 The CWT results of transmitted and received signals. t_1 and t_2 show different propagation time for f_1 and f_2 guided waves ($L(0,1)$ mode).

3.5.2 DETECTION OF DEFECT LOCATION AND SIZE

In this section, the influence of defect location and size to the received signals is investigated. Pitch-catch measurement is used (guided wave is excited on one side of the rod and received on the other side). The received guided waves are analyzed by the CWT based on different defects.

FEM software ANSYS/Multiphysics 15.0 is used to investigate the influence of different defect locations along circumferential direction and various defect sizes to the received signals, the. The model rod built in the simulations is a 304 stainless steel pipe with 300 mm length, 12.7 mm outer diameter and 10.9 mm inner diameter, Young's modulus 196.5 GPa, Poisson's ratio 0.29, and density 8000kg/m^3 . The defect is at the

middle of the rod (150 mm away from each side). Figure 3.9 shows the finite element model of the failed fuel rod with defect. The SOLID45 elements are used to build the rod. Guided waves including 50 kHz and 100 kHz frequencies are excited from one side of the rod, and only longitudinal direction displacement is considered.

Transient analysis is used in the simulations. The calculation accuracy is ensured by limiting the maximum dimensions of elements to less than ten elements per wavelength along the wave propagation direction and limiting the integration time step for transient analysis stability [161]. In this work, the maximum size of elements is smaller than 1 mm, and the time step is 0.1 μ s.

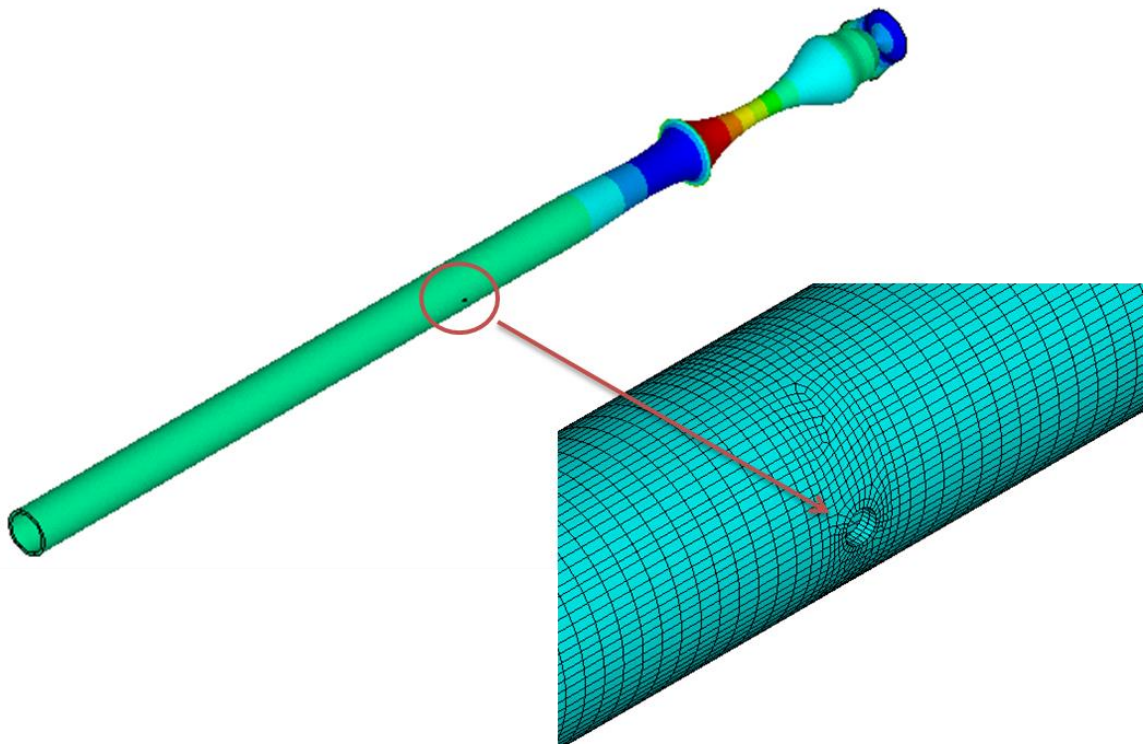


Figure 3.9 The finite element model of the failed fuel rod with defect, and guided wave propagation simulation.

The received guided waves are processed by the CWT and the maximum modulus results are compared. The angle between receiver sensor and defect along circumferential direction is defined in Figure 3.10. Figure 3.11 shows the results for 1 mm diameter defect whose angles are from 0 ° to 180 °. The results indicate that the maximum modulus for both 50 kHz and 100 kHz signals is varying as the angle is increasing. Figure 3.12 shows simulation results of the maximum modulus in CWT for different sizes of defects at 0 °, 90 ° and 180 ° angles. Again, the change in size of defect influences the maximum modulus at different angles. The relationship can be built based on this connection between different defect conditions and the maximum modulus at 50 kHz and 100 kHz.

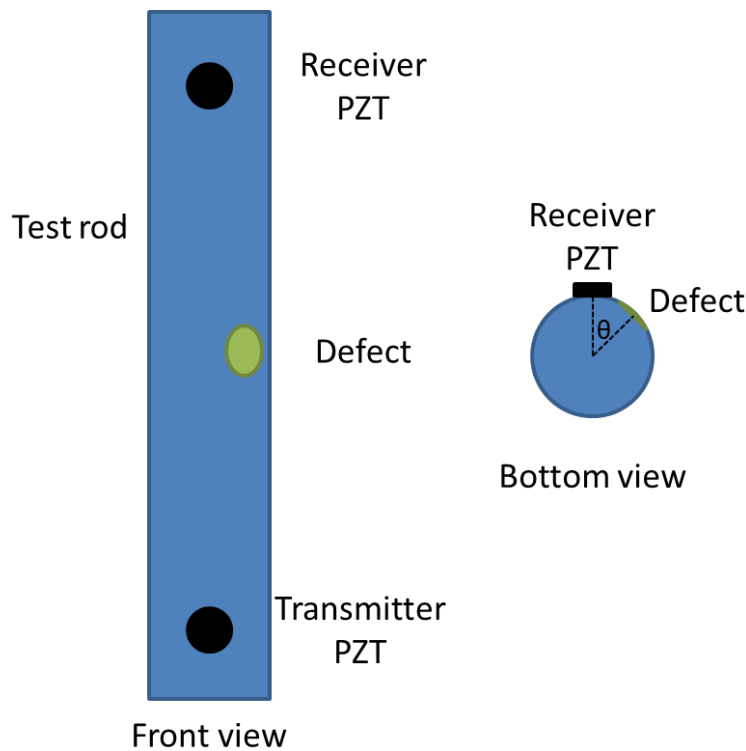


Figure 3.10 The definition of angle θ between defect and receiver sensor along circumferential direction.

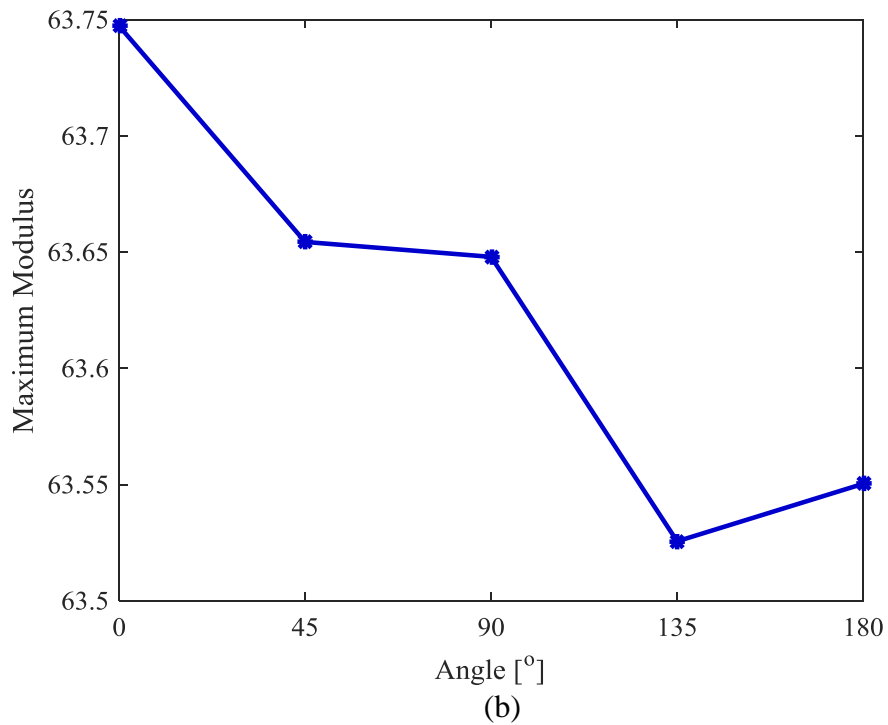
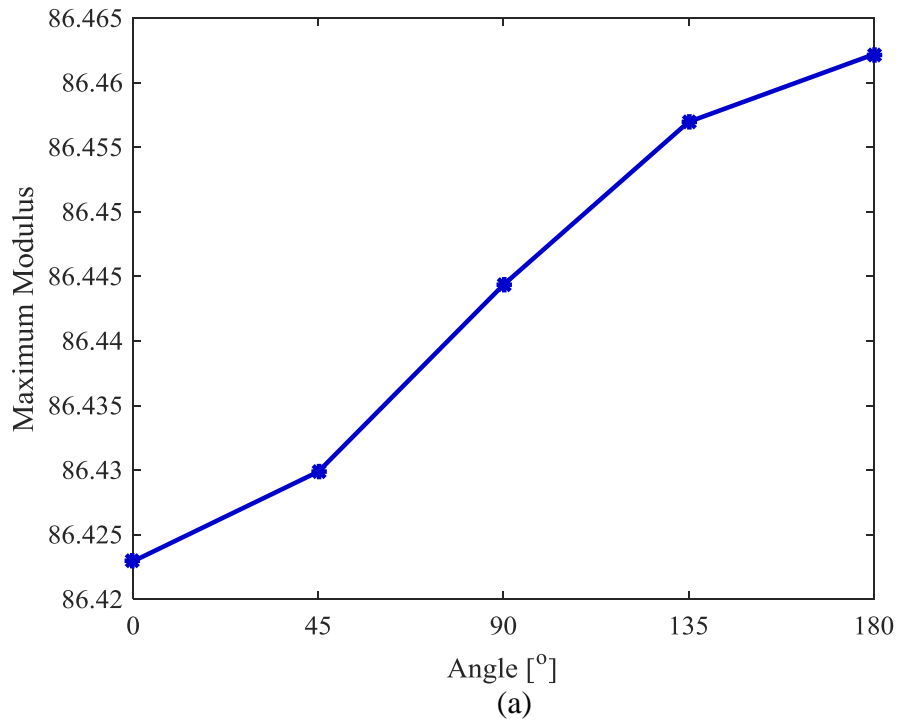
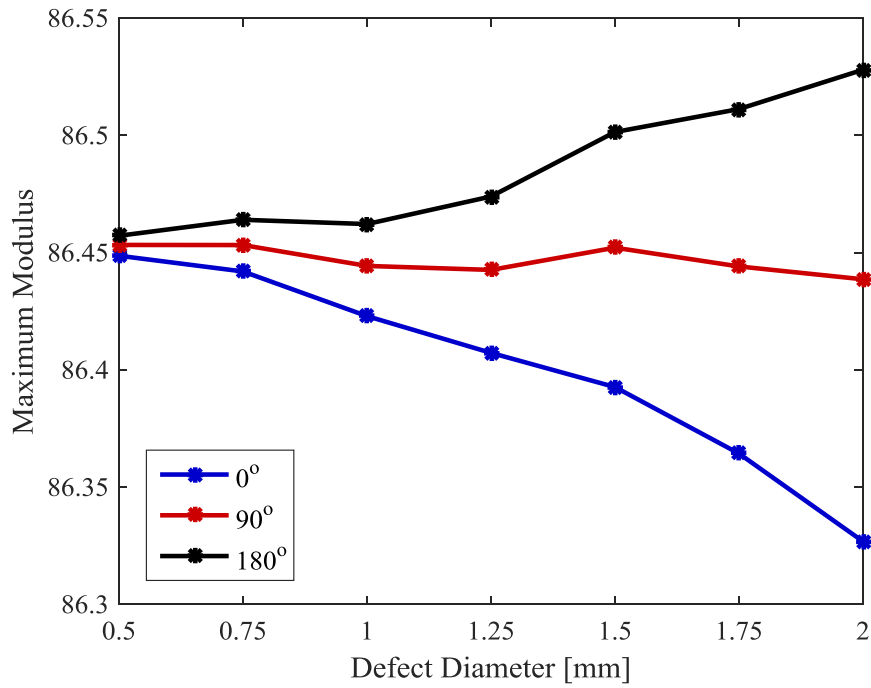
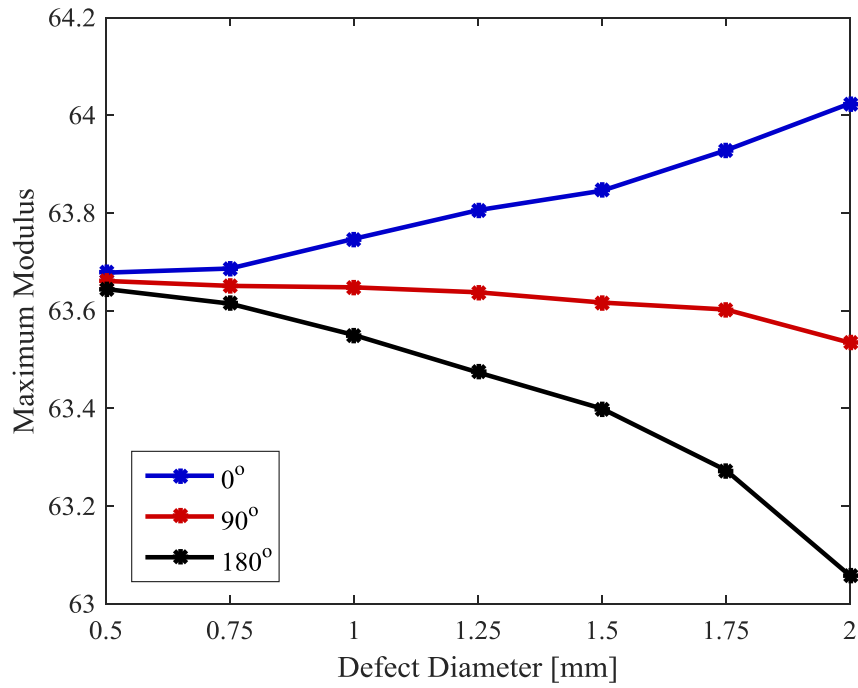


Figure 3.11 Simulation results of the maximum modulus in CWT at (a) 50 kHz and (b) 100 kHz frequencies for different angles between received sensor and defect (1 mm) along circumferential direction.



(a)



(b)

Figure 3.12 Simulation results of the maximum modulus in CWT at (a) 50 kHz and (b) 100 kHz frequencies for different sizes of defects at 0°, 90° and 180° angles between received sensor and defect along circumferential direction.

3.5.3 DETECTION OF ICE FORMATION AND ICE LEVEL

Ice formation will cause a different structural response from the fuel rod that can be measured. Local parameter changes caused by ice can be discovered by guided waves introduced into the rod structure. The guided waves have different propagating speeds on an empty rod over frequencies based on the dispersion curves. When there is ice inside the rod, the propagation speeds will be attenuated. Since the traveling speeds on an empty rod and a rod with ice inside are different, the ice level can be calculated based on the guided wave arrival time. PZTs are used to excite and receive longitudinal guided wave L(0,1) using pitch-catch measurement for ice formation and ice level detection (Figure 3.13). The wave propagation path d from the transmitter to the receiver consists of ice path d_i and empty rod path $d-d_i$. Therefore, the total propagation time t can be expressed as

$$t = \frac{d_i}{v_i} + \frac{d-d_i}{v} \quad (3.14)$$

where v and v_i are guided wave propagation speeds in the empty rod and the rod with ice. Ice forming inside the rod from water can be detected using Equation 3.14. The comprehensive approach to determine ice formation is designed as following.

A guide wave is transmitted that includes two frequencies (f_1 and f_2). The received signal is analyzed using the CWT to extract the total propagation time of waves at each frequency (t_1 and t_2). Based on Equation 3.14, the following equations are obtained according to guided waves with different frequencies traveling on the rod:

$$\begin{cases} \frac{d-d_i}{v_1} + \frac{d_i}{v_{1i}} = t_1 \\ \frac{d-d_i}{v_2} + \frac{d_i}{v_{2i}} = t_2 \end{cases} \Rightarrow \begin{cases} d_i = \frac{v_{1i}}{v_{1i}-v_1} (d - v_1 t_1) \\ d_i = \frac{v_{2i}}{v_{2i}-v_2} (d - v_2 t_2) \end{cases} \quad (3.15)$$

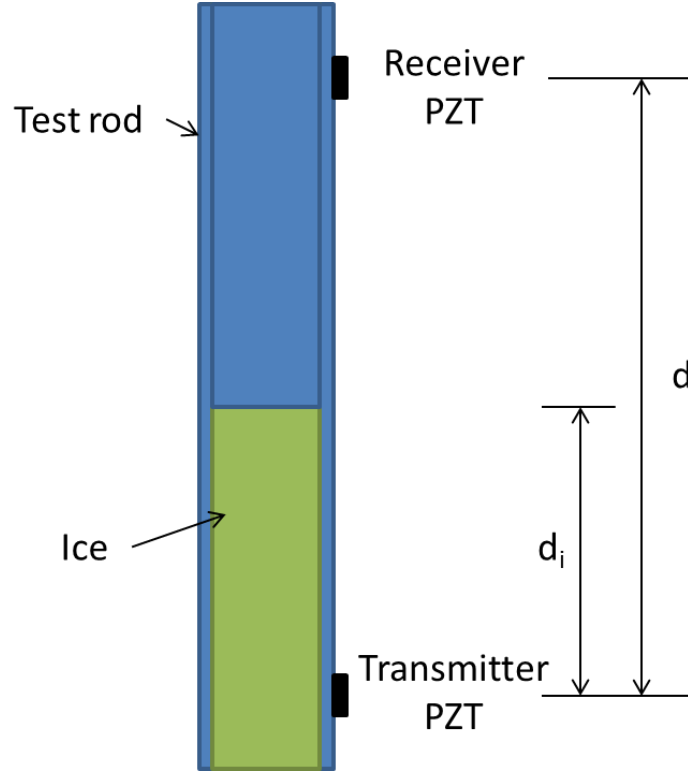


Figure 3.13 Pitch-catch measurement for ice formation and ice level detection.

where d is the distance between transmitter and receiver, d_i is the height of ice, v_1 and v_2 are guided wave propagating speeds through empty rod at f_1 and f_2 , and v_{1i} and v_{2i} are guided wave propagating speeds through the rod with ice inside from the f_1 and f_2 signals. If the calculated results of d_i match each other, it means there is ice inside the rod and it indicates the ice level. Otherwise, it shows there is still water inside the rod.

The PZT uses piezoelectric effect on materials that can convert an applied mechanical force to the internal generation of electrical charge and vice versa. Linear piezoelectricity can be described in coupled equations, of which the strain-charge form is [169]:

$$\begin{aligned} S_{ij} &= s_{ijkl}T_{kl} + d_{kij}E_k \\ D_i &= d_{ijk}T_{jk} + \varepsilon_{ij}E_j \end{aligned} \quad (3.16)$$

where S is strain, s is compliance under short-circuit conditions, T is stress, d represents the direct piezoelectric effect, E is electric field strength, D is electric displacement, and ε is permittivity (free-body dielectric constant).

One advantage of PZT is their capability of tuning its output to excite various guided wave modes. The tuning effect of PZT benefits the selective actuation and sensing of guided wave modes [170, 171]. In the experiments, the transmitter and receiver PZTs are the same round PZT (7 mm diameter, 0.2 mm thickness) bonded on a 304 stainless steel pipe (12.7 mm outer diameter and 10.9 inner diameter). Their distance is 300 mm. The amplitude of voltage given to the transmitter PZT is 35 V. Figure 3.14 shows experimental tuning curve of the receiver PZT.

Experiments are conducted by building a PZT sensing system (Figure 3.15). Guided waves are generated from a PZT. The excitation signal has 20 V amplitude and 50 kHz and 100 kHz frequencies. The guided waves 300 mm away from the PZT are measured by another PZT. First, for both two frequencies, the propagation speeds on empty rod and rod with ice are measured, respectively. In this way, v_1 , v_2 , v_{1i} and v_{2i} in Equation 3.15 are known. The experimental results are $v_1 = 4834$ m/s, $v_2 = 3901$ m/s, $v_{1i} = 3902$ m/s, and $v_{2i} = 3327$ m/s. Then, the guided waves are measured at various ice levels from 0 to 300 mm, and converted to calculated ice level using Equation 3.15 (Figure 3.16). The results indicate that this approach can accurately identify the ice formation as well as the ice level.

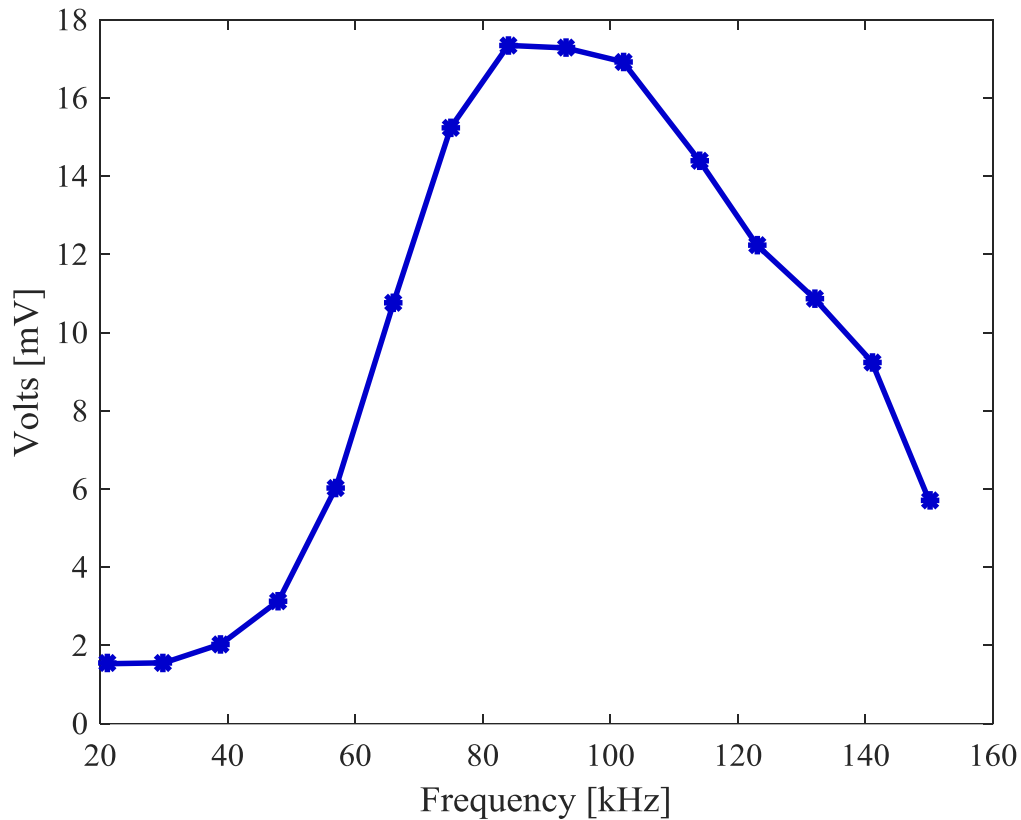


Figure 3.14 Tuning curve of a round PZT (7 mm diameter, 0.2 mm thickness) bonded on a 304 stainless steel pipe (12.7 mm outer diameter and 10.9 inner diameter).

3.5.4 ADVANCED WAVELET-BASED APPROACH

Combining the methods used in Sections 3.5.2-3, a novel wavelet-based structural health monitoring approach is established.

In Section 3.5.2, it is shown that there is a relationship between defects and CWT coefficients of received signal. For any specific problem (for example, failed fuel rods), first use pitch-catch measurement and wavelet analysis to build this relationship from known conditions. Then for any unknown but same condition, the defect can be detected and predicted by only analyzing the received signals.

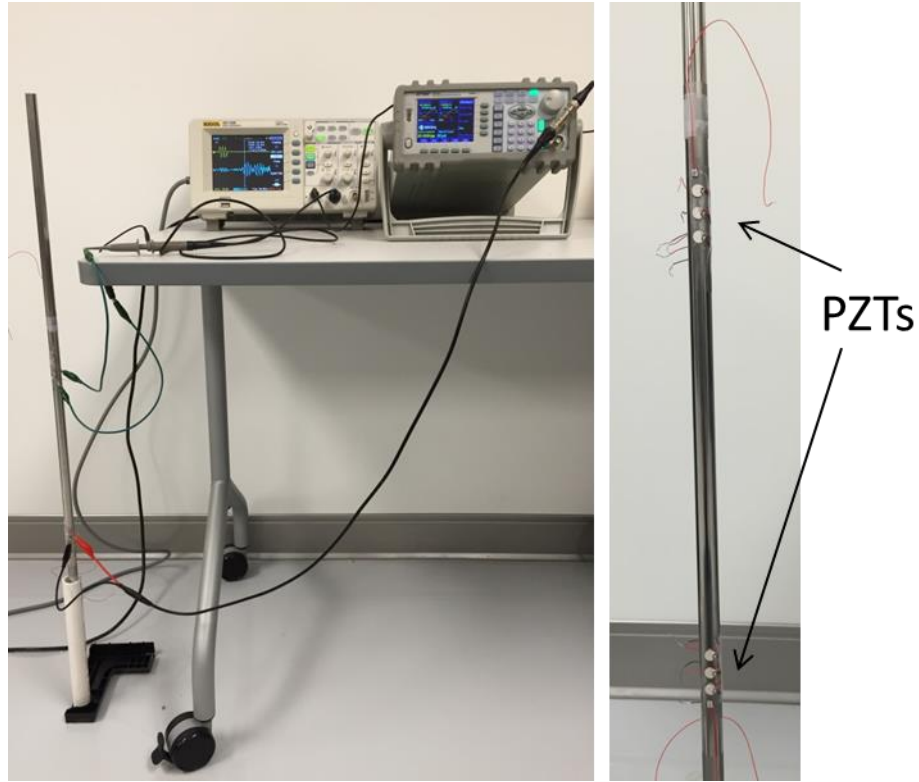


Figure 3.15 Experiment setup for PZT sensing system.

For detecting the ice formation and ice level inside the rod, first measure the propagation speeds on the specific rod and the rod with ice inside. After that, any ice formation and the related ice level can be identified using Equation 3.15.

Figure 3.17 displays the sequence of the wavelet-based approach.

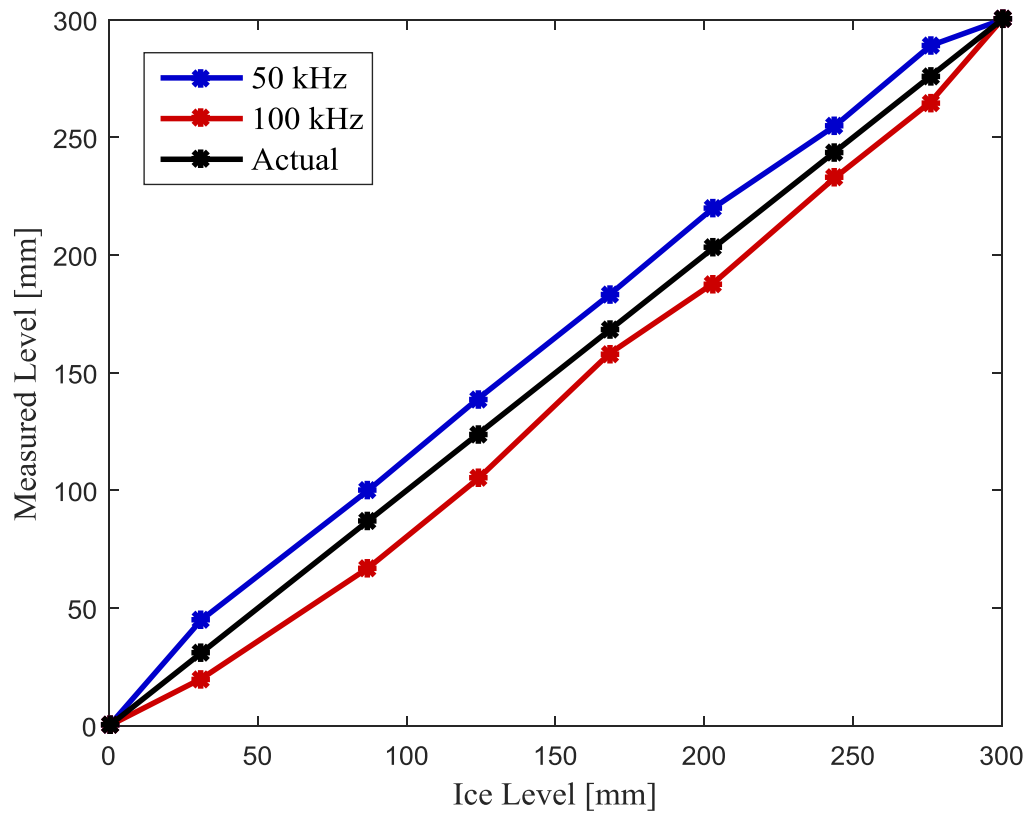


Figure 3.16 Experimental results for the measured ice levels by 50 kHz and 100 kHz guided waves.

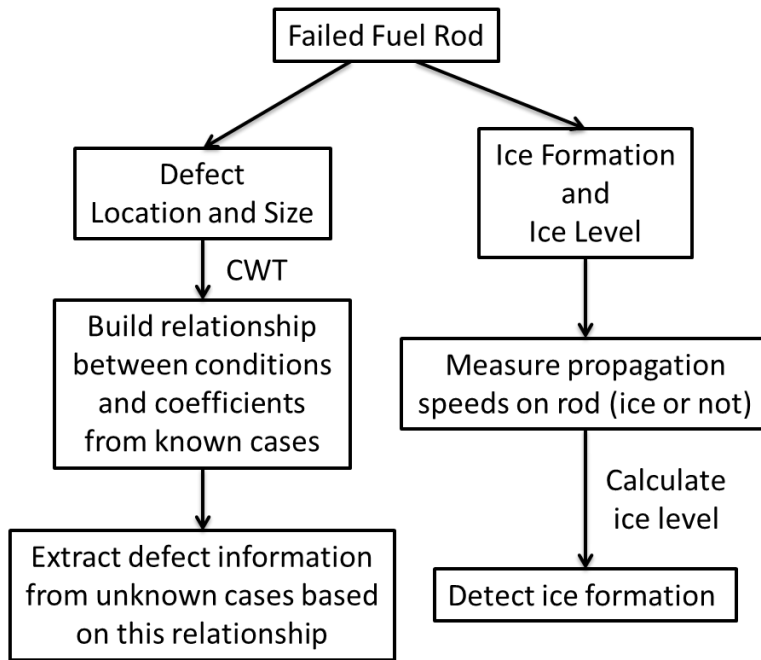


Figure 3.17 The wavelet-based approach for structural health monitoring in dry cask storage.

CHAPTER 4

CONCLUSIONS AND FUTURE WORK

This chapter includes an overall conclusion to this work, from Chapter 1 to 3, and outlines directions for future research.

4.1 CONCLUSIONS

This dissertation introduces a novel wavelet-based periodic error measurement and compensation method that can be used to compensate periodic errors for both constant and non-constant velocity profiles in real-time. It also describes a novel wavelet-based approach for structural health monitoring in dry cask storage.

Chapter 1 introduces wavelet analysis, including DWT and CWT. For CWT, related equations, typical wavelets that could be used, and the linearity property are given. The complex Morlet wavelet is described in detail since it is used in the research. The complex Morlet wavelet is suitable in periodic error compensation algorithm because it enables localization in both the time and frequency domains. The frequency of the periodic error signal is located at the scale with the maximum wavelet coefficient and the phase information can be extracted based on the real and imaginary parts of this coefficient. It is also used in detecting the conditions of the failed fuel rod since it can identify the propagation time of guided waves at different frequencies.

Chapter 2 provides background of interferometry. Heterodyne interferometer is introduced. Error sources in heterodyne interferometry are analyzed, and the focus is on periodic error. The traditional frequency domain compensation approach for periodic error and its limitation are also given. Then it describes the entire algorithm design process. The implementation of the algorithm consists of detrending the signal, applying the wavelet transform, identifying the ridge, phase and amplitude, and finally reconstructing and compensating periodic error. It shows the simulation and experimental results using the wavelet-based algorithm for constant and non-constant velocity motions. It also discusses the situations where the periodic error amplitude is varying, and higher order periodic errors. The algorithm is also implemented on the hardware (FPGA).

Chapter 3 describes the background of spent nuclear fuel rod drying. SHM is first introduced into this field. Guided waves in pipes are shown. Dispersion curves are given for the sample rod. After that, the novel wavelet-based detection approach for failed fuel rod conditions is described. In order to extract complex information, multi-frequency guided waves are excited, which is different from traditional single-frequency guided wave propagation. The relationship between location and size of defects and CWT coefficients of received signals is investigated. Also, the method to identify ice formation and ice level inside the fuel rod is discussed. Finally, the approach is synthesized and shown its potential to apply to other applications.

4.2 FUTURE WORK

The algorithm presented in this work is designed to be executed on parallel hardware offering the potential application for real-time compensation of periodic error

in heterodyne interferometers. In the future, the algorithm will be implemented in the experiments to determine the limits for the industrial implementation of wavelet analysis for periodic error measurement and compensation. Using the experimental setup, the performance of the wavelet-based algorithm to accurately characterize and compensate the periodic error will be investigated.

Also, experiments will be conducted in the drying cask storage. Different defects will be detected based on the established relationship between defects and CWT coefficients. The approach will be applied to monitor any ice formation during different drying tasks in the storage.

REFERENCES

- [1] Daubechies I. Orthonormal bases of compactly supported wavelets. Communications on pure and applied mathematics 1988;41(7):909-96.
- [2] Daubechies I. Ten lectures on wavelets: SIAM; 1992.
- [3] Combes J, Grossmann A, Tchamitchian P, Pierce AD. Wavelets: Time-frequency methods and phase space. The Journal of the Acoustical Society of America 1991;89(5):2477-8.
- [4] Rioul O, Vetterli M. Wavelets and signal processing. IEEE signal processing magazine 1991;8(LCAV-ARTICLE-1991-005):14-38.
- [5] Meyer Y. Wavelets and applications: Paris [etc.]: Masson; Berlin [etc.]: Springer-Verlag; 1992.
- [6] Ruskai MB, Beylkin G, Coifman R. Wavelets and their Applications. Jones and Bartlett Books in Mathematics, Boston: Jones and Bartlett, 1992, edited by Ruskai, Mary B; Beylkin, Gregory; Coifman, Ronald 1992;1.
- [7] Donoho DL. Unconditional bases are optimal bases for data compression and for statistical estimation. Applied and computational harmonic analysis 1993;1(1):100-15.
- [8] Burke B. The mathematical Microscope: waves, wavelets and beyond. A Positron Named Priscilla, Scientific Discovery at the Frontier 1994:196-235.
- [9] Hubbard BB. The World According the Wavelet: The Story of a Mathematical Technique in the Making. Ak Peters 1996:227-9.
- [10] Donoho DL. Nonlinear wavelet methods for recovery of signals, densities, and spectra from indirect and noisy data. In: Proceedings of symposia in Applied Mathematics. 1993. p. 173-205.
- [11] Donoho DL. De-noising by soft-thresholding. Information Theory, IEEE Transactions on 1995;41(3):613-27.
- [12] Saito N. Simultaneous noise suppression and signal compression using a library of orthonormal bases and the minimum-description-length criterion. In: SPIE's International Symposium on Optical Engineering and Photonics in Aerospace Sensing. 1994. p. 224-35.

- [13] Wei D, Tian J, Wells Jr RO, Burrus CS. A new class of biorthogonal wavelet systems for image transform coding. *Image Processing, IEEE Transactions on* 1998;7(7):1000-13.
- [14] Guo H. Wavelets for approximate Fourier Transform and data compression: PhD thesis, Rice University; 1997.
- [15] Daubechies I. The wavelet transform, time-frequency localization and signal analysis. *IEEE Transactions on Information Theory* 1990;36(5):961-1005.
- [16] Farge M. Wavelet transforms and their applications to turbulence. *Annual Review of Fluid Mechanics* 1992;24(1):395-458.
- [17] Haar A. Zur theorie der orthogonalen funktionensysteme. *Mathematische Annalen* 1910;69(3):331-71.
- [18] Szu H, Hsu C, Sa LD, Li W. Hermitian Hat wavelet design for singularity detection in the PARAGUAY river level data analysis. *Proceeding of SPIE The International Society for Optical Engineering* 1997;3078:96-115.
- [19] Ormsby RRH, Klauder B. A choice of wavelets. *CSEG Recorder* 1994;19:8-9.
- [20] Taner M. Joint Time/Frequency Analysis, Q Quality Factor and Dispersion Computation Using Gabor-Morlet Wavelets or the Gabor-Morlet Transform. RSI Technical Report. 2001.
- [21] Patterson S, Beckwith J. Reduction of systematic errors in heterodyne interferometric displacement measurement. In: *Proceedings of the 8th International Precision Engineering Seminar (IPES)*. 1995. p. 101-4.
- [22] Badami V, Patterson S. A frequency domain method for the measurement of nonlinearity in heterodyne interferometry. *Precision engineering* 2000;24(1):41-9.
- [23] Badami V, Patterson S. Investigation of nonlinearity in high-accuracy heterodyne laser interferometry. In: *Proceedings of the 12th annual American Society for Precision Engineering (ASPE) conference*. 1997. p. 153-6.
- [24] Schmitz T, Chu DC, Kim HS. First and second order periodic error measurement for non-constant velocity motions. *Precision engineering* 2009;33(4):353-61.
- [25] Schmitz T, Adhia C, Kim HS. Periodic error quantification for non-constant velocity motion. *Precision engineering* 2012;36(1):153-7.
- [26] Peggs G, Yacoot A. A review of recent work in sub-nanometre displacement measurement using optical and X-ray interferometry. *Philosophical Transactions of the Royal Society of London A: Mathematical, Physical and Engineering Sciences* 2002;360(1794):953-68.

- [27] Bobroff N. Residual errors in laser interferometry from air turbulence and nonlinearity. *Applied optics* 1987;26(13):2676-82.
- [28] Bobroff N. Recent advances in displacement measuring interferometry. *Measurement Science and Technology* 1993;4(9):907.
- [29] Estler W. High-accuracy displacement interferometry refraction in air. *Applied optics* 1985;24(6):808-15.
- [30] Schmitz T, Evans C, Davies A, Estler WT. Displacement uncertainty in interferometric radius measurements. *CIRP Annals-Manufacturing Technology* 2002;51(1):451-4.
- [31] Schmitz T, Kim HS. Monte Carlo evaluation of periodic error uncertainty. *Precision engineering* 2007;31(3):251-9.
- [32] Kim H, Schmitz T, Beckwith J. Periodic error in heterodyne interferometry: Examination and Elimination. In: Halsey D, Raynor W, ed, editors. *Handbook of Interferometers: Research, Technology and Applications*. Hauppauge, NY: Nova Science; 2009.
- [33] Schmitz TL, Houck L, Chu D, Kalem L. Bench-top setup for validation of real time, digital periodic error correction. *Precision engineering* 2006;30(3):306-13.
- [34] Fedotova G. Analysis of the measurement error of the parameters of mechanical vibrations. *Measurement Techniques* 1980;23(7):577-80.
- [35] Quenelle R. Nonlinearity in interferometric measurements. *Hewlett-Packard Journal* 1983;34(4):10.
- [36] Sutton C. Nonlinearity in length measurements using heterodyne laser Michelson interferometry. *Journal of Physics E: Scientific Instrumentation* 1987;20:1290-2.
- [37] Steinmetz C. Sub-micron position measurement and control on precision machine tools with laser interferometry. *Precision engineering* 1990;12(1):12-24.
- [38] Oldham N, Kramar J, Hetrick P, Teague E. Electronic limitations in phase meters for heterodyne interferometry. *Precision engineering* 1993;15(3):173-9.
- [39] Demarest FC. High-resolution, high-speed, low data age uncertainty, heterodyne displacement measuring interferometer electronics. *Measurement Science and Technology* 1998;9(7):1024.
- [40] Edlén B. The refractive index of air. *Metrologia* 1966;2(2):71.
- [41] Popela B. The Influence of the Atmosphere on the Wavelength of the He-Ne Laser and the Solution of Corrections of the Laser Interferometer. *Journal of modern optics* 1972;19(7):605-12.

- [42] Jones FE. Simplified equation for calculating the refractivity of air. *Applied optics* 1980;19(24):4129-30.
- [43] Jones FE. The refractivity of air. *Journal of Research* 1981;86:27-32.
- [44] Schellekens P, Wilkening G, Reinboth F, Downs M, Birch K, Spronck J. Measurements of the refractive index of air using interference refractometers. *Metrologia* 1986;22(4):279.
- [45] Birch K, Reinboth F, Ward R, Wilkening G. The effect of variations in the refractive index of industrial air upon the uncertainty of precision length measurement. *Metrologia* 1993;30(1):7.
- [46] Číp O, Petrů F, Matoušek V, Lazar J. Direct measurement of index of refraction of air by means of high-resolution laser interferometry. *Physica Scripta* 2005;2005(T118):48.
- [47] Cosijns S, Haitjema H, Schellekens P. Modeling and verifying non-linearities in heterodyne displacement interferometry. *Precision engineering* 2002;26(4):448-55.
- [48] Schmitz T, Beckwith J. An investigation of two unexplored periodic error sources in differential-path interferometry. *Precision engineering* 2003;27(3):311-22.
- [49] Rosenbluth A, Bobroff N. Optical sources of non-linearity in heterodyne interferometers. *Precision engineering* 1990;12(1):7-11.
- [50] Augustyn W, Davis P. An analysis of polarization mixing errors in distance measuring interferometers. *Journal of Vacuum Science & Technology B* 1990;8(6):2032-6.
- [51] Xie Y, Wu Y-z. Zeeman laser interferometer errors for high-precision measurements. *Applied optics* 1992;31(7):881-4.
- [52] De Freitas J, Player M. Importance of rotational beam alignment in the generation of second harmonic errors in laser heterodyne interferometry. *Measurement Science and Technology* 1993;4(10):1173.
- [53] Hou W, Zhao X. Drift of nonlinearity in the heterodyne interferometer. *Precision engineering* 1994;16(1):25-35.
- [54] De Freitas J, Player M. Polarization effects in heterodyne interferometry. *Journal of modern optics* 1995;42(9):1875-99.
- [55] Howard L, Stone J. Computer modeling of heterodyne interferometer errors. *Precision engineering* 1995;12(1):143-6.
- [56] Wu C-m, Su C-s. Nonlinearity in measurements of length by optical interferometry. *Measurement Science and Technology* 1996;7(1):62.

- [57] Park B, Eom T, Chung M. Polarization properties of cube-corner retroreflectors and their effects on signal strength and nonlinearity in heterodyne interferometers. *Applied optics* 1996;35(22):4372-80.
- [58] De Freitas JM. Analysis of laser source birefringence and dichroism on nonlinearity in heterodyne interferometry. *Measurement Science and Technology* 1997;8(11):1356.
- [59] Li B, Liang J-w. Effects of polarization mixing on the dual-wavelength heterodyne interferometer. *Applied optics* 1997;36(16):3668-72.
- [60] Wu C-M, Deslattes RD. Analytical modeling of the periodic nonlinearity in heterodyne interferometry. *Applied optics* 1998;37(28):6696-700.
- [61] Petrů F, Číp O. Problems regarding linearity of data of a laser interferometer with a single-frequency laser. *Precision engineering* 1999;23(1):39-50.
- [62] Dubovitsky S, Lay OP, Seidel DJ. Elimination of heterodyne interferometer nonlinearity by carrier phase modulation. *Optics letters* 2002;27(8):619-21.
- [63] Zhao H, Zhang G. Nonlinear error by orientation and elliptic polarization in a two-beam interferometer. *Optical Engineering* 2002;41(12):3204-8.
- [64] Hou W. *Subdivision of Nonlinearity in Heterodyne Interferometers*. Fringe 2005: Springer; 2006. p. 327-33.
- [65] Hou W. Optical parts and the nonlinearity in heterodyne interferometers. *Precision engineering* 2006;30(3):337-46.
- [66] Stone JA, Howard LP. A simple technique for observing periodic nonlinearities in Michelson interferometers. *Precision engineering* 1998;22(4):220-32.
- [67] Yin C, Dai G, Chao Z, Xu Y, Xu J. Determining the residual nonlinearity of a high-precision heterodyne interferometer. *Optical Engineering* 1999;38(8):1361-5.
- [68] Loner D, Knarren B, Cosijns S, Haitjema H, Schallakans P. Laser polarization state measurement in heterodyne interferometry. *CIRP Annals-Manufacturing Technology* 2003;52(1):439-42.
- [69] Knarren BA, Cosijns SJ, Haitjema H, Schellekens PH. Fiber characterization for application in heterodyne laser interferometry with nanometer uncertainty, part I: polarization state measurements. *Optical Engineering* 2005;44(2):025002--9.
- [70] Knarren BA, Cosijns SJ, Haitjema H, Schellekens PH. Fiber characterization for application in heterodyne laser interferometry, part II: modeling and analysis. *Optical Engineering* 2005;44(2):025003--9.

- [71] Topcu S, Chassagne L, Alayli Y, Juncar P. Improving the accuracy of homodyne Michelson interferometers using polarisation state measurement techniques. *Optics communications* 2005;247(1):133-9.
- [72] Kim HS, Schmitz TL. Periodic error calculation from spectrum analyzer data. *Precision engineering* 2010;34(2):218-30.
- [73] Ganguly V, Kim NH, Kim HS, Schmitz T. Sensitivity analysis of periodic errors in heterodyne interferometry. *Measurement Science and Technology* 2011;22(3):035305.
- [74] Eom T, Kim J, Jeong K. The dynamic compensation of nonlinearity in a homodyne laser interferometer. *Measurement Science and Technology* 2001;12(10):1734.
- [75] Tanaka M, Yamagami T, Nakayama K. Linear interpolation of periodic error in a heterodyne laser interferometer at subnanometer levels [dimension measurement]. *Ieee Transactions on Instrumentation and Measurement* 1989;38(2):552-4.
- [76] Hou W, Wilkening G. Investigation and compensation of the non-linearity of heterodyne interferometers. *Precision engineering* 1992;14(2):91-8.
- [77] Wu C-m, Su C-s, Peng G-S. Correction of nonlinearity in one-frequency optical interferometry. *Measurement Science and Technology* 1996;7(4):520.
- [78] Wu C-m, Lawall J, Deslattes RD. Heterodyne interferometer with subatomic periodic nonlinearity. *Applied optics* 1999;38(19):4089-94.
- [79] Nakatani N. Heterodyne interferometers using orthogonally polarized and two-frequency shifted light sources with super-high extinction ratio. *Optical Review* 1999;6(5):443-8.
- [80] Lawall J, Kessler E. Michelson interferometry with 10 pm accuracy. *Review of Scientific Instruments* 2000;71(7):2669-76.
- [81] Guo J, Zhang Y, Shen S. Compensation of nonlinearity in a new optical heterodyne interferometer with doubled measurement resolution. *Optics communications* 2000;184(1):49-55.
- [82] Wang C, Augousti A, Mason J. Real time evaluation and correction of nonlinear errors in single frequency interferometers. *Transactions of the Institute of Measurement and Control* 2000;22(5):405-12.
- [83] Schmitz T, Beckwith J. Acousto-optic displacement-measuring interferometer: a new heterodyne interferometer with Ångstrom-level periodic error. *Journal of modern optics* 2002;49(13):2105-14.
- [84] Wu C-M, Lin S-T, Fu J. Heterodyne interferometer with two spatial-separated polarization beams for nanometrology. *Optical and quantum electronics* 2002;34(12):1267-76.

- [85] Eom T, Choi T, Lee K, Choi H, Lee S. A simple method for the compensation of the nonlinearity in the heterodyne interferometer. *Measurement Science and Technology* 2002;13(2):222-5.
- [86] Yeh H-C, Ni W-T, Pan S-S. Real-time motion control with subnanometer heterodyne interferometry. *International Journal of Modern Physics D* 2002;11(07):1087-99.
- [87] Halverson PG, Spero RE. Signal processing and testing of displacement metrology gauges with picometre-scale cyclic nonlinearity. *Journal of Optics A: Pure and Applied Optics* 2002;4(6):S304.
- [88] Bitou Y. Polarization mixing error reduction in a two-beam interferometer. *Optical Review* 2002;9(5):227-9.
- [89] Lay OP, Dubovitsky S. Polarization compensation: a passive approach to a reducing heterodyne interferometer nonlinearity. *Optics letters* 2002;27(10):797-9.
- [90] Wu C-m. Periodic nonlinearity resulting from ghost reflections in heterodyne interferometry. *Optics communications* 2003;215(1):17-23.
- [91] Li Z, Herrmann K, Pohlenz F. A neural network approach to correcting nonlinearity in optical interferometers. *Measurement Science and Technology* 2003;14(3):376.
- [92] Dai G, Pohlenz F, Danzebrink H-U, Hasche K, Wilkening G. Improving the performance of interferometers in metrological scanning probe microscopes. *Measurement Science and Technology* 2004;15(2):444.
- [93] Keem T, Gonda S, Misumi I, Huang Q, Kurosawa T. Removing nonlinearity of a homodyne interferometer by adjusting the gains of its quadrature detector systems. *Applied optics* 2004;43(12):2443-8.
- [94] Keem T, Gonda S, Misumi I, Huang Q, Kurosawa T. Simple, real-time method for removing the cyclic error of a homodyne interferometer with a quadrature detector system. *Applied optics* 2005;44(17):3492-8.
- [95] Schmitz T, Chu D, Houck III L. First-order periodic error correction: validation for constant and non-constant velocities with variable error magnitudes. *Measurement Science and Technology* 2006;17(12):3195.
- [96] Hong M, Jeon J, Park K, You K. Adaptive nonlinearity compensation of heterodyne laser interferometer. In: *Knowledge-Based Intelligent Information and Engineering Systems*. 2006. p. 545-52.
- [97] Buchta Z, Lazar J. Small displacement measurements with subatomic resolution by beat frequency measurements. *Measurement Science and Technology* 2007;18(7):2005.

- [98] Olyae S, Nejad MS. Nonlinearity and frequency-path modelling of three-longitudinal-mode nanometric displacement measurement system. *Optoelectronics, IET* 2007;1(5):211-20.
- [99] Teng H-K, Lang K-C. Heterodyne interferometer for displacement measurement with amplitude quadrature and noise suppression. *Optics communications* 2007;280(1):16-22.
- [100] Schluchter C, Ganguly V, Chu D, Schmitz TL. Low velocity compensation for first order periodic error caused by beam shear. *Precision engineering* 2011;35(2):241-7.
- [101] Ellis JD, Baas M, Joo K-N, Spronck JW. Theoretical analysis of errors in correction algorithms for periodic nonlinearity in displacement measuring interferometers. *Precision engineering* 2012;36(2):261-9.
- [102] Wu C, Su C, Peng G, Huang Y. Polarimetric, nonlinearity-free, homodyne interferometer for vibration measurement. *Metrologia* 1996;33(6):533.
- [103] Köning R, Dixon R, Fu J, Vorbürger T. The role of periodic interferometer errors in the calibration of capacitance displacement sensors for nanometrology applications. *Measurement Science and Technology* 2001;12(11):2002.
- [104] Wu C-m. Heterodyne interferometric system with subnanometer accuracy for measurement of straightness. *Applied optics* 2004;43(19):3812-6.
- [105] Evans C, Holmes M, Demarest F, Newton D, Stein A. Metrology and calibration of a long travel stage. *CIRP Annals-Manufacturing Technology* 2005;54(1):495-8.
- [106] Deng Y-l, Li X-j, Wu Y-b, Hu J-g, Yao J-q. Analysis of frequency mixing error on heterodyne interferometric ellipsometry. *Measurement Science and Technology* 2007;18(11):3339.
- [107] Liu H, Cartwright AN, Basaran C. Moire interferogram phase extraction: a ridge detection algorithm for continuous wavelet transforms. *Applied optics* 2004;43(4):850-7.
- [108] Cherbuliez M, Jacquot P. Phase computation through wavelet analysis: yesterday and nowadays. *Fringe*. 2001. p. 154-62.
- [109] A. C1553-08 Standard guide for drying behavior of spent nuclear fuel ASTM International. 2008.
- [110] NUREG-1536. Nuclear Regulatory Commission 2010.
- [111] Miller LW, G; Mintz, T; Wilt, T. Prepared for US Nuclear Regulatory Commission contract No NRC-02-07-C-006 Vacuum drying test plan - public version center for Nuclear Waste Regulatory Analyses. 2013.

- [112] EPRI Temperature limit determination for the inert dry storage of spent nuclear fuel. 1994.
- [113] Muravin B, Muravin G, Lezvinsky L. The Fundamentals of Structural Health Monitoring by the Acoustic Emission Method. In: Proceedings of the 20th International Acoustic Emission Symposium. 2010. p. 253-8.
- [114] Strutt JW. On waves propagated along the plane surface of an elastic solid. Proceedings of the London Mathematical Society 1885;17(1):4-11.
- [115] Rose JL. Ultrasonic waves in solid media: Cambridge university press; 2004.
- [116] Igor'A V. Rayleigh and Lamb waves: physical theory and applications: Plenum Press; 1967.
- [117] Julius M. The Theory of Elastic Waves and Waveguides. North-Holland Publishing Company, Amsterdam, New York. 1978.
- [118] Achenbach J. Wave propagation in elastic solids. 1984.
- [119] Auld BA. Acoustic fields and waves in solids: RE Krieger; 1990.
- [120] Graff KF. Wave motion in elastic solids: Courier Corporation; 1975.
- [121] Nayfeh AH. Wave propagation in layered anisotropic media: With application to composites: Elsevier; 1995.
- [122] Rose JL. Standing on the shoulders of giants: an example of guided wave inspection. Materials Evaluation 2002;60(1):53-9.
- [123] Rose JL. A baseline and vision of ultrasonic guided wave inspection potential. Journal of pressure vessel technology 2002;124(3):273-82.
- [124] Cook E, Valkenburg H. Surface waves at ultrasonic frequencies. ASTM bulletin 1954;3:81-4.
- [125] Liu G, Qu J. Guided circumferential waves in a circular annulus. Journal of Applied Mechanics 1998;65(2):424-30.
- [126] Zhao X, Rose JL. Guided circumferential shear horizontal waves in an isotropic hollow cylinder. The Journal of the Acoustical Society of America 2004;115(5):1912-6.
- [127] Gridin D, Craster R, Fong J, Lowe M, Beard M. The high-frequency asymptotic analysis of guided waves in a circular elastic annulus. Wave Motion 2003;38(1):67-90.
- [128] Kley M, Valle C, Jacobs LJ, Qu J, Jarzynski J. Development of dispersion curves for two-layered cylinders using laser ultrasonics. The Journal of the Acoustical Society of America 1999;106(2):582-8.

- [129] Valle C, Qu J, Jacobs LJ. Guided circumferential waves in layered cylinders. *International Journal of Engineering Science* 1999;37(11):1369-87.
- [130] Qu J, Berthelot Y, Jacobs L. Crack detection in thick annular components using ultrasonic guided waves. *Proceedings of the Institution of Mechanical Engineers, Part C: Journal of Mechanical Engineering Science* 2000;214(9):1163-71.
- [131] Luo W, Rose JL, Kwun H. Circumferential shear horizontal wave axial-crack sizing in pipes. *Research in Nondestructive Evaluation* 2005;15(4):149-71.
- [132] Ghosh J. Longitudinal vibrations of a hollow cylinder. *Bulletin of the Calcutta Mathematical Society* 1923;14:31-40.
- [133] Gazis DC. Three - dimensional investigation of the propagation of waves in hollow circular cylinders. I. Analytical foundation. *The Journal of the Acoustical Society of America* 1959;31(5):568-73.
- [134] Zemanek Jr J. An experimental and theoretical investigation of elastic wave propagation in a cylinder. *The Journal of the Acoustical Society of America* 1972;51(1B):265-83.
- [135] Silk M, Bainton K. The propagation in metal tubing of ultrasonic wave modes equivalent to Lamb waves. *Ultrasonics* 1979;17(1):11-9.
- [136] Alleyne D, Cawley P. The excitation of Lamb waves in pipes using dry-coupled piezoelectric transducers. *Journal of Nondestructive Evaluation* 1996;15(1):11-20.
- [137] Quarry MJ, Rose JL. Multimode guided wave inspection of piping using comb transducers. *Materials Evaluation* 1999;57(10):1089-90.
- [138] Kwun H, Teller CM. Magnetostrictive generation and detection of longitudinal, torsional, and flexural waves in a steel rod. *The Journal of the Acoustical Society of America* 1994;96(2):1202-4.
- [139] Ditri JJ, Rose JL. Excitation of guided elastic wave modes in hollow cylinders by applied surface tractions. *Journal of Applied Physics* 1992;72(7):2589-97.
- [140] Li J, Rose JL. Excitation and propagation of non-axisymmetric guided waves in a hollow cylinder. *The Journal of the Acoustical Society of America* 2001;109(2):457-64.
- [141] Sun Z, Zhang L, Gavigan B, Hayashi T, Rose JL. Ultrasonic flexural torsional guided wave pipe inspection potential. In: *ASME 2003 Pressure Vessels and Piping Conference*. 2003. p. 29-34.
- [142] Raghavan A, Cesnik CE. Finite-dimensional piezoelectric transducer modeling for guided wave based structural health monitoring. *Smart materials and structures* 2005;14(6):1448.

- [143] Shen Y, Giurgiutiu V. Predictive modeling of nonlinear wave propagation for structural health monitoring with piezoelectric wafer active sensors. *Journal of Intelligent Material Systems and Structures* 2014;25(4):506-20.
- [144] Fellingner F, Langenberg K. Numerical techniques for elastic wave propagation and scattering. In: *Elastic Waves and Ultrasonic Nondestructive Evaluation*. 1990. p. 81-6.
- [145] Leckey CA, Rogge MD, Miller CA, Hinders MK. Multiple-mode Lamb wave scattering simulations using 3D elastodynamic finite integration technique. *Ultrasonics* 2012;52(2):193-207.
- [146] Leckey C, Rogge M, Parker F. Microcracking in composite laminates: Simulation of crack-induced ultrasound attenuation. 2012.
- [147] Peng H, Ye L, Meng G, Mustapha S, Li F. Concise analysis of wave propagation using the spectral element method and identification of delamination in CF/EP composite beams. *Smart materials and structures* 2010;19(8):085018.
- [148] Kim Y, Ha S, Chang F-K. Time-domain spectral element method for built-in piezoelectric-actuator-induced lamb wave propagation analysis. *AIAA journal* 2008;46(3):591-600.
- [149] Mansur W, Brebbia C. Numerical implementation of the boundary element method for two dimensional transient scalar wave propagation problems. *Applied Mathematical Modelling* 1982;6(4):299-306.
- [150] Zhu W, Rose JL. Lamb wave generation and reception with time-delay periodic linear arrays: A BEM simulation and experimental study. *Ultrasonics, Ferroelectrics, and Frequency Control, IEEE Transactions on* 1999;46(3):654-64.
- [151] Aimi A, Gazzola S, Guardasoni C. Energetic boundary element method analysis of wave propagation in 2D multilayered media. *Mathematical Methods in the Applied Sciences* 2012;35(10):1140-60.
- [152] Liu QH, Schoen E, Daube F, Randall C, Liu HI, Lee P. Large - scale 3D finite - difference simulation of elastic wave propagation in borehole environments. *The Journal of the Acoustical Society of America* 1994;96(5):3337-.
- [153] Leutenegger T, Dual J. Detection of defects in cylindrical structures using a time reverse method and a finite-difference approach. *Ultrasonics* 2002;40(1):721-5.
- [154] Kelly K. Numerical study of Love wave propagation. *Geophysics* 1983;48(7):833-53.
- [155] Virieux J. SH-wave propagation in heterogeneous media: velocity-stress finite-difference method. *Geophysics* 1984;49(11):1933-42.

- [156] Reddy JN. An introduction to the finite element method: McGraw-Hill New York; 1993.
- [157] Cook RD. Concepts and applications of finite element analysis: John Wiley & Sons; 2007.
- [158] Bathe K-J. Finite element procedures: Klaus-Jurgen Bathe; 2006.
- [159] Soni S, Das S, Chattopadhyay A. Simulation of damage-features in a lug joint using guided waves. *Journal of Intelligent Material Systems and Structures* 2009;20(12):1451-64.
- [160] Pistone E, Li K, Rizzo P. Noncontact monitoring of immersed plates by means of laser-induced ultrasounds. *Structural Health Monitoring* 2013;12(5-6):549-65.
- [161] Song F, Huang G, Hudson K. Guided wave propagation in honeycomb sandwich structures using a piezoelectric actuator/sensor system. *Smart materials and structures* 2009;18(12):125007.
- [162] Cho H, Ogawa S, Takemoto M. Non-contact laser ultrasonics for detecting subsurface lateral defects. *NDT & E International* 1996;29(5):301-6.
- [163] Abbate A, Frankel J, Das P. Wavelet transform signal processing for dispersion analysis of ultrasonic signals. In: *Ultrasonics Symposium, 1995 Proceedings, 1995 IEEE*. 1995. p. 751-5.
- [164] Kaya K, Bilgutay NM, Murthy R. Flaw detection in stainless steel samples using wavelet decomposition. In: *Ultrasonics Symposium, 1994 Proceedings, 1994 IEEE*. 1994. p. 1271-4.
- [165] Murase M, Kawashima K. Noncontact Evaluation of Defects in Thin Plate With Multimodes Lamb's Waves and Wavelet Transform. In: *ASME 2002 International Mechanical Engineering Congress and Exposition*. 2002. p. 27-30.
- [166] Ahmad R, Kundu T. Guided wave technique to detect defects in pipes using wavelet transform. In: *Proceedings of the Second European Workshop on Structural Health Monitoring*. 2004. p. 7-9.
- [167] Ahmad R, Banerjee S, Kundu T. Pipe wall damage detection in buried pipes using guided waves. *Journal of pressure vessel technology* 2009;131(1):011501.
- [168] Jeong H, Jang Y-S. Wavelet analysis of plate wave propagation in composite laminates. *Composite Structures* 2000;49(4):443-50.
- [169] Ikeda T. *Fundamentals of piezoelectricity*: Oxford university press; 1996.

[170] Santoni GB, Yu L, Xu B, Giurgiutiu V. Lamb wave-mode tuning of piezoelectric wafer active sensors for structural health monitoring. *Journal of Vibration and Acoustics* 2007;129(6):752-62.

[171] Giurgiutiu V. Tuned Lamb wave excitation and detection with piezoelectric wafer active sensors for structural health monitoring. *Journal of Intelligent Material Systems and Structures* 2005;16(4):291-305.